A UNITED STATES DEPARTMENT OF COMMERCE PUBLICATION

SECTION A

# JOURNAL OF RESEARCH

## of the NATIONAL BUREAU OF STANDARDS

JNBAAR 77A, (3) 309-382 May-June 1973

# Physics and Chemistry

U.S. DEPARTMENT OF COMMERCE
National Bureau of Standards

**Journal of Research**

**of the**

**National Bureau of Standards**

A. Physics and Chemistry

May–June • 1973

VOLUME • 77A

NUMBER • 3

Editor: C. W. Beckett

Associate Editor: D. D. Wagman

Publication dates:
Feb. 1, Apr. 1, June 1, Aug. 1, Oct. 1, Dec. 1, 1973

J. Res. Nat. Bur. Stand. (U.S.), A

**JOURNAL OF RESEARCH**

The National Bureau of Standards Journal of Research reports research and development in the fields of activity shown at right. Also included from time to time are survey articles on topics closely related to the Bureau's scientific and technical program.

The Journal is published in two separate sections as follows:

**A. Physics and Chemistry**

Contains papers of interest primarily to scientists working in these fields. Issued six times a year. Annual subscription: domestic, $17.00; foreign $21.25. Single copy, varies.

**B. Mathematical Sciences**

Presents studies and compilations designed mainly for the mathematician and the theoretical physicist. Issued quarterly. Annual subscription: domestic, $9.00; foreign, $11.25. Single copy, $2.25.

The National Bureau of Standards[1] was established by an act of Congress March 3, 1901. The Bureau's overall goal is to strengthen and advance the Nation's science and technology and facilitate their effective application for public benefit. To this end, the Bureau conducts research and provides: (1) a basis for the Nation's physical measurement system, (2) scientific and technological services for industry and government, (3) a technical basis for equity in trade, and (4) technical services to promote public safety. The Bureau consists of the Institute for Basic Standards, the Institute for Materials Research, the Institute for Applied Technology, the Institute for Computer Sciences and Technology, and the Office for Information Programs.

**THE INSTITUTE FOR BASIC STANDARDS** provides the central basis within the United States of a complete and consistent system of physical measurement; coordinates that system with measurement systems of other nations; and furnishes essential services leading to accurate and uniform physical measurements throughout the Nation's scientific community, industry, and commerce. The Institute consists of a Center for Radiation Research, an Office of Measurement Services and the following divisions:

Applied Mathematics — Electricity — Mechanics — Heat — Optical Physics — Nuclear Sciences[2] — Applied Radiation[2] — Quantum Electronics[2] — Electromagnetics[2] — Time and Frequency[2] — Laboratory Astrophysics[2] — Cryogenics[2].

**THE INSTITUTE FOR MATERIALS RESEARCH** conducts materials research leading to improved methods of measurement, standards, and data on the properties of well-characterized materials needed by industry, commerce, educational institutions, and Government; provides advisory and research services to other Government agencies; and develops, produces, and distributes standard reference materials. The Institute consists of the Office of Standard Reference Materials and the following divisions:

Analytical Chemistry — Polymers — Metallurgy — Inorganic Materials — Reactor Radiation — Physical Chemistry.

**THE INSTITUTE FOR APPLIED TECHNOLOGY** provides technical services to promote the use of available technology and to facilitate technological innovation in industry and Government; cooperates with public and private organizations leading to the development of technological standards (including mandatory safety standards), codes and methods of test; and provides technical advice and services to Government agencies upon request. The Institute consists of a Center for Building Technology and the following divisions and offices:

Engineering and Product Standards — Weights and Measures — Invention and Innovation — Product Evaluation Technology — Electronic Technology — Technical Analysis — Measurement Engineering — Structures, Materials, and Life Safety[4] — Building Environment[4] — Technical Evaluation and Application[4] — Fire Technology.

**THE INSTITUTE FOR COMPUTER SCIENCES AND TECHNOLOGY** conducts research and provides technical services designed to aid Government agencies in improving cost effectiveness in the conduct of their programs through the selection, acquisition, and effective utilization of automatic data processing equipment; and serves as the principal focus within the executive branch for the development of Federal standards for automatic data processing equipment, techniques, and computer languages. The Center consists of the following offices and divisions:

Information Processing Standards — Computer Information — Computer Services — Systems Development — Information Processing Technology.

**THE OFFICE FOR INFORMATION PROGRAMS** promotes optimum dissemination and accessibility of scientific information generated within NBS and other agencies of the Federal Government; promotes the development of the National Standard Reference Data System and a system of information analysis centers dealing with the broader aspects of the National Measurement System; provides appropriate services to ensure that the NBS staff has optimum accessibility to the scientific information of the world. The Office consists of the following organizational units:

Office of Standard Reference Data — Office of Technical Information and Publications — Library — Office of International Relations.

[1] Headquarters and Laboratories at Gaithersburg, Maryland, unless otherwise noted; mailing address Washington, D.C. 20234.
[2] Part of the Center for Radiation Research.
[3] Located at Boulder, Colorado 80302.
[4] Part of the Center for Building Technology.

U.S. DEPARTMENT OF COMMERCE
Frederick B. Dent, Secretary
NATIONAL BUREAU OF STANDARDS
Richard W. Roberts, Director

Order all publications from the Superintendent of Documents
U.S. Government Printing Office, Washington, D.C. 20402

The Secretary of Commerce has determined that the publication of this periodical is necessary in the transaction of the public business required by law of this Department. Use of funds for printing this periodical has been approved by the Director of the Office of Management and Budget through June 30, 1976.

JOURNAL OF RESEARCH of the National Bureau of Standards—A. Physics and Chemistry
Vol. 77A, No. 3, May–June 1973

# The International Practical Temperature Scale of 1968 in the Region 13.81 K to 90.188 K as Maintained at the National Bureau of Standards

**George T. Furukawa, John L. Riddle, and William R. Bigge**

**Institute for Basic Standards, National Bureau of Standards, Washington, D.C. 20234**

**(January 18, 1973)**

The reproducibility of the International Practical Temperature Scale of 1968 (IPTS–68) in the region of 13.81 K to 90.188 K using standard platinum resistance thermometers is discussed. The effect of errors above 0 °C on the calibration between 13 and 90 K is analyzed. Calibrations resulting from least squares and "fixed point" treatment of the data are compared. The results show that in general the NBS–IPTS–68 temperature scale maintained at the National Bureau of Standards (NBS) by reference standard platinum resistance thermometers is transferred to thermometers calibrated at the NBS within a few tenths of a mK between about 20 and 90.188 K and within about ±1 mK between 13.81 and 20 K. Agreements within a few mK are shown between the observed values of temperatures, employing platinum resistance thermometers calibrated in terms of the NBS–IPTS–68 scale, and the values of temperatures of the fixed points in the region 13.81 to 90.188 K given in the text of the IPTS–68.

Key words: International Practical Temperature Scale; NBS–IPTS–68; NBS–1955 provisional scale; platinum resistance thermometer.

## 1. Introduction

Between 13.81 K (−259.34 °C) and 903.89 K (630.74 °C) the International Practical Temperature Scale of 1968 [1],[1] referred to hereafter as IPTS–68, is defined by nine fixed points and specified interpolation formula to relate the temperature and the resistance ratio,

$$W(T) = R(T)/R(0\,°C),$$

of the particular standard platinum resistance thermometer (prt). The defining fixed points are based on equilibrium states between phases of pure substances. These equilibrium states and their assigned values of temperature on the IPTS–68 are given in table 1. The thermometer resistor must be annealed pure platinum, supported in a "strain-free" manner and have a value of $W$ at 100 °C not less than 1.39250.

Below 0 °C the $W$ versus temperature relation in between the fixed points is given by

$$W(T) = W^*(T) + \Delta W(T), \qquad (1)$$

[1] Figures in brackets indicate the literature reference at the end of this paper.

TABLE 1. *Defining fixed points of the IPTS–68 in the platinum resistance thermometer range*

| Equilibrium State [a,b,c,d] | Assigned value of the IPTS–68 temperature | |
|---|---|---|
| | $T$, K | $t$, °C |
| e-$H_2$, TP | 13.81 | −259.34 |
| e-$H_2$, BP (33,330.6 N/m²) | 17.042 | −256.108 |
| e-$H_2$, NBP | 20.28 | −252.87 |
| Ne, NBP | 27.102 | −246.048 |
| $O_2$, TP | 54.361 | −218.789 |
| $O_2$, NBP | 90.188 | −182.962 |
| $H_2O$, TP | 273.16 | 0.01 |
| $H_2O$, NBP or Sn, FP | 373.15<br>505.1181 | 100<br>231.9681 |
| Zn, FP | 692.58 | 419.58 |

[a] Except for the triple points and one e-$H_2$ point at 17.042 K the assigned values of temperature are for equilibrium states at a pressure of one standard atmosphere (101,325 N/m²). In the realization of the fixed points small departures from the assigned temperatures occur as a result of small deviations from the specified pressure at the point of immersion of the thermometer. Adjustment is made for these small temperature differences.

[b] TP = triple point, BP = boiling point, NBP = normal boiling point, FP = freezing point, and e-$H_2$ = equilibrium hydrogen.

[c] The water used should have the isotopic composition of ocean water.

[d] The neon used should have the normal isotopic composition: 0.909 mol $^{20}$Ne, 0.0808 mol $^{22}$Ne, and 0.0026 mol $^{21}$Ne.

where $W^*(T)$ is a reference function defined by

$$T = \sum_{i=0}^{20} A_i [\ln W^*(T)]^i \qquad (2)$$

and $\Delta W(T)$ is a deviation function which is a polynomial in $T$ [2]. (The coefficients $A_i$ of eq (1) are given in reference [1].) The range 13.81 to 273.15 K is divided into four subranges, each with its specified deviation function. The coefficients of the polynomials are determined from $\Delta W(T)$ obtained by calibration at the fixed points (see sec. 4 for further discussion) [1]. From 0 to 630.74 °C the values of temperature $t$ are defined by

$$t = t' + 0.045\left(\frac{t'}{100}\right)\left(\frac{t'}{100}-1\right)\left(\frac{t'}{419.58}-1\right)\left(\frac{t'}{630.74}-1\right), \qquad (3)$$

where

$$t' = \frac{1}{\alpha}[W(t')-1] + \delta\left(\frac{t'}{100}\right)\left(\frac{t'}{100}-1\right). \qquad (4)$$

(For simplification, the unit °C has been omitted from eqs (3) and (4).) The thermometer constants $R(0\ °C)$, $\alpha$, and $\delta$ are determined from resistance measurements at the triple point (TP) of water, the normal boiling point (NBP) of water (or the freezing point of tin), and the freezing point of zinc. By definition $t$ and $T$ are related by $t = T - 273.15$ K.

At the National Bureau of Standards (NBS) the defining fixed points above 0 °C are maintained and are employed regularly in the calibration of prt's. The defining fixed points below 0 °C are "maintained" at present by reference standard prt's of the capsule type. This paper describes the NBS–IPTS–68 temperature scale between 13.81 and 90.188 K maintained by the reference standard prt's, shows the degree of agreement of the scale with the IPTS–68 in terms of recently published measurements employing prt's calibrated on the scale, and demonstrates the reproducibility of the NBS–IPTS–68 scale by prt's that have been received for calibration at the NBS. The cryostat in which the calibrations are performed is described. The reduction of the calibration data by a least squares method is compared with a "fixed point" method.

## 2. NBS–IPTS–68 Scale

The following is a brief history and description of the IPTS–68 temperature scale between 13.81 and 90.188 K now being maintained on reference standard prt's at the NBS. In 1939 the NBS–1939 scale [3] was established by comparing capsule type prt's with values of temperatures that were determined by a helium gas thermometer between 10.8 and 91.4 K. Considering the apparatus that was employed at the time, the authors of the NBS–1939 scale stated, "It is hoped that the scale will be found to be in agreement with the thermodynamic scale to within ±0.02°" [3]. In 1955 the values of temperature of the NBS–1939 scale were reduced by 0.01 K because of the adoption by the Tenth General Conference on Weights and Measures in 1954 of a thermodynamic Kelvin scale that was defined by assigning the value 273.16 K to the TP of water and also on the basis of accumulated data indicating that the value of the NBP of normal hydrogen was 0.01 K too high on the NBS–1939 scale [4]. This modified scale was named the NBS–1955 scale [4]. By 1962 three other laboratories had developed provisional temperature scales between about 10 and 90 K based on gas thermometry [5,6,7,8,9,10]. To determine the relation among the existing four provisional temperature scales they were intercompared in 1964 at the Physicotechnical and Radiotechnical Measurements Institute (Moscow, U.S.S.R.) and at the National Physical Laboratory (Teddington, Middlesex, U.K.) [11]. After the four provisional scales were adjusted to a common NBP of oxygen and a common NBP of normal hydrogen, the scales were found to agree within ±0.01 between 20 K and 90 K. Between 13.81 and 90.188 K the IPTS–68 scale is based both on the results of these intercomparisons and on "best" values of temperature assigned to the defining fixed points. The new scale was intended to replace the four provisional scales, but at the time of its adoption no national laboratory could realize all five new fixed points below the NBP of oxygen. The Comité Consultatif de Thermometrie that recommended the IPTS–68 to the Comité International des Poids et Mesures to be adopted, therefore, formally recognized the use of the former provisional scales, which are highly reproducible, and published differences [12] between these scales and the IPTS–68 that would give a close approximation to the IPTS–68. The IPTS–68 scale between 13.81 and 90.188 K which is presently maintained at NBS was obtained by first adjusting the values of $T$(NBS–55) of the reference prt by the published differences between the IPTS–68 and the NBS–1955 scale. To obtain a smooth scale, the deviation ($\Delta W$) between each of these adjusted values and the corresponding value of the reference function ($W^*$) was smoothed by a least squares method using the nearest five points. These smoothed values of $\Delta W$ were added to the reference function values and the resulting table was subtabulated at 0.1 K intervals by cubic interpolation. The temperature scale represented by these tabular values will be referred to in this paper as NBS–IPTS–68 (tabular).

Because the NBS–IPTS–68 (tabular) scale is not convenient for computer use, the "best" IPTS–68 coefficients of the deviation functions were derived from the values of the tabular scale. This derived scale which is given in terms of the coefficients of the deviation functions will be referred to in this paper as the NBS–IPTS–68 scale. The NBS–IPTS–68 and

NBS–IPTS–68 (tabular) temperature scales are compared in figure 1. The differences between the two "scales" become somewhat larger in terms of the temperature below about 20 K, but in terms of resistance the deviations are about the same over the whole temperature range. The lengths of the vertical lines represent 20 $\mu\Omega$. Below 21 K the deviations,

$$T[\text{NBS}-\text{IPTS}-68\,(\text{tabular})]-T[\text{NBS}-\text{IPTS}-68],$$

are connected to show more clearly the general trend in the differences between the two scales. Because of the numerical smoothing procedure employed in obtaining the NBS–IPTS–68 (tabular) scale, the deviation plot exhibits some "noise."

The relation between the NBS–IPTS–68 and the IPTS–68 can be assessed from measurements, e.g., at the fixed points, employing thermometers that have been calibrated in terms of the NBS scale. Table 2 lists some of the measurements that have been reported for the defining fixed points. Whenever the temperature values were reported on the NBS–1955 (or NBS–1939) scale, appropriate adjustments were made to NBS–IPTS–68 employing the published differences between IPTS–68 and NBS–1955 [12]. When the temperature value was in NBS–1939, it was first adjusted to NBS–1955 and then converted to the NBS–IPTS–68 scale. Where data were available on the other provisional scales, they were converted to the IPTS–68 employing the published differences [12]. The values of temperatures of the defining fixed points obtained on the NBS–IPTS–68 scale are in good agreement with the assigned values except for the NBP of oxygen. Inasmuch as the values on all four provisional scales are in good agreement, the oxygen NBP realized by Muijlwijk, Moussa, and van

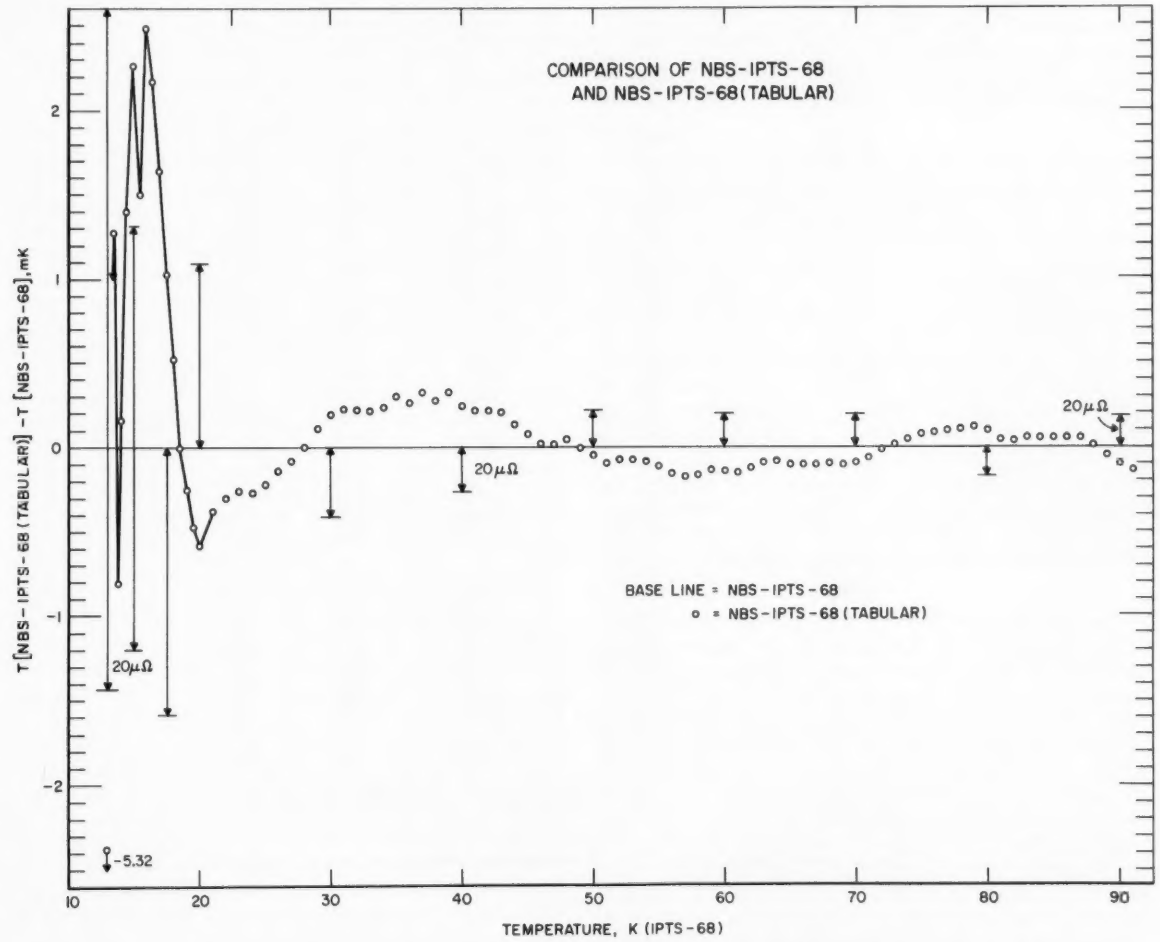


FIGURE 1. *Comparison of the NBS–IPTS–68 (tabular) temperature scale with the NBS–IPTS–68 temperature scale.*

NBS–IPTS–68 (tabular) is a tabular scale based on combining the NBS–1955 scale and the published differences [12] between the NBS–1955 scale and the IPTS–68 scale and numerically smoothing the adjusted scale. The NBS–IPTS–68 is based on the relation given by eq (1) and the "best" deviation functions $\Delta W(T)$ derived from NBS–IPTS–68 (tabular).

TABLE 2. *Comparison of observed values of temperature of some defining fixed points and secondary reference points on the various provisional temperature scales adjusted to the IPTS–68*

| Equilibrium point and assigned temperature on the IPTS–68 | Temperature scale [a] | Temperature value | Year of work | Reference |
|---|---|---|---|---|
| e-$H_2$, TP 13.81 K | NBS [b] | 13.799 | 1951 | [13] |
| | NPL | 13.813 | 1963 | [14] |
| | NBS | $13.805_1$ | 1971 | [15] |
| | NBS | $13.807_9$ | 1971 | [16] |
| e-$H_2$, BP (25/76 atm) 17.042 K | NBS | $17.042_{61}$ | 1971 | [15] |
| e-$H_2$, NBP 20.28 K | NBS [b] | 20.276 | 1951 | [13] |
| | NBS | 20.276 | 1962 | [17] |
| | NPL | 20.2796 | 1963 | [14] |
| | NBS | $20.278_{19}$ | 1971 | [15] |
| | NBS | 20.2798 | 1971 | [16] |
| Ne, NBP 27.102 K | NBS | 27.099 | 1962 | [18] |
| | NBS | 27.103 | 1970 | [19] |
| | NBS | $27.103_2$ | 1970 | [20] |
| | NBS | 27.103 | 1972 | [32] |
| $O_2$, TP 54.361 K | NBS | 54.3576 | 1966 | [21] |
| $O_2$, NBP 90.188 K | NBS | 90.1956 | 1966 | [21] |
| | NBS | 90.1912 | 1966 | [21] |
| | NBS | 90.1924 | 1966 | [21] |
| | PSU | 90.1928 | 1966 | [21] |
| | PSU | 90.1919 | 1966 | [21] |
| | NPL | 90.1900 | 1966 | [21] |
| | NPL | 90.1935 | 1966 | [21] |
| | PRMI | 90.1935 | 1966 | [21] |
| | PRMI | 90.1937 | 1966 | [21] |
| | PRMI | 90.1948 | 1966 | [21] |
| Ne, TP 24.555 K | NBS | 24.552 | 1962 | [18] |
| | NBS | 24.561 | 1970 | [19] |
| | NBS | 24.560 | 1970 | [20] |
| | IPTS–68 [c] | 24.5620 | 1971 | [22] |
| | IPTS–68 [c] | 24.5618 | 1971 | [22] |
| $N_2$, TP 63.148 K | NBS | 63.1481 | 1966 | [23] |
| | NBS | 63.1469 | 1966 | [23] |
| | PRMI | 63.1479 | 1966 | [23] |
| | PRMI | 63.1477 | 1966 | [23] |
| $N_2$,NBP 77.348 K | NBS [b] | 77.3459 | 1954 | [24] |
| | NBS | 77.3466 | 1963 | [25] |
| | NBS (1) [d] | 77.3493 | 1966 | [26] |
| | NBS (1) [d] | 77.3471 | 1966 | [26] |
| | NBS (2) [d] | 77.3481 | 1966 | [26] |
| | PRMI | 77.3475 | 1966 | [26] |
| | PRMI | 77.3477 | 1966 | [26] |
| | NPL (3) [d] | 77.3469 | 1966 | [26] |
| | NPL (3) [d] | 77.3473 | 1966 | [26] |
| | NPL (4) [d] | 77.3486 | 1966 | [26] |

[a] NBS = NBS–IPTS–68, NPL = NPL–IPTS–68, PRMI = PRMI–IPTS–68, and PSU = PSU–IPTS–68.

[b] Initially published on the NBS–1939 scale.

[c] The prt was calibrated at the IPTS–68 defining fixed-points.

[d] The number identifies the prt.

Dijk [21] may have been slightly too high. Muijlwijk, Durieux, and van Dijk [26] realized a NBP of e-$H_2$ that is 3.7 mK higher than the value on the NBS–IPTS–68. Of the secondary reference points, the NBS–IPTS–68 values are in good agreement with the values recommended in the text of the IPTS–68 and with the values of the other provisional scales, except for the *TP* of neon. Since the NBS–IPTS–68 values for the *TP* of neon are in close agreement with the value of Tiggelman, van Rijn, and Durieux [22] that was obtained employing a prt calibrated directly with the IPTS–68 fixed points, the value recommended in the text of the IPTS–68 may be too low.

## 3. Design and Operation of the Cryostat

The capsule type prt's are calibrated in terms of the standards in the cryostat shown schematically in figure 2. The copper comparison block V, shown enlarged in figure 3, has wells for six thermometers, two standards and four thermometers under test. Stopcock grease is used to enhance the thermal contact between the prt and the copper block. The wiring arrangement shown in figure 4 is employed to minimize the number of leads and, therefore, the heat transfer through the leads between the surroundings and the copper block. Five prt's are wired with only twelve leads. The first standard is wired separately with four additional leads to allow it to be electrically isolated from the group of five prt's. In the calibration process the resistance of the first standard and the resistance of any one of the four thermometers under test or the second standard are determined simultaneously by measurements made with two Mueller bridges by two operators.

The cryostat (fig. 2) was designed so that the central core could remain stationary when the cryostat assembly is lowered to expose the thermometer comparison block for installation or removal of thermometers. To the thin-wall, stainless steel central support tube G are attached, from bottom upward, the copper comparison block V, the thermometer lead terminal block T, thermal tie downs Q and N (two), and the upper support section which contains the vacuum line and the exit seal for the leads to the thermometers, thermocouples, and heaters. After the cryostat assembly is raised into position around the core the vacuum seal consisting of a Viton "O" ring E is closed; thus, only a single vacuum seal at room temperature is involved in the installation or removal of thermometers from the cryostat.

For the thermometer leads, manganin wire (No. 26 AWG, 0.404 mm diam.) insulated with a heavy coating of Formvar [2] was selected for its small temperature coefficient of resistance to minimize the possible change in the difference of resistance of the potential leads between the normal (N) and reverse (R) readings of the Mueller bridge. The leads are "tempered" by being placed in good thermal contact with a series of three thermal tie downs (two of N and one of Q, shown schematically in fig. 2 and shown in detail in fig. 5). The leads are cemented in vertical grooves C of the copper cylinder D that is soldered to the central support tube A (G in fig. 2). Copper cylinder E is fitted snugly over D and held securely by pin H. The copper cylinder E contains the spring fingers G of beryllium copper. In the two thermal tie downs N the fingers make thermal contact with the refrigerant bath and in thermal tie down Q the fingers make thermal contact with the shield S. Q contains also a heater and a five-junction Chromel P/constantan thermopile for temperature control; the thermocouples are placed in thermal contact with Q by means of the "thermal tie down" shown by the insert F. The thermometer leads are tempered on the copper comparison block by cementing them in grooves shown as K in figure 3. The manganin thermometer leads and the copper leads to the thermocouples and heaters exit at the top of the cryostat through small holes in a ceramic disk. A hard wax is used to make the vacuum seal around the ceramic disk and the lead wires.

During operation the cryostat (fig. 2) is surrounded by a liquid helium Dewar M and an outer Dewar (not shown) that contains liquid nitrogen. The "O" ring seal J between the cryostat and the inner helium Dewar is closed. For the initial cool down, liquid nitrogen is introduced through A into the inner Dewar and its vapor pressure is reduced to about 1/3 atm by pumping through L. For heat exchange the vacuum can O is filled with $^3$He gas to about 0.3 torr and the cryostat is left to cool over night to about 65 K. The liquid nitrogen remaining in the inner Dewar is removed by pressurizing the Dewar with $^4$He and forcing the liquid out through a siphon inserted through A. (Precooling the cryostat from about 80 to about 65 K reduces the liquid helium required for cooling by about two liters.) Six to seven liters of liquid helium are usually required to cool the apparatus from 65 to 4.2 K and fill the inner Dewar.

As part of the test, the resistance of the prt is first measured near 4.2 K with the $^3$He exchange gas in the vacuum can O. For the measurements in the range 13 to 90 K the $^3$He gas is removed by pumping and the temperature of the copper comparison block is stabilized by controlling the temperature of the thermal shields relative to the block. The temperature of the shields is controlled automatically by employing an amplifier and three-mode controller between each of the three five-junction Chromel P/constantan differential thermopiles and their corresponding shield heaters. The heaters and thermopiles are located on Q, R, and S of figure 2. R controls primarily the heat transfer up the stainless steel well F from the comparison block. Q controls the temperature of the leads and the central support tube. S is the thermal shield from R down and around the comparison block.

[2] Certain commercial materials are identified in this paper in order to adequately specify the experimental procedure. In no case does such identification imply recommendation or endorsement by the National Bureau of Standards, nor does it imply that the material identified is necessarily the best available for the purpose.

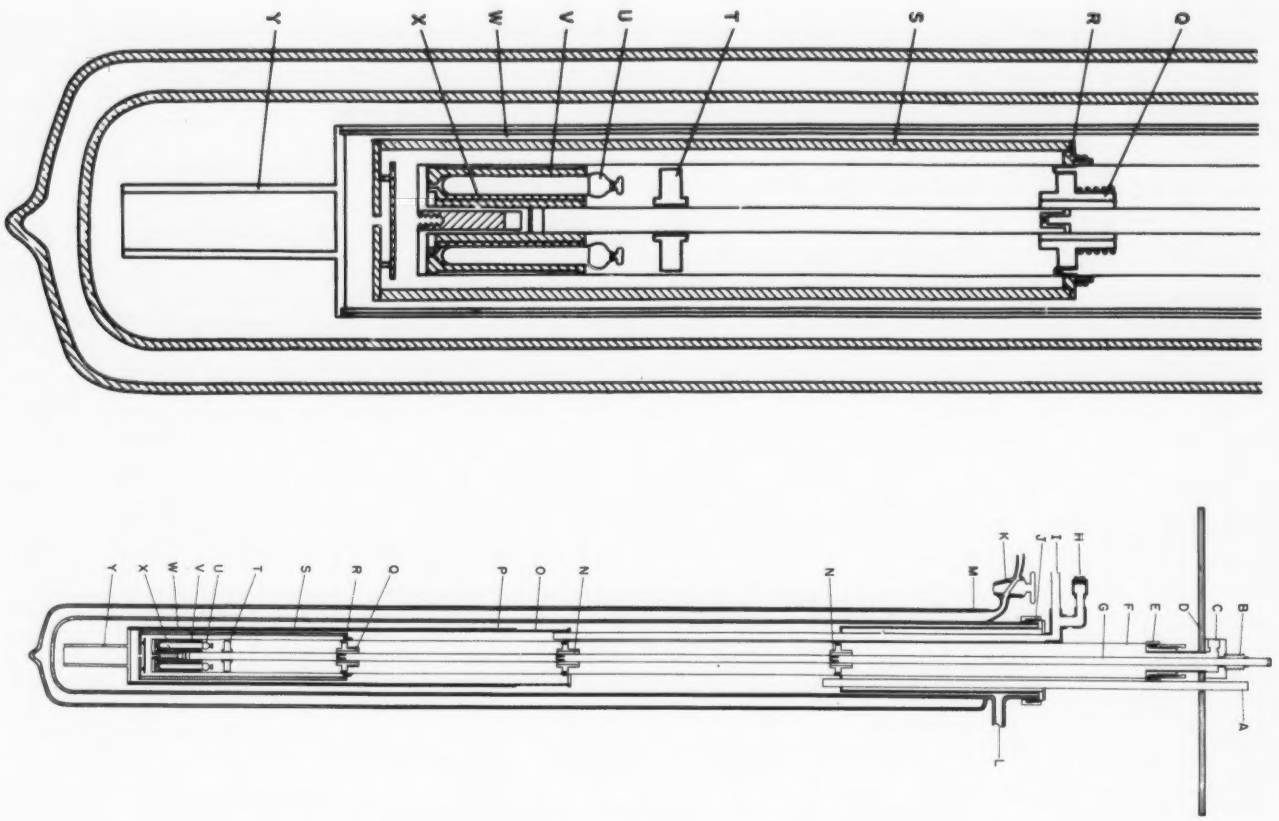


FIGURE 2. *Cryostat for the intercomparison of capsule type SPRT's.*

A. Guide for directing transfer tube into liquid helium Dewar.
B. Metal bellows to permit differential expansion between the central tube and the supporting thermometer block well.
C. Exit for the vacuum line and electrical leads to the thermometers, the thermocouples, and the heater on the copper thermometer block.
D. Supporting shelf.
E. Demountable "O" ring seal to the well around the thermometer block.
F. Well around the thermometer block.
G. Central tube for supporting the thermometer block.
H. Seal for the electrical leads from the vacuum can that surrounds the shield and lower portion of the thermometer block well.
I. Line from vacuum can "O".
J. Demountable "O" ring seal to the liquid helium Dewar.
K. Glass stopcock to permit reevacuation of liquid helium Dewar.
L. Line for pumping the space within the liquid helium Dewar.
M. Liquid helium Dewar.
N. Thermal tie-down for lead wires.
O. Vacuum can that surrounds the lower portion of the thermometer block well and the thermal shield.
P. Copper sleeve on vacuum can to maintain uniform temperature when liquid helium level is low.
Q. Thermal tie-down for leads similar to N with a heater and five-junction Chromel-P/constantan thermocouple for temperature control.
R. Copper ring on the thermometer block well with temperature control components similar to Q.
S. Heavy copper shield with temperature control components similar to Q.
T. Thermometer lead terminal block of anodized aluminum.
U. Capsule type platinum resistance thermometers thermally attached to copper block with vacuum grease.
V. Copper thermometer block with holes for six thermometers.
W. Location of thermocouple junctions placed on shield.
X. Reentrant "thumb" in the bottom of well. "Thumb" contains reference junctions for thermocouples on R and S.
Y. Heavy copper tail on vacuum can to reach liquid helium at a low level.

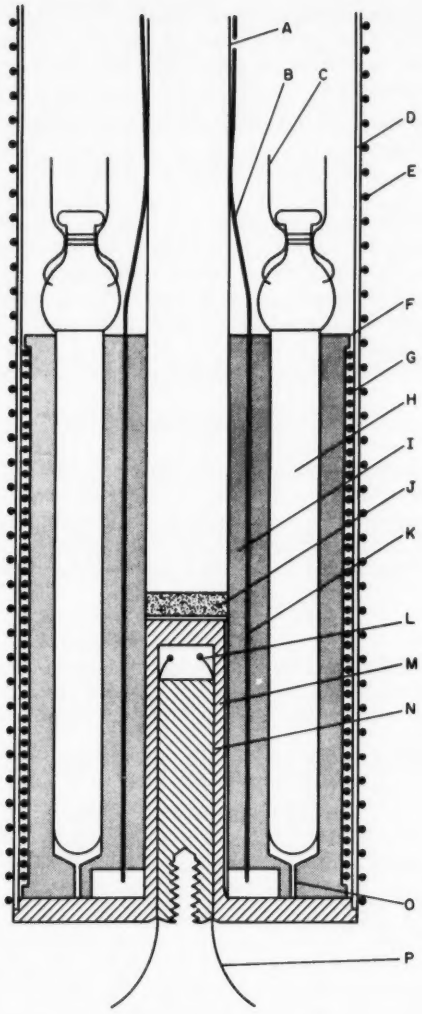


FIGURE 3. *Thermometer comparison block.*

A. Stainless steel tube to support thermometer comparison block.
B. Manganin leads for thermometers and copper leads for block heater.
C. Platinum leads of resistance thermometer.
D. Stainless steel well for thermometer block.
E. Heater distributed along well "D".
F. Copper thermometer block with wells for six thermometers.
G. Heater for thermometer block.
H. Platinum resistance thermometer.
I. Copper sleeve (attached to central supporting tube) with longitudinal grooves to serve as thermal tie-downs for manganin leads and thermocouples.
J. Brass plug to seal end of central support tube.
K. Location of grooves in sleeve "I".
L. Reference junctions for thermocouples on shield (at "W" in fig. 2) and thermometer block well ring heater (at "R" in fig. 2).
M. Closely fitted reentrant copper "thumb" (with a groove for venting gas).
N. Copper plug with longitudinal grooves to serve as thermal tie-downs for thermocouples.
O. Vent.
P. Thermocouple leads to shield and thermometer block well ring heater.

A heater wire wound directly on the copper comparison block is used to change its temperature to the next higher measurement temperature. Because of the low thermal diffusivity of stainless steel, a heater wire is also wound on the support tube to raise its

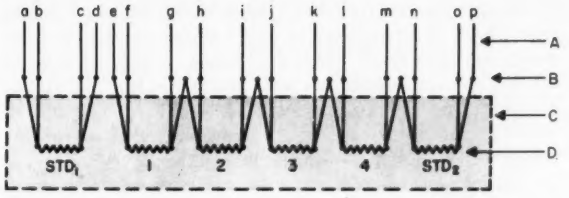


FIGURE 4. *Schematic of wiring capsule-type platinum resistance thermometers in the copper comparison block of the cryostat for calibration.*

To avoid excessive heating of the copper block, the bridge connections to the thermometers, wired in series, are made as follows:

| SPRT | Leads used |
|---|---|
| 1 | efgh |
| 2 | ghij |
| 3 | ijkl |
| 4 | klmn |
| $STD_2$ | mnop |

A. Cryostat leads.
B. Thermometer connections made among them and with the cryostat leads.
C. Schematic of the copper comparison block.
D. Platinum resistance thermometers. $STD_1$ and $STD_2$ are reference standards; others are to be calibrated.

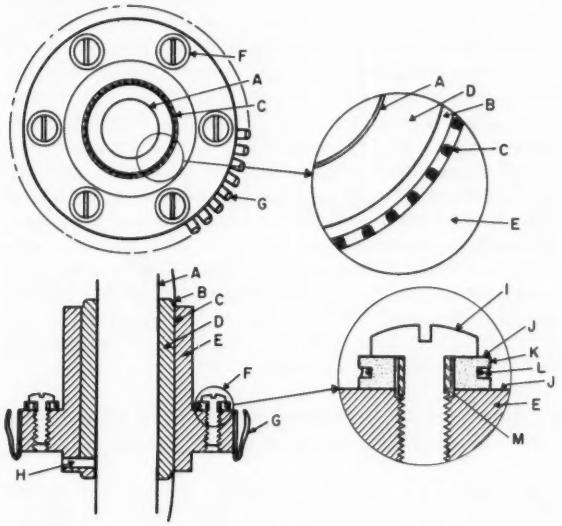


FIGURE 5. *Thermal tie-downs.*

A. Central support tube (stainless steel) for thermometer block.
B. Rounded corner, tangent to the bottom of the grooves for wire.
C. Round bottom grooves in cylinder "D" with wire cemented in place.
D. Copper cylinder soldered (tin-lead eutectic) to the central support tube.
E. Copper cylinder fitted to "D" and held in place by pin "H".
F. Thermocouple tie-down.
G. Spring fingers of beryllium copper heavily silver plated and gold "flashed".
H. 1.5 mm steel pin to hold cylinder "E" in position.
I. Pan head 2–56 brass screw to clamp thermocouple tie-down assembly to "E".
J. Insulating washer of 0.005 mm Mylar coated with vacuum grease.
K. Copper washer with pretinned groove for thermocouple wire.
L. Polyimide insulated thermocouple wire, placed at the bottom of the pretinned groove and "potted" in eutectic tin-lead solder.
M. Epoxy insulation on screw.

temperature whenever the temperatures of the comparison block and Q are raised. When the block is being heated above about 40 K, the limitations of the

power amplifiers that are presently being used cause the shield temperature to lag behind the block temperature; however, when the block heater is turned off the power amplifiers are adequate for the shield temperature to equalize rapidly to that of the block. After termination of heating the time required for the comparison block to attain temperature equilibrium increases with temperature. At 13.8 K the thermometer drift will decrease to less than 10 $\mu\Omega$/min in 1 min; however, at 90 K more than 30 min are required before this temperature drift rate can be reached. Measurements are considered unsatisfactory if the thermometer drift is more than 5 $\mu\Omega$/min below 20 K or more than 10 $\mu\Omega$/min above 20 K.

The simultaneous measurements of each test prt and the first standard are made at 16 temperatures which are approximately 12.20, 13.81, 15.42, 17.34, 18.66, 20.28, 23.69, 27.102, 33.92, 40.75, 47.55, 54.361, 66.30, 78.24, 84.22, and 90.188 K. The measurements at these temperatures provide one to three intermediate points between the defining fixed points. The intercomparison of the first and second standards is usually made only at temperatures close to the fixed points. At each temperature a series of simultaneous measurements of the two prt's is carried out as rapidly as possible with a continuous current of 1 mA and with the Mueller bridge commutator placed successively in positions NRRNNRRN. At approximately 90.2 K, the self-heating effect of the prt is determined by making measurements at 1 mA and at 2 mA. (Immediately after the prt is installed in the cryostat, the space around the copper block is evacuated and the prt is tested for any excessive self-heating effects. If the metal-to-glass seal of the capsule develops a leak, the helium exchange gas in the capsule is lost. Such a prt will have a large self-heating effect in a vacuum environment and is considered unreliable.) In the cryostat the total self-heating effect observed at 90 K is normally from 0.05 to 0.2 mK/(mA)$^2$, depending upon the thermometer design.

## 4. Analysis of Platinum Resistance Thermometer Relations of the IPTS–68

In the IPTS–68 the specified formulae for evaluating temperatures employing the standard prt are such that the resistance versus temperature relation of a prt at any temperature (except at the defining fixed points) is influenced by *all* calibration points above that temperature. The following is a brief outline of the relation among the five sub-ranges of the IPTS–68 which are defined in terms of the prt.

Below 0 °C, as mentioned in the introduction, the values of temperature ($T$) on the IPTS–68 are defined by eq (1) which gives the observed resistance ratio $W(T)$ as the sum of the reference function $W^*(T)$ (eq 2)) and the deviation function $\Delta W(T)$. The deviation function $\Delta W(T)$ is defined by a polynomial in $T$ and the coefficients of the terms are determined from the deviation of the measured values of $W(T)$ from the reference function values, $W^*(T)$, at the appropriate defining fixed points. Furthermore, the coefficients are constrained by the requirement that the first derivative of successive deviation functions be continuous at the points of joining below 0 °C.

(a) From 13.81 to 20.28 K the deviation function is

$$\Delta W(T) = A_1 + B_1 T + C_1 T^2 + D_1 T^3. \quad (5)$$

The coefficients are determined from the measured deviation, $W(T) - W^*(T)$, at the TP, the equilibrium temperature between liquid and vapor at 25/76 standard atmosphere, and the NBP of equilibrium hydrogen (e-$H_2$), and by the derivative at the NBP of e-$H_2$ of eq (6).

(b) From 20.28 to 54.361 K the deviation function is

$$\Delta W(T) = A_2 + B_2 T + C_2 T^2 + D_2 T^3. \quad (6)$$

The coefficients are determined from the measured deviation, $W(T) - W^*(T)$, at the NBP of e-$H_2$, NBP of neon of natural composition, and the TP of oxygen, and by the derivative at the TP of oxygen of eq (7).

(c) From 54.361 to 90.188 K the deviation function is

$$\Delta W(T) = A_3 + B_3 T + C_3 T^2. \quad (7)$$

The coefficients are determined from the measured deviation, $W(T) - W^*(T)$, at the TP and NBP of oxygen, and by the derivative at the NBP of oxygen of eq (8).

(d) From 90.188 to 273.15 K the deviation function is

$$\Delta W(T) = A_4 t + C_4 t^3 (t - 100). \quad (8)$$

The coefficients are determined from the measured deviation, $W(T) - W^*(T)$, at the NBP of oxygen and the NPB of water. (By definition, $t = T - 273.15$ K.) $W(100\ °C)$ for the prt may be calculated from eq (4) or (9), if the tin and zinc points are employed in the thermometer calibration. $W^*(100\ °C)$ is calculated from eq (4) or (9) employing thermometer "constants" $\alpha^*$ and $\delta^*$, which are to be described in the next paragraph.

As outlined in the introduction, from 0 °C (273.15 K) to 630.74 °C (903.89 K) the values of temperature on the IPTS–68 are defined by eqs (3) and (4). The relation shown in eq (4) may be expressed in the equivalent form

$$W(t') = 1 + At' + Bt'^2, \quad (9)$$

where

$$A = \alpha(1 + \delta/100), \quad (10)$$

and

$$B = -\alpha\delta \times 10^{-4}. \quad (11)$$

Also, from eqs (10) and (11)

$$\alpha = (A + 100\,B), \quad (12)$$

and

$$\delta = -B \times 10^4/(A + 100\,B). \quad (13)$$

It follows from eq (4) that

$$\alpha = [W(100\ ^\circ\text{C}) - 1]/100. \tag{14}$$

At $T = 273.15$ K (or $t = 0$ °C) the reference function eq (2) and its first and second derivatives are continuous with eq (9) (or eq (4)) for $\alpha = 3.9259668 \times 10^{-3}$ °C$^{-1}$ and $\delta = 1.496334$ °C. (Hereafter, these values will be referred to as $\alpha^*$ and $\delta^*$, respectively.) However, the first derivatives of real prt's are not continuous at 0 °C [27]. The discontinuity is expected to be at most about $3 \times 10^{-8}$ °C$^{-1}$ or 0.0008 percent and, therefore, can be neglected for most purposes.

The contribution of $\alpha$ to the calibration of the prt in the subranges below 0 °C will be demonstrated in the following. From eq (4) or (14)

$$W(100\ ^\circ\text{C}) = 100\alpha + 1, \tag{15}$$

and

$$W^*(100\ ^\circ\text{C}) = 100\alpha^* + 1. \tag{16}$$

Subtracting eq (16) from eq (15) and substituting in eq (8) at 100 °C, there results

$$A_4 = \alpha - \alpha^*. \tag{17}$$

When eq (8) is solved for $C_4$ at $t_{O_2}$,

$$C_4 = (\Delta W(t_{O_2}) - A_4 t_{O_2})/t_{O_2}^3\,(t_{O_2} - 100). \tag{18}$$

Thus, both coefficients $A_4$ and $C_4$ of eq (8) are affected by the value of $\alpha$. The derivative of eq (8) is

$$d\,[\Delta W(t)]/dt = A_4 + 4C_4 t^2\,(t - 75). \tag{19}$$

The values of $A_4$ and $C_4$ of the 28 capsule type prt's, that have been calibrated during the last 2 1/2 years at NBS, ranged from $-7.900 \times 10^{-7}$ to $+1.0833 \times 10^{-6}$ and from $-2.27_{40} \times 10^{-14}$ to $+2.31_{20} \times 10^{-14}$, respectively. (The coefficients $A_4$ and $C_4$ of 166 long stem prt's, that have been obtained over the same period by calibration at the TP of water, tin and zinc points, and the NBP of oxygen, ranged from $-9.668 \times 10^{-7}$ to $+1.3108 \times 10^{-6}$ and $-5.26_{12} \times 10^{-15}$ to $+3.04_{37} \times 10^{-14}$, respectively.) Since the factor $4t^2(t - 75)$ becomes about $-3 \times 10^7$ at the oxygen point, the two terms of eq (19) can be comparable in magnitude at that temperature. When eq (19) is expressed in terms of the measured quantities $A_4$ and $W(T_{O_2})$ by substituting eq (18) for $C_4$, there is obtained

$$\{d[\Delta W(T)]/dt\}_{O_2} = \frac{4\Delta W(t_{O_2})\,(t_{O_2} - 75) - A_4 t_{O_2}(3t_{O_2} - 200)}{t_{O_2}(t_{O_2} - 100)}. \tag{20}$$

When $-182.962$ °C is substituted for $t_{O_2}$, eq (20) becomes

$$\{d[\Delta W(T)]/dt\}_{O_2} = -(2.64659_6 A_4 + 0.0199308_9 \Delta W(t_{O_2})). \tag{21}$$

Again, since $\Delta W(t_{O_2})$ ranges from about $-2.0 \times 10^{-4}$ to $+1 \times 10^{-4}$, the contribution of $A_4$ to the derivative at the oxygen point can be comparable to that of the measured value of $\Delta W(t_{O_2})$. (The values of $A_4$ and $\Delta W(t_{O_2})$ have been found to be closely connected. When $A_4$ is relatively large, i.e., when $\alpha$ is relatively large, $\Delta W(t_{O_2})$ is negatively larger; when $A_4$ is minus, $\Delta W(t_{O_2})$ is positive.)

The capsule type prt's are calibrated first at the TP of water and at the tin point before calibrating in the region of 13 to 90 K. Because of the possible damage and the electrical leakage across the metal-glass lead seal at high temperatures, the capsule type prt's are not calibrated at the zinc point as is routinely done with long-stem type prt's. The capsule type prt's are also not given any annealing treatment at NBS. The calibration sequence consists of measurements at the TP of water, tin point, TP of water, and the 13 to 90 K range. To obtain $\alpha$ from the calibration measurements at the TP of water and the tin point, an average value of $B$ (approximately $-5.8755 \times 10^{-7}$ °C$^{-2}$) is employed which is based on the values obtained earlier on 203 long-stem type prt's. The range of values of $B$ on the long-stem type prt's is $5 \times 10^{-10}$ °C$^{-2}$. From eq (12)

$$\frac{d\alpha}{dB} = \frac{dA}{dB} + 100 \tag{22}$$

and at the tin point from eq (9)

$$\frac{dA}{dB} = -231.9292; \tag{23}$$

thus

$$d\alpha = -131.9292\,dB. \tag{24}$$

Therefore, by choosing the mean value of $B$ there would be an uncertainty in $\alpha$ (or in $A_4$) of about $\pm 3 \times 10^{-8}$ °C$^{-1}$ (equivalent to about 1 mK at the NBP of water). (A survey of the values of $B$ obtained on long-stem prt's that were received during the last 2½ years shows the average to be closer to $-5.8768 \times 10^{-7}$ °C$^{-2}$ and the range to be about $4 \times 10^{-10}$ °C$^{-2}$.) A survey of 28 capsule type prt's shows that the derivatives at the NBP of oxygen of the deviation functions could be $3 \times 10^{-8}$ °C$^{-1}$ or smaller. This indicates that the value of the derivative of the deviation function at the oxygen point could be obscured by the uncertainty in the value of $B$ that is used.

An error in the realization of the NBP of water (or in the calculated value of $W(100\ ^\circ\text{C})$ because of the

calibration error at the tin point) results in an error in the value of $\alpha$. From eq (14)

$$d\alpha/dt' = (1/100)\ dW(100\ ^\circ\text{C})/dt' \tag{25}$$

and from eq (9)

$$dW/dt' = A + 2Bt'. \tag{26}$$

Thus,

$$d\alpha = (1/100)\,(A + 200B)\ dt'. \tag{27}$$

Since $A$ is about $3.98 \times 10^{-3}\ ^\circ\text{C}^{-1}$ and $B$ is about $-5.87 \times 10^{-7}\ ^\circ\text{C}^{-2}$,

$$d\alpha \sim 3.86 \times 10^{-5}\ dt. \tag{28}$$

($dt'$ is replaced by $dt$ in this approximation because at 100 °C $dt/dt'$ is about 1.0003; see eq (3).) Thus, the uncertainty in $\alpha$ of $\pm 3 \times 10^{-8}\ ^\circ\text{C}^{-1}$, caused by employing the mean value of $B$, is equivalent to an uncertainty of about ± 1 mK in the realization of the NBP of water. Reproducibilities of ± 0.1 mK to ± 1 mK have been reported for the NBP of water [28, 29], indicating that the uncertainty in $B$ is comparable to the reproducibility of the NBP of water.

The effect of an error in the realization of the tin point on the value of $\alpha$ is shown by the following. When eq (9) is substituted for $A$ in eq (12), there is obtained

$$\alpha = \frac{(W-1)}{t'} + B(100 - t'). \tag{29}$$

When eq (29) is differentiated with respect to $W$,

$$d\alpha = dW/t', \tag{30}$$

if an assumed average $B$ is used. By substituting eq (9) for $A$ in eq (26), the effect of a change in temperature on $W$ is obtained as

$$dW = \left[\frac{W-1}{t'} + Bt'\right]dt'. \tag{31}$$

The substitution of eq (31) for $dW$ in eq (30) gives

$$d\alpha = \left[\frac{W-1}{t'^2} + B\right]dt'. \tag{32}$$

At the tin point, $W$ is approximately 1.892, $dt/dt'$ is about 1.0002, and since $B$ is about $-5.876 \times 10^{-7}\ ^\circ\text{C}^{-2}$, eq (32) becomes

$$d\alpha = 1.6 \times 10^{-5} dt, \tag{33}$$

which shows that the effect on $\alpha$ (or $A_4$) of a unit error of temperature at the tin point (if using an assumed value of $B$) is about 0.4 of that at the NBP of water.

The foregoing analysis shows that the errors of calibration above 0 °C could contribute a *relatively* large effect on the derivative of the deviation function at the oxygen point. However, the errors of computed temperatures in the region below 0 °C is determined by the *absolute* magnitude of the error in the value of the deviation functions. From eq (2)

$$\delta T = (dT/dW^*(T))\ \delta W^*(T)$$

$$= \frac{\delta W^*(T)}{W^*(T)} \sum_{i=1}^{20} iA_i\,[\ln W^*(T)]^{i-1}, \tag{34}$$

and from eq (1)

$$\delta W^*(T) = -\delta \Delta W(T). \tag{35}$$

(The effect of the error of resistance ratio measurement $\delta W(T)$ by the user of the prt is not considered in this discussion; this error can be best estimated by the user and combined with the error of calibration $\delta \Delta W(t)$ to determine the overall error.) In the region of 13 to 90 K, $dT/dW^*(T)$ ranges from about 4918 to 230 K so that the error $\delta \Delta W(t)$ must be smaller than $2 \times 10^{-7}$ at 13 K and smaller than $4 \times 10^{-6}$ at 90 K for the temperature error $\delta T$ to be 1 mK or less. This corresponds to the resistance reading error of a standard prt, with an $R$ (0 °C) of 25 Ω, to be less than $5 \times 10^{-6}$ Ω at 13 K and less than $1 \times 10^{-5}$ Ω at 90 K. The effect of the error in the deviation, $\Delta W(t)_{O_2}$, at the NBP of oxygen on the final deviation functions between 13 and 90 K was analyzed by numerical techniques using a computer.

The data (16 points) from the comparison measurements, obtained as described in the section, "Design and Operation of the Cryostat," are processed by a computer employing a least squares technique in which the derivatives of the four polynomial deviation equations are constrained to be equal at the point of their joining as outlined earlier, i.e., at 20.28 K (NBP of e-$H_2$), at 54.361 K (TP of oxygen), and 90.188 K (NBP of oxygen). The analysis yields the "best values" of $\Delta W$ (or $W$) at the fixed points for the respective prt's which are then used to obtain the polynomial deviation functions of the IPTS–68 and then to evaluate tables of $W$ or $R$ versus $T$. This method, which is employed in processing the 16 observations obtained on all capsule type prt's that are received for calibration at NBS, will be referred to in this paper as the least squares method.

The comparison measurements include observations within 0.02 or 0.03 K of the defining fixed point temperatures; they deviate at most by 0.3 K. In the second method of analysis the points close to the fixed points were "extrapolated," without the use of the observations at the intermediate temperatures, to the appropriate fixed points to obtain $W$ and then the $\Delta W$. The IPTS–68 deviation functions were derived from these extrapolated values. This method of analysis will be referred to as the fixed-point method. This analysis procedure illustrates the case when only the defining fixed points are employed in calibrating prt's.

In the analysis of the interrelationship of the deviation functions of the IPTS–68 for prt presented here, the calibration obtained on a typical capsule type prt was taken to be "perfect." Various types of errors, to be subsequently described, were introduced into the calibration of this prt and the results are compared with the results of the "perfect" calibration. Plots show the temperature difference or the deviations between the two "calibrations."

A computer analysis was made in terms of how a unit positive error of temperature in the realization of the NBP of water is reflected in the reduction of the calibration data in the region of 13 to 90 K. The results are shown in figure 6. The effect of the error is shown to be attenuated and is smaller between about 30 and 87 K for the least squares treatment of the data than for the fixed point treatment but at other temperatures the effect is larger for the least square method. Since

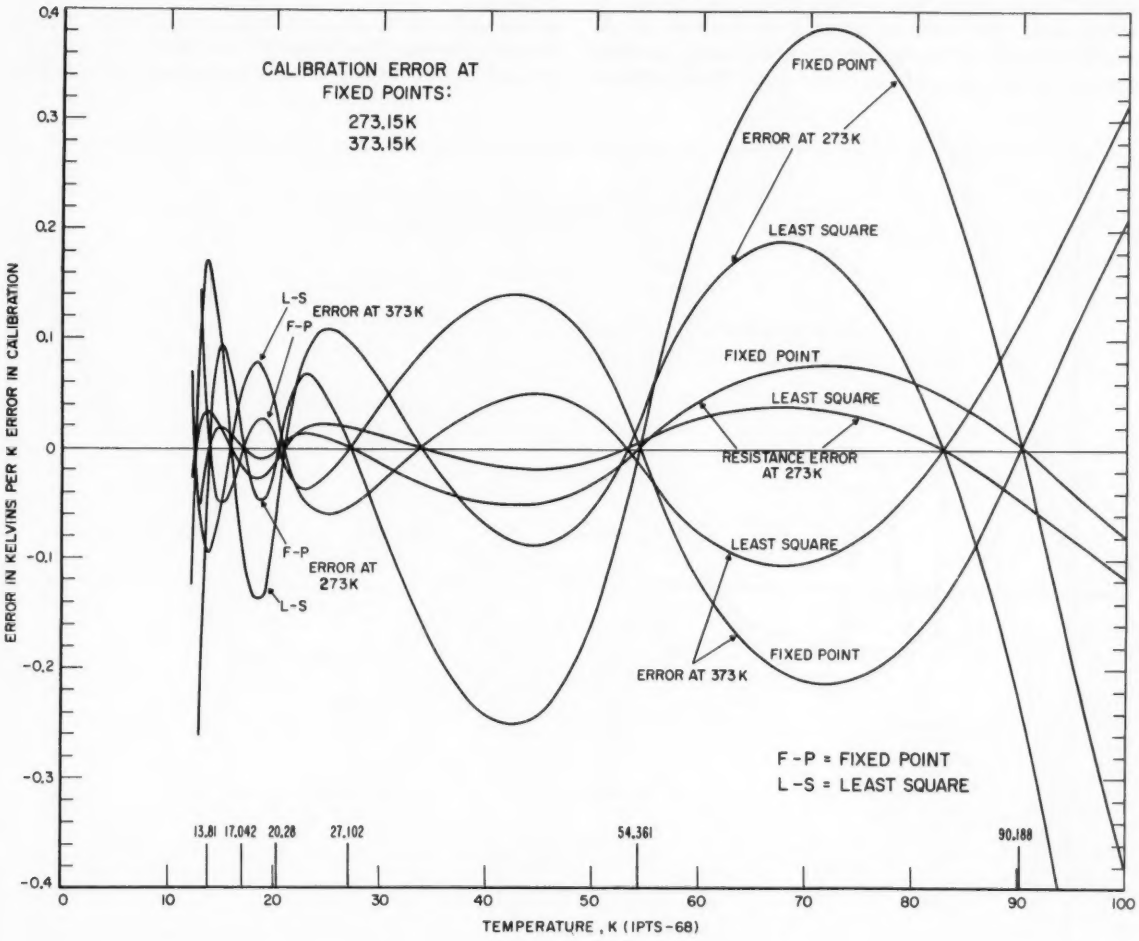


FIGURE 6. *The effect of errors in the realization of the fixed points above 0* °C on the calibration of a platinum resistance thermometer in the region 13 K to 90 K.

The errors introduced in the calibration when the least squares treatment is employed is compared with those of the fixed point treatment of the same data. The effects of errors equivalent to unit positive temperature in the realization of the TP and of the NBP of water are each plotted. The resulting errors are also shown when an error in $R(0\ °C)$ equiivalent to a unit positive temperature is made but no error in $\alpha$ is made.

the least squares method involves the minimization of the absolute error in $W$, the relatively large deviations at the lower temperatures shown in figure 6 reflect the increased sensitivity in $\partial t/\partial W^*(t)$ at these temperatures. These relatively large temperature deviations at the lower temperatures will be seen in other figures. There is shown also in figure 6 how a unit positive error of temperature in the realization of the TP of water is reflected in the reduction of the calibration data in the region of 13 to 90 K. This measurement error causes an error in $\alpha$ and in $R(0\ ^\circ C)$. Figure 6 shows also the effect of resistance error in $R(0\ ^\circ C)$ corresponding to a unit positive error of temperature, but with no error in $\alpha$. In general the results obtained in the latter two cases with the least squares treatment and the fixed point treatment are very similar to those obtained with an error at the NBP of water. As pointed out earlier, in employing the average value of $B$ in the calibration of capsule prt's there results an uncertainty equivalent to an uncertainty of $\pm 1$ mK in the realization of the NBP of water. Figure 6 shows that this uncertainty corresponds to less than 0.1 mK over most of the 13 to 90 K range. In the least squares treatment the error would amount to about 0.1 mK at 65 and 90 K.

For the least squares treatment, the effect of taking additional observations below 90 K was examined as a possibility to reduce the influence of the calibration errors above 0 °C. Figure 7 shows the results of three times more data between 54 and 90 K and between 13 and 20 K. The additional data between 54 and 90 K

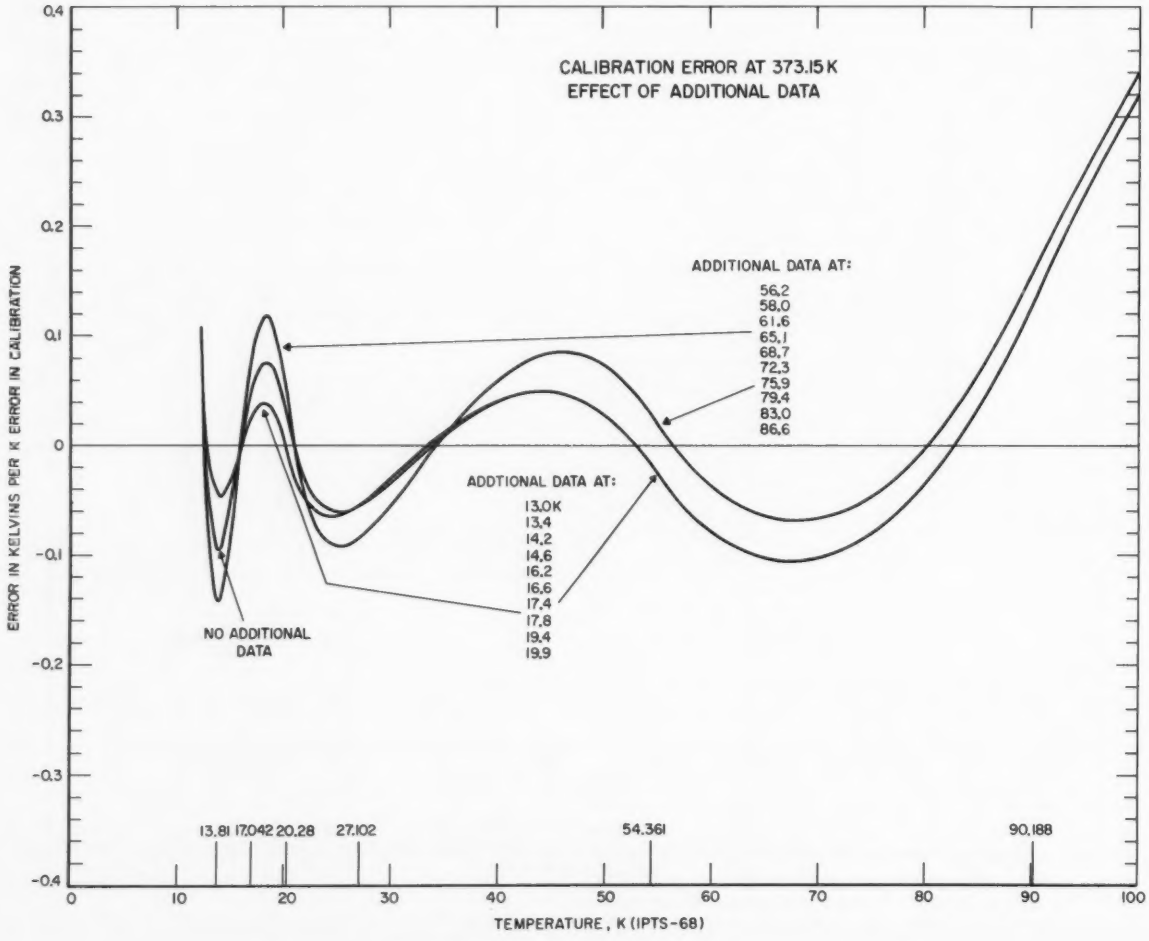


FIGURE 7. *The effect of three times more data in the region 13 to 20 K and the effect of three times more data in the region 54 K to 90 K on the results of least squares treatment of the calibration data with an error equivalent to unit positive temperature at the NBP of water.*

The plot gives the deviations of the values of temperatures of the calibration with error from those of the calibration without error.

make relatively small improvement on the deviations above about 50 K and make the deviation worse below 50 K. The additional data between 13 and 20 K result in significant reduction of the deviations between 13 and 40 K and very little change in the deviations above about 50 K.

Figures 8 and 9 show the effect of unit positive error in the realization of the fixed-point temperatures at 90.188, 54.361, 27.102, 20.28, 17.042, and 13.81 K. The results of both least squares and fixed point treatments are shown. The least squares treatment propagates the errors both upward and downward and causes relatively larger deviations at the lower temperatures than the fixed-point treatment. However, the overall average deviation is smaller for the least squares method.

The least squares treatment of error of observation at temperatures between the fixed points was also examined. Figure 10 shows that the error is attenuated significantly although the error is propagated to other temperature regions, particularly to lower temperatures. The error at 15.4 K is reduced to 46 percent, that at 18.6 K to 37 percent, that at 23.7 K to 26 percent, that at 40.7 K to 28 percent, and that at 78.2 K to 28 percent. Thus, considering only the possible measurement errors, the least squares analysis of the calibration data should yield better results than the fixed point method. Additional data at the lower temperatures, particularly below about 25 K, and increased weighting of these data should improve the results of the least squares treatment of calibration data.

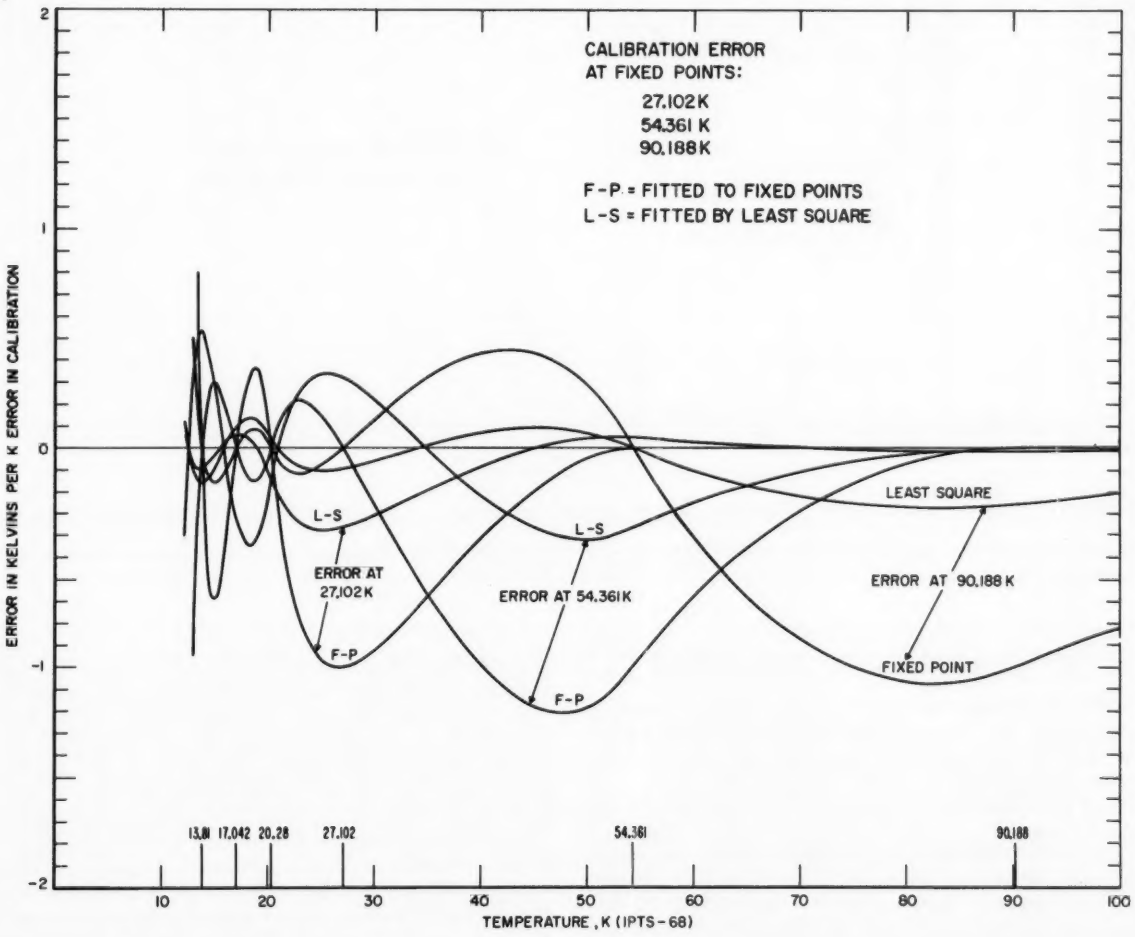


FIGURE 8. *The effect of an error in the realization of the fixed point on the calibration of platinum resistance thermometer in the region 13 to 90 K.*

The figure shows the resulting error with the least squares treatment and the resulting error with the fixed point treatment of the same data with an error equivalent to unit positive temperature at 90.188, at 54.361, and at 27.102 K.

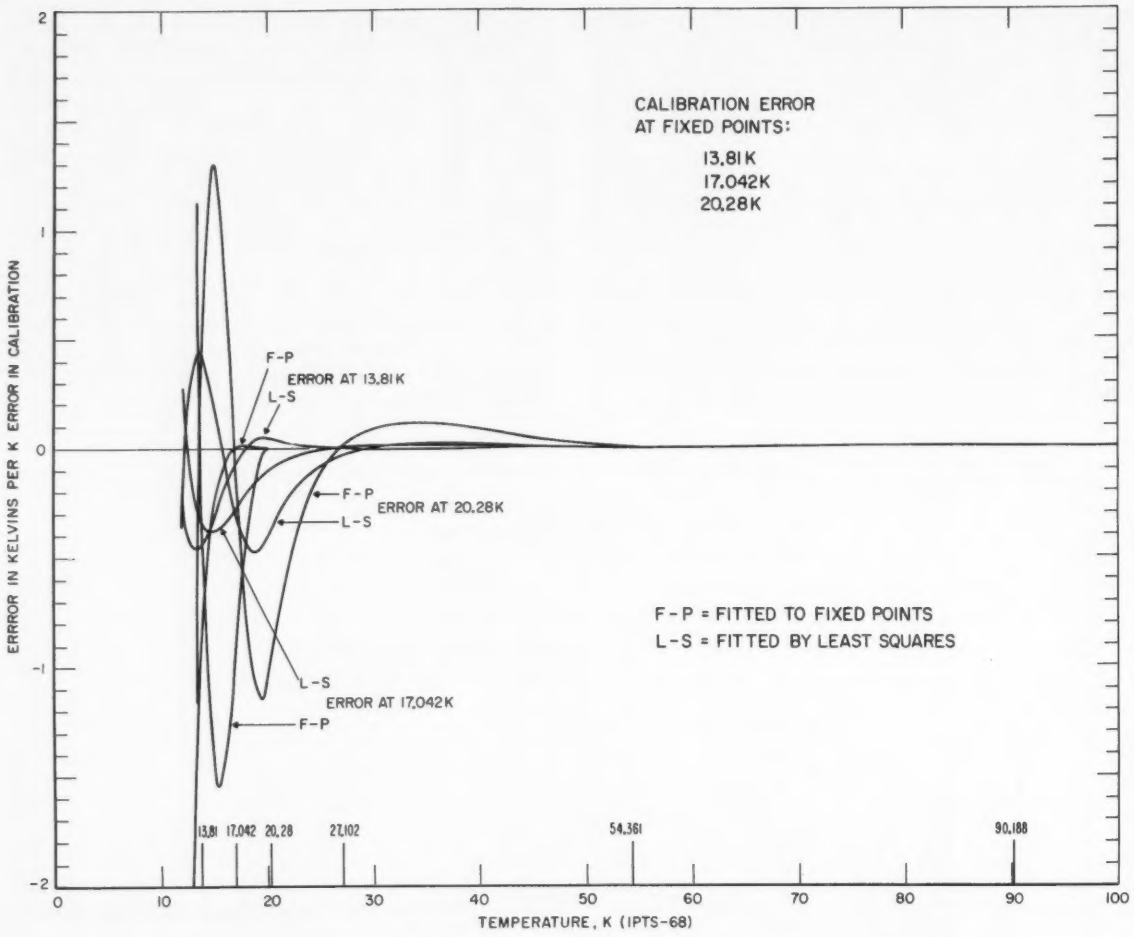


FIGURE 9. *The effect of an error in the realization of the fixed point on the calibration of platinum resistance thermometer in the region 13 to 90 K.*

The figure shows the resulting error with the least squares treatment and the resulting error with the fixed point treatment of the same data with an error equivalent to unit positive temperature at 20.28 K, at 17.042 K, and at 13.81 K.

## 5. Reproducibility of NBS–IPTS–68

The reduction of the calibration data involves calculating the temperature from the observed resistance of the reference standard and assigning this value of temperature to the simultaneously observed value of resistance of the prt being calibrated. The temperature of the reference standard prt is evaluated from its IPTS–68 deviation functions and the reference function in accordance with eqs (1) and (2). As described earlier, these observed resistance versus temperature data for the prt being calibrated are processed by the least squares method to obtain the "best" coefficients for the IPTS–68 deviation functions. These deviation functions are employed to compute the thermometer calibration table issued from NBS. The coefficients of the deviation functions for the prt are also issued as a part of the calibration service. The differences between the final tabular values and the observed resistance versus temperature data for the prt being calibrated are indicative of the quality of reproduction of the NBS–IPTS–68 by the prt. Systematic differences would indicate that the formulations being used do not adequately transfer the NBS–IPTS–68 to the prt being calibrated. A close similarity of these differences for different prt's indicates that the NBS–IPTS–68 scale is being transferred to the prt's in a similar manner. If many "wild" differences exist, the measurement process, which includes the cryostat, requires improvement. Obviously, if the differences are small, then the transfer of the NBS–IPTS–68 to the prt's is adequate.

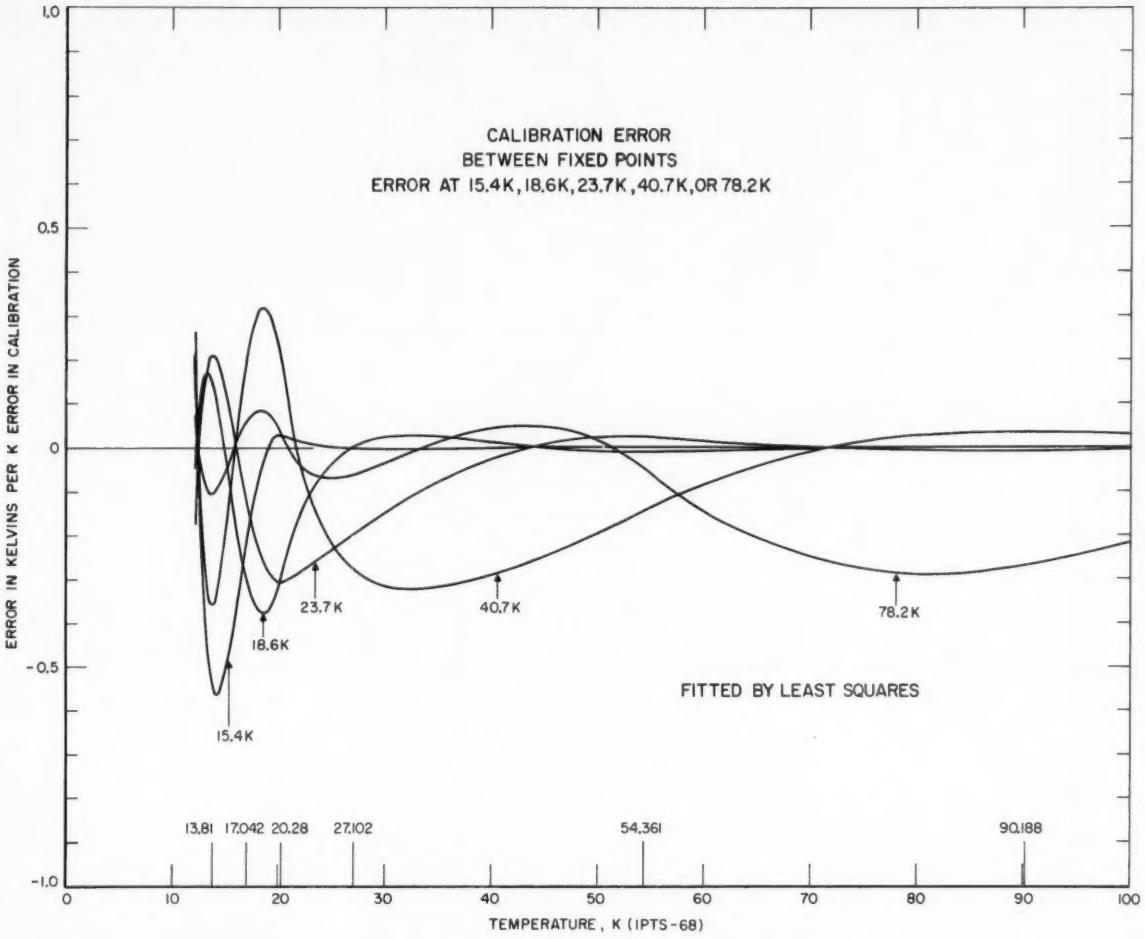


FIGURE 10. *The effect of an error in the calibration data at temperatures midway between the fixed points on the calibration of platinum resistance thermometer in the region 13 to 90 K.*

The figure shows the resulting error with the least squares treatment of the data with an error equivalent to unit positive temperature at 15.4 K, at 18.6 K, at 23.7 K, at 40.7 K, and at 78.2 K.

In the following discussion a series of plots of the differences between the calculated values and the observed values is shown to indicate the reproducibility of prt comparison calibrations performed at the NBS the past 2½ years since the present least squares computer program was initiated. In addition to the least squares method, the fixed point treatment described earlier was also used with the same data. The results of the latter method of analysis should indicate the reproducibility of the IPTS–68 for this group of thermometers.

A second reference standard prt is intercompared with the first standard in every group of thermometers calibrated. The comparisons are made at temperatures near the fixed points and occasionally at other temperatures. The coefficients of the IPTS–68 deviation functions have been derived for this second reference standard. Figure 11 shows the differences between the computed values of temperatures at the temperatures of intercomparison of the two reference standard prt's. The deviations, except for a few possible errors of recording of observations, indicate excellent precision in the calibration measurements.

Figures 12, 13, 14, 15, and 16 show the results of the least squares treatment of the calibration data. Between about 20 and 90 K the derived coefficients of the IPTS–68 deviation functions for the prt's yield temperature scales that generally agree within a few tenths of a mK with the NBS–IPTS–68. Between 13.8 and 20 K the differences become closer to about ±0.7 mK. A small systematic deviation is seen in the data above about 40 K. In some of the measurements a deviation as much as −1 mK is shown at 90 K; this is considered to be principally the result of relatively poor joining of the two deviation functions at 90.188 K and the relatively large deviations between 54 and 90 K in the

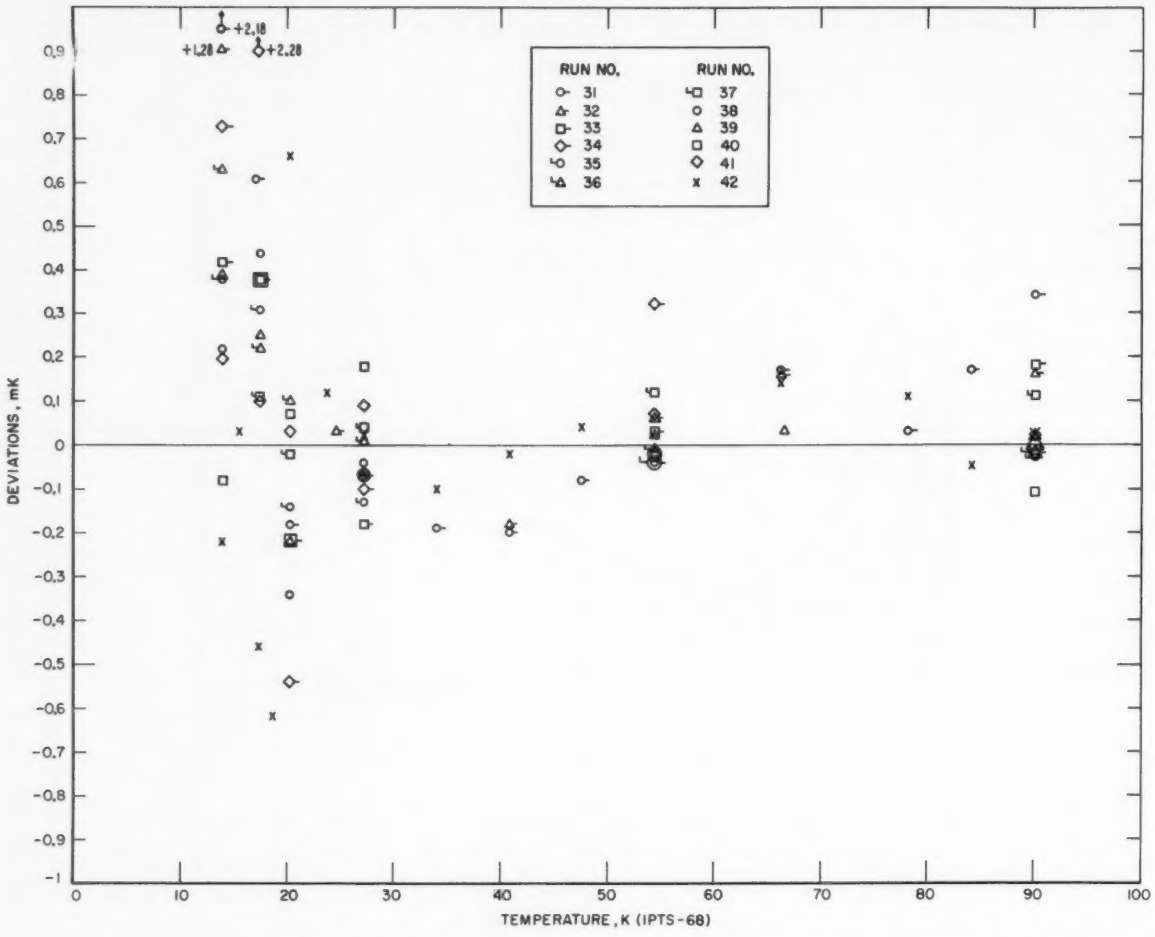


FIGURE 11. *Measured deviations of the values of temperatures of the second reference standard platinum resistance thermometer from those of the first reference standard.*

IPTS–68 formulation of the NBS–IPTS–68 scale (see figs. 17 and 18). In section 4 (see fig. 6) an error of realization of the NBP of water is shown to be attenuated by 1/10 at 90 K. An error in $\alpha$ equivalent to an error of 0.01 K at the NBP of water, because of possible error of measurements at the tin point or the use of average B, is considered unlikely. Further work is in progress to reduce these relatively large differences found for some thermometers.

Although there is some experimental scatter in the data, particularly below about 20 K, definite systematic differences are shown by the results of the fixed point treatment of the data (see figs. 17 and 18). Between 20.28 and 27.102 K the deviations are in general negative, between 27.102 and 54.361 K at first positive then negative, and between 54.361 and 90.188 K positive. Similar deviations in the reproducibility of the IPTS–68 have been reported by Bedford and Ma [30] and by Tiggelman and Durieux [31]. Except for a few observations that seem to deviate considerably more, the reproducibility of the NBS–IPTS–68 scale using the IPTS–68 fixed point treatment is well within $\pm 1$ mK. The relatively large differences of the fixed point treatment (see fig. 18) are reduced by the least squares treatment (see fig. 16).

## 6. Conclusion

The calibration procedure employed at the NBS for capsule type prt's reproduces the NBS–IPTS–68 scale maintained on reference standard prt's within a few tenths of a mK between about 20 and 90.188 K and within about $\pm 1$ mK between 13.81 and 20 K. The results of the fixed point treatment of the same calibration data, rather than the least squares method normally employed at the National Bureau of Standards, exhibit in general larger systematic deviation from the NBS–IPTS–68 than the results of the least squares

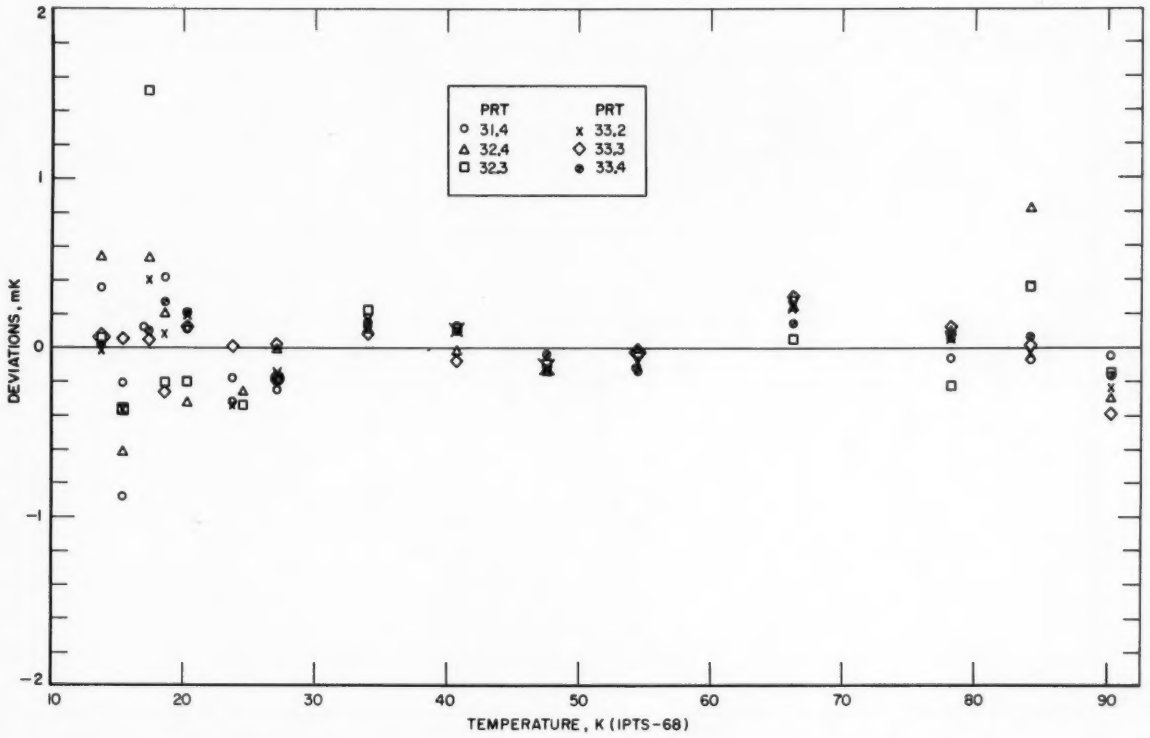


FIGURE 12. *The measured deviations of the values of temperatures, given by the IPTS–68 formulations obtained for each thermometer by the least squares treatment of the calibration data, from those of the NBS–IPTS–68 scale at temperatures of intercomparison with the reference standard.*



496-895 OL - 73 - 2

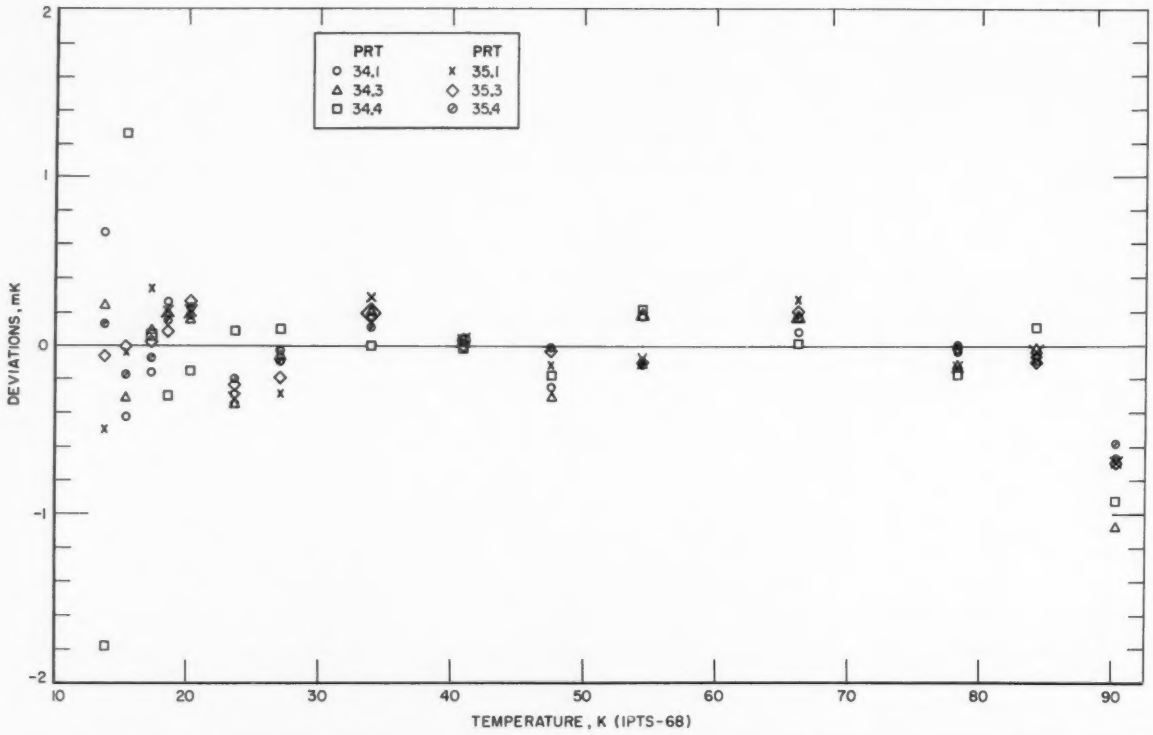


FIGURE 13. *The measured deviations of the values of temperatures, given by the IPTS–68 formulations obtained for each thermometer by the least squares treatment of the calibration data, from those of the NBS–IPTS–68 scale at temperatures of intercomparison with the reference standard.*

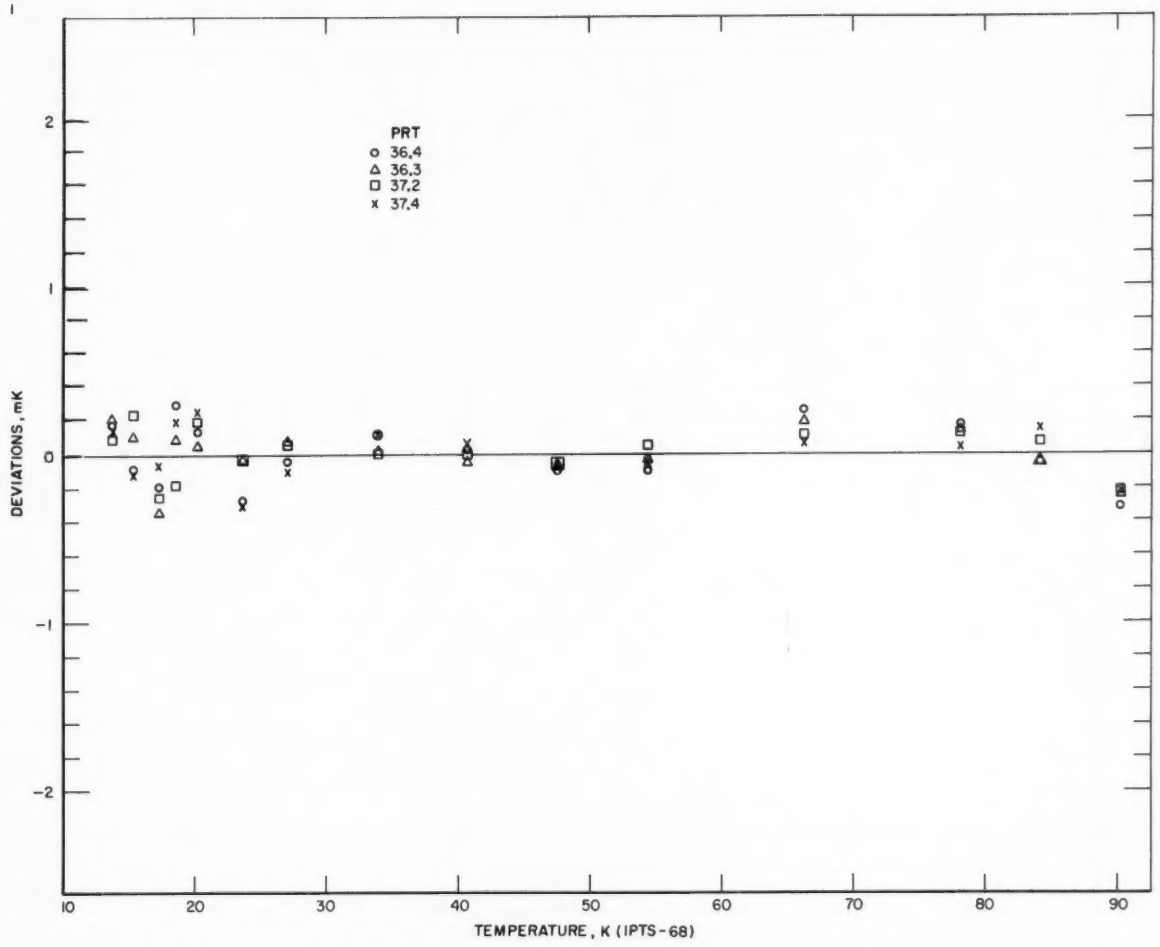


FIGURE 14. *The measured deviations of the values of temperatures, given by the IPTS–68 formulations obtained for each thermometer by the least squares treatment of the calibration data, from those of the NBS–IPTS–68 scale at temperatures of intercomparison with the reference standard.*

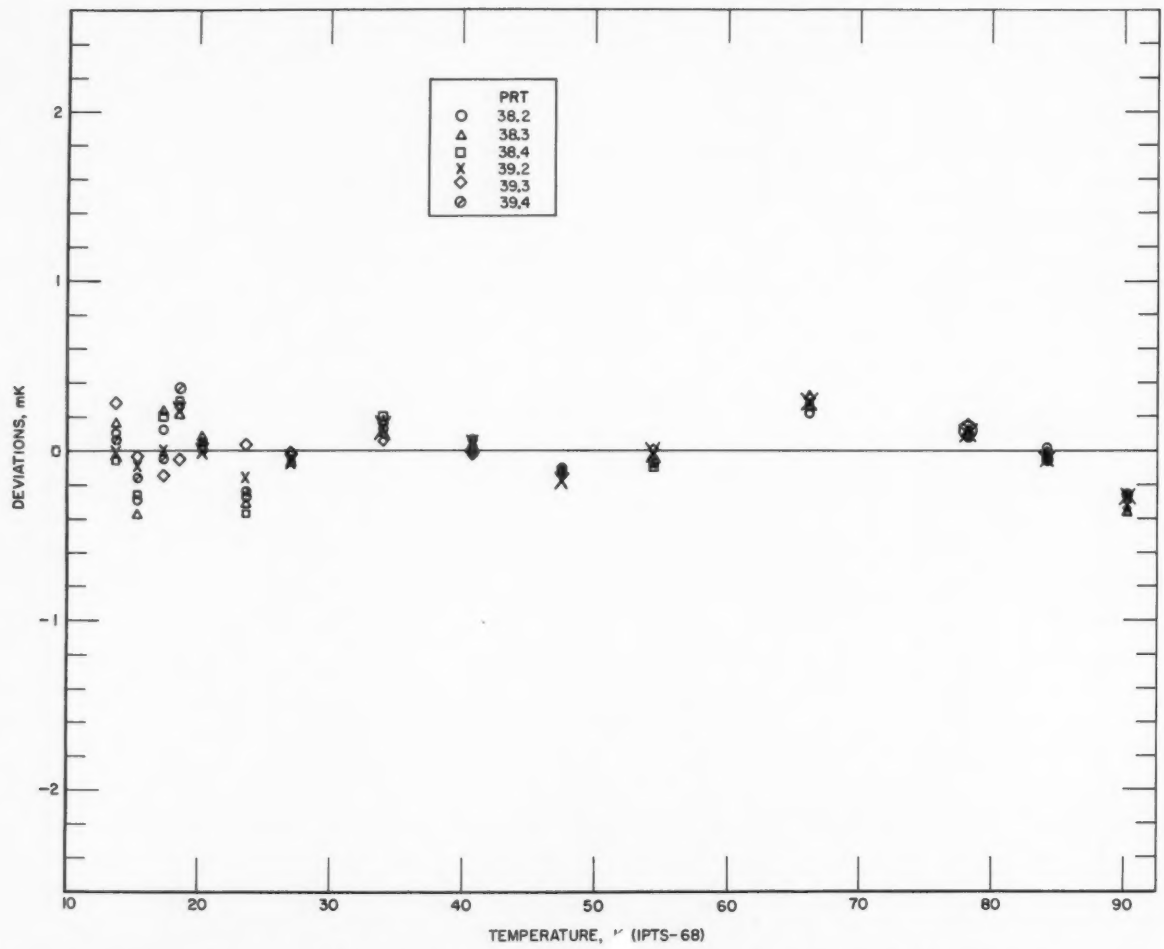


FIGURE 15. *The measured deviations of the values of temperatures, given by the IPTS–68 formulations obtained for each thermometer by the least squares treatment of the calibration data, from those of the NBS–IPTS–68 scale at temperatures of intercomparison with the reference standard.*

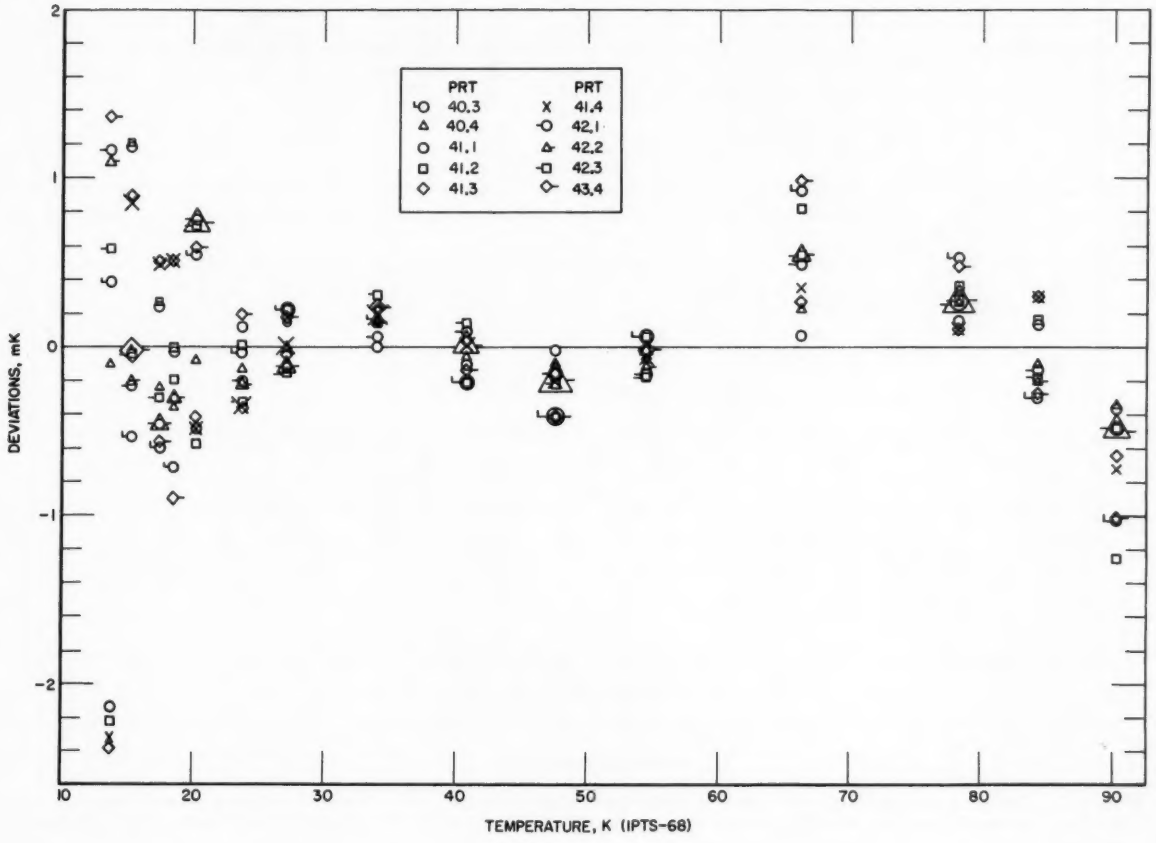


FIGURE 16. *The measured deviations of the values of temperatures, given by the IPTS–68 formulations obtained for each thermometer by the least squares treatment of the calibration data, from those of the NBS–IPTS–68 scale at temperatures of intercomparison with the reference standard.*

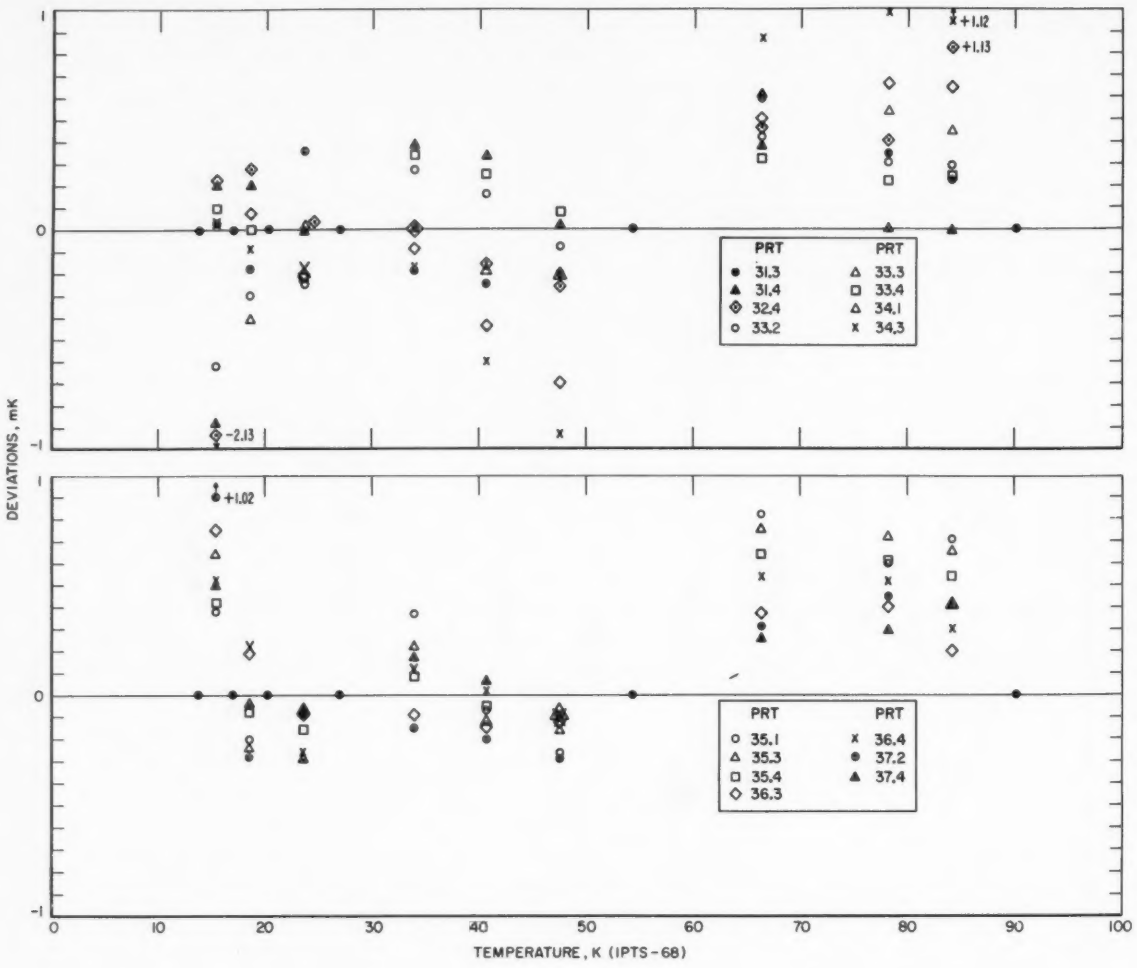


FIGURE 17. *The measured deviations of the values of temperatures, given by the IPTS–68 formulations obtained for each thermometer by the fixed point treatment of the calibration data, from those of the NBS–IPTS–68 scale of temperatures of intercomparison with the reference standard.*

analysis. The deviations are more evenly distributed in the results of the least squares treatment. Except for cases where accidental errors apparently occurred at the fixed point temperatures, the two methods of analyses yielded deviations that are in general very similar in shape. Since the deviations of values of temperatures are very similar for all prt's, particularly above about 40 K, the reference standard prt's employed at the NBS appear not to be "average" prt's. They seem to have characteristics somewhat different from the prt's that were recently calibrated.

The survey of measurements of fixed points employing thermometers calibrated in terms of the NBS–IPTS–68 shows that the values of temperatures reported are in close agreement with the values given in the text of the IPTS–68. The values reported prior to about 1969 are expected to have influenced to some degree the final values for the IPTS–68. Nevertheless, the survey shows that the NBS–IPTS–68 scale closely approximates the defining fixed points of the IPTS–68.

The study of the effect of errors in the calibration data above 0 °C on the calibration of prt's in the region 13 to 90 K indicates that any given error of temperature which causes an error only in the value of $\alpha$ is attenuated by a factor of 10 or more in the calibration between 13 and 90 K when the least squares

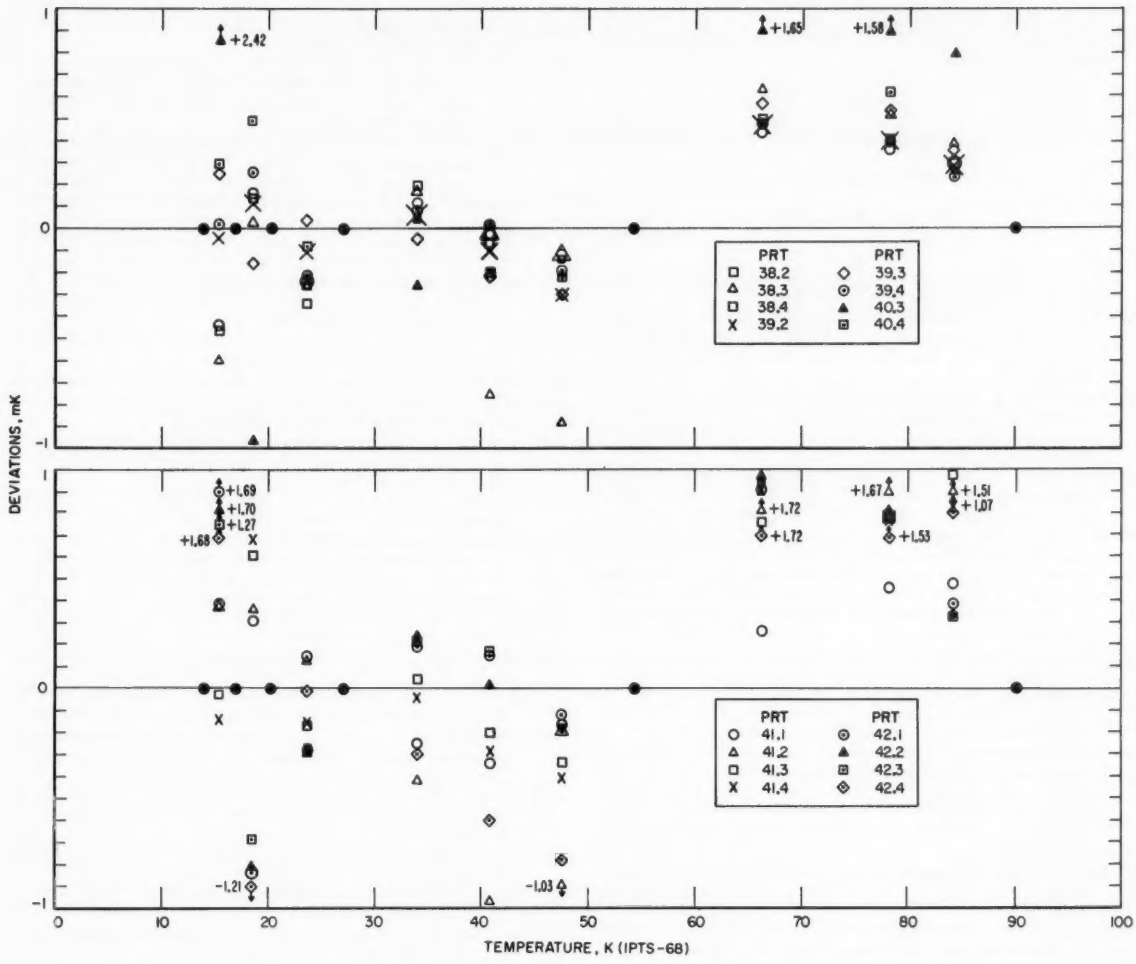


FIGURE 18. *The measured deviations of the values of temperatures, given by the IPTS–68 formulations obtained for each thermometer by the fixed point treatment of the calibration data, from those of the NBS–IPTS–68 scale at temperatures of intercomparison with the reference standard.*

treatment of the data is employed. In the least squares treatment of the data any error in the region 13 to 90 K is distributed both upward and downward in temperature. Since the least squares treatment minimizes the deviations in $W$ and the derivative $dT/dW$ is larger at the lower temperatures, the temperature deviations appear larger at the lower temperatures. To improve the present calibrations, the data at the lower temperatures should be increased in both quantity and accuracy. Work is in progress to make such improvements in the calibrations a practical reality.

---

The authors gratefully acknowledge the help of William J. Hall of NBS Cryogenics Division, Boulder, Colorado, who wrote the present computer program for reducing the prt calibration data for the region 13 to 90 K obtained with the cryostat.

## 7. References


[1] The International Practical Temperature Scale of 1968. Adopted by the Comité International des Poids et Mesures, Metrologia **5**, No. 2, 35–44 (April 1969).

[2] The notations employed in the IPTS–68 document have been abbreviated as follows:

$$T = T_{68}$$

$$W(T) = W(T_{68})$$

$$\Delta W(T) = \Delta W(T_{68})$$

$$W^*(T) = W_{CCT\text{-}68}(T_{68})$$

$$t = t_{68}.$$

The other notations have been retained.

[3] Hoge, H. J., and Brickwedde, F. G., Establishment of a temperature scale for the calibration of thermometers between 14° and 83 °K, J. Res. Nat. Bur. Stand. (U.S.) **22**, 351–373 (1939) RP1188.

[4] Swindells, J. F., National Bureau of Standards provisional scale of 1955, in Precision Measurement and Calibration. Temperature, Nat. Bur. Stand. (U.S.), Spec. Publ. 300, Vol. **2**, 513 pages (August 1968), p. 56.

[5] Moessen, G. W., Aston, J. G., and Ascah, R. G., Thermodynamic temperature scale below 90 °K, the normal boiling point of normal hydrogen, J. Chem. Phys. **22**, 2096–2097 (1954).

[6] Moessen, G. W., Aston, J. G., and Ascah, R. G., The Pennsylvania State University thermodynamic temperature scale below 90 °K and the normal boiling points of oxygen and normal hydrogen on the thermodynamic scale, in American Institute of Physics, Temperature, Its Measurement, and Control in Science and Industry, Vol. **3**, Part 1, 91–102 (Reinhold Publishing Corp., New York, N.Y., 1962).

[7] Borovik-Romanov, A. S., Strelkov, P. G., and Orlova, M. P., Procès-Verbaux dex Séances du Comité International des Poids et Mesures, Tenth Series, **24**, Annexe T18, pp. T141–T147 (Gauthier-Villars, Paris, 1955).

[8] Borovik-Romanov, A. S., Strelkov, P. G., Orlova, M. P., and Astrov, D. N., The I.M.P.R. temperature scale for the 10 to 90 °K region, in American Institute of Physics, Temperature, Its Measurement and Control in Science and Industry, Vol. **3**, Part 1, 113–128 (Reinhold Publishing Company, New York, N.Y., 1962).

[9] Barber, C. R., The establishment of a practical scale of temperature for the range 10–90 °K. Brit. J. Appl. Phys. **13**, 235–241 (1962).

[10] Barber, C. R., Low-temperature scales 10 to 90 °K, in American Institute of Physics, Temperature, Its Measurement and Control in Science and Industry, Vol. **3**, Part 1, 345–350 (Reinhold Publishing Corp., New York, N.Y., 1962).

[11] Orlova, M. P., Sharevskaya, D. I., Astrov, D. N., and Krutikova, I. G., and Barber, C. R., and Hayes, J. G., The derivation of the provisional reference table CCT64, $T = f(W)$ for platinum resistance thermometers for the range from 12 to 273.15 °K. Part 1. The derivation of the table for the range from 12 to 95 °K, Metrologia **2**, No. 1, 6–10 (Jan. 1966).

[12] Bedford, R. E., Durieux, M., Muijlwijk, R., and Barber, C. R., Relationships between the International Practical Temperature Scale of 1968 and the NBS–1955, NPL–61, PRMI–54, and PSU–54 temperature scales in the range from 13.81 to 90.188 K, Metrologia **5**, No. 2, 47–49 (April 1969).

[13] Hoge, H. J., and Arnold, R. D., Vapor pressures of hydrogen, deuterium, and hydrogen deuteride and dew-point pressure of their mixtures, J. Res. Nat. Bur. Stand. (U.S.) **47**, No. 2, 63–74 (Aug. 1951) RP2228.

[14] Barber, C. R., and Horsford, A., The determination of the boiling point and triple points of equilibrium hydrogen and its vapour pressure–temperature relation, Brit. J. Appl. Phys. **14**, 920–923 (1963).

[15] Compton, J. P., The realization of low temperature fixed points, in American Institute of Physics, Temperature, Its Measurement and Control in Science and Industry, Vol. **4**, pending.

[16] Cataland, G., and Plumb, H. H., Comparison of temperature scales and the realization of low temperature fixed points, in American Institute of Physics, Temperature, Its Measurement and Control in Science and Industry, Vol. **4**, pending.

[17] Weber, L. A., Diller, D. E., Roder, H. M., and Goodwin, R. D., The Vapor Pressure of 20 °K Equilibrium Hydrogen, Cryogenics **2**, No. 4, 236–238 (1962).

[18] Grilly, E. R., The vapour pressure of solid and liquid neon, Cryogenics **2**, No. 4, 226–229 (1962).

[19] Furukawa, G. T., Saba, W. G., Sweger, D. M., and Plumb, H. H., Normal boiling point and triple point temperatures of neon, Metrologia **6**, No. 1, 35–37 (Jan. 1970).

[20] Compton, J. P., The realization of the normal boiling point of neon. II. Vapor pressure measurements, Metrologia **6**, No. 3, 103–109 (Aug. 1970).

[21] Muijlwijk, R., Moussa, M. R., and van Dijk, H., The vapour pressure of liquid oxygen, Physica **32**, 805–822 (1966).

[22] Tiggelman, J. L., van Rijn, C., and Durieux, M., Vapor pressures of liquid and solid neon between 19 K and 30 K, in American Institute of Physics, Temperature, Its Measurement and Control in Science and Industry, Vol. **4**, pending.

[23] Moussa, M. R., Muijlwijk, R., and van Dijk, H., The vapor pressure of liquid nitrogen, Physica **32**, 900–912 (1966).

[24] Armstrong, G. T., Vapor Pressure of nitrogen, J. Res. Nat. Bur. Stand. (U.S.) **53**, No. 4, 263–266 (Oct. 1954) RP2543.

[25] Lovejoy, D. R., Some boiling and triple points below 0 °C, Nature **197**, No. 4865, 353–354 (Jan. 1963).

[26] Muijlwijk, R., Durieux, M., and van Dijk, H., Comparisons of platinum resistance thermometers with the hydrogen vapor-pressure thermometer, Physica **43**, 622–632 (1969).

[27] Riddle, J. L., Furukawa, G. T., Plumb, H. H., Platinum resistance thermometry, Nat. Bur. Stand. (U.S.), Monogr. 126, 129 pages (April 1973).

[28] Comité International des Poids et Mesures. Procès-verbaux des séances de l'année 1954, **24**, T96–T121 (1955).

[29] Berry, R. J., The reproducibility of the steam point, Can. J. Phys. **36**, 740–760 (1958).

[30] Bedford, R. E., and Ma, C. K., A note on the reproducibility of the IPTS–68 below 273.15 K, Metrologia **6**, No. 3, 89–94 (July 1970).

[31] Tiggelman, J. L., and Durieux, M., Platinum resistance thermometry between 13.81 K and 373.15 K, in American Institute of Physics, Temperature, Its Measurement and Control in Science and Industry, Vol. 4, pending.

[32] Cetas, T. C., and Swenson, C. A., A paramagnetic salt temperature scale, 0.9 to 18 K, Metrologia **8**, No. 2, 46–64 (April 1972).


(Paper 77A3–770)

JOURNAL OF RESEARCH of the National Bureau of Standards—A. Physics and Chemistry
Vol. 77A, No. 3, May–June 1973

# Radiance Temperature of Niobium at its Melting Point*

**Ared Cezairliyan**

**Institute for Materials Research, National Bureau of Standards, Washington, D.C. 20234**

**(January 29, 1973)**

A subsecond duration pulse heating method is used to investigate variations in the radiance temperature (at 650 nm) of niobium near and at its melting point. Measurements were made on several specimens with different surface conditions. The results do not indicate any dependence of radiance temperature (at the melting point) on initial surface conditions. The average radiance temperature (at 650 nm) at the melting point for twelve different niobium specimens is 2425 K on the International Practical Temperature Scale of 1968, with an average absolute deviation of 0.6 K and a maximum deviation of 1.2 K.

Key words: High-speed measurements; high temperature; melting; niobium; radiance temperature; surface roughness.

## 1. Introduction

In an earlier publication [1],[1] the application of a millisecond resolution pulse heating technique to the measurement of the melting point of niobium was described. In the same publication, preliminary results for the normal spectral emittance (at 650 nm) of two niobium specimens at the melting point were also presented. Normal spectral emittance was obtained from the measurements of the melting point and the radiance temperature at the melting point.

In general, specimen radiance temperature at a given true temperature is not a reproducible quantity. Radiance temperature depends on specimen surface conditions, thus it varies from specimen to specimen (of the same substance) and it may even be different for the same specimen at different times and under different environments.

However, the preliminary results of radiance temperature measurements for the two different specimens reported in the earlier study [1] were within 1.5 K of each other at the melting point of niobium (2750 K). This has suggested the possibility that radiance temperature (at the melting point) may be independent of surface conditions of the solid specimen, thus it may be a reproducible quantity for pure specimens of similar thermal history.

The objective of this paper is to further investigate the melting behavior of niobium and to report the results of recent accurate measurements, utilizing a pulse heating technique, of the radiance temperature of niobium near and at its melting point.

*This work was supported in part by the U.S. Air Force Office of Scientific Research.

[1] Figures in brackets indicate the literature references at the end of this paper.

## 2. General Considerations

Melting of a pure metal is manifested by a plateau in the temperature versus time curve as shown in figure 1 (Case 1). Since in the figure the heating curve is represented by the specimen radiance temperature, validity of the shape of the curve is based on the assumption that the normal spectral emittance of the metal does not change during the solid-to-liquid transition. For real surfaces this assumption is not satisfied, and it is likely that one obtains a heating curve similar to the one shown in figure 1 (Case 2). The drop at the beginning of the plateau corresponds to the change in normal spectral emittance of the metal surface as it melts. An initial high radiance temperature (peak of spike) indicates that normal spectral emittance of the solid surface is higher than that of the liquid surface. This is likely to be the case, in general, since solid surfaces, regardless of the degree of polish, depart from the conditions of ideal smoothness.

## 3. Method

The method is based on resistive self-heating of the specimen from room temperature to its melting point in less than one second and measuring, with millisecond resolution, the pertinent experimental quantities. The specimen's radiance temperature was measured with a high-speed photoelectric pyrometer [2], which permits 1200 evaluations of specimen temperature per second. A schematic diagram showing the arrangement of the specimen and the pyrometer is presented in figure 2. The radiance measurements were performed at 650 nm which corresponds to the effective wavelength of the pyrometer's interference

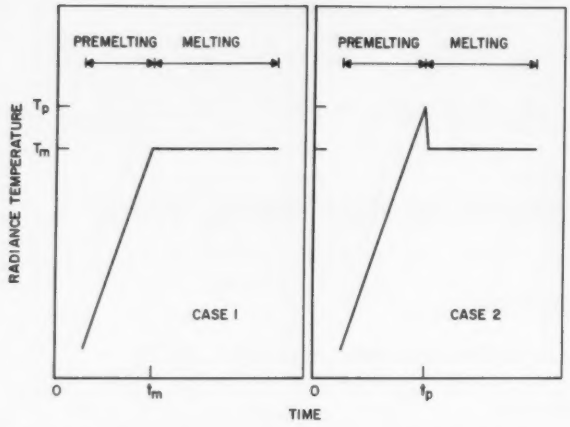


FIGURE 1. *Radiance temperature of pure metals near and at their melting points.*

Case 1 is based on the assumption that normal spectral emittance does not change during the solid-to-liquid transition, and Case 2 is based on the assumption that normal spectral emittance of the solid surface is higher than that of the liquid surface at the melting point.

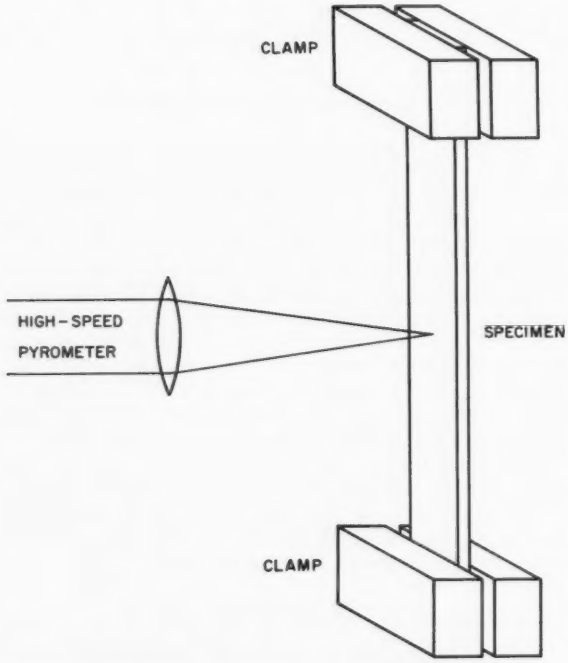


FIGURE 2. *Schematic diagram showing the arrangement of the specimen, clamps, and the pyrometer (dimensions are not to scale).*

filter. The bandwidth of the filter was 10 nm. The circular area viewed by the pyrometer was 0.2 mm in diameter. The recordings of temperature were made with a high-speed digital data acquisition system [3], which is capable of recording data at the rate of 2400 points per second with a full-scale signal resolution of approximately one part in 8000. Details regarding the construction and operational characteristics of the entire measurement system are given in an earlier publication [4].

## 4. Measurements

The niobium specimens were in the form of strips with the following nominal dimensions: length, 75 mm; width, 6.3 mm; and thickness, 0.25 mm. All of the specimens were from the same lot and were 99.9+ percent pure. Manufacturer's analysis indicated the presence of the following impurities in ppm by weight: Ta, 210; Hf and W, < 100 each; Fe, Mo and Zr, < 50 each; Al, Ca, Cr, Co, Cu, Mg, Mn, Ni, Pb, Si, Sn, Ti, V, < 20 each; Cd, < 5; O, 42; N, 25; C, 14; H, 5.

A total of 12 experiments were performed on 12 different specimens. Eight of the experiments were conducted on specimens with surfaces in the "as received" conditions (smooth and shiny). The remaining four experiments were performed on specimens with three different surface roughnesses, which were achieved by using different grades of sand paper. The RMS surface roughness of a typical "as received" specimen was 0.10 $\mu$m, and for the others it ranged from 0.38 to 0.95 $\mu$m, yielding a factor of approximately 10 for the overall variation in surface roughness.

In nine of the experiments the specimens were in a vacuum environment of approximately $10^{-5}$ torr, and in three of the experiments the specimens were in an argon environment at approximately atmospheric pressure.

The specimens were initially annealed by the manufacturer. Ten of the experiments were performed without any additional heat treatment. In two of the cases, the specimens were further annealed in the laboratory before the experiments by subjecting them to 30 heating pulses (up to 2400 K).

Different heating rates, ranging from 1000 K $s^{-1}$ to 20,000 K $s^{-1}$, were used in the experiments. This corresponds to specimen heating periods (from room temperature to the melting point) in the range from 40 ms to 800 ms. The magnitude of current pulses near the melting point was in the range from 200 to 600 A. The high-speed pyrometer was calibrated during the period between experiments 7 and 8 against a tungsten filament standard lamp, which in turn was calibrated against the NBS Temperature Standard.

A summary of the experimental procedure is given in table 1. All measurements reported in this paper are based on the International Practical Temperature Scale of 1968 [5].

## 5. Experimental Results

The radiance temperature of niobium at its melting point for the 12 experiments (corresponding to 12 specimens) and other pertinent results are given in table 1. Oscilloscope trace photographs of specimen radiance as measured with the high-speed pyrometer for two typical experiments representing two specimens having different initial surface conditions ("smooth" and "rough") are shown in figure 3. Com-

TABLE 1. *Summary of experiments for the measurement of radiance temperature of niobium during melting*

| Specimen number [a] | Surface condition [b] | Environment | Premelting Period | | | Melting Period | | | | | Temp. diff. peak and plateau [j] K |
|---|---|---|---|---|---|---|---|---|---|---|---|
| | | | Heating rate K $s^{-1}$ | Stand. dev.[c] K | Rad. temp. at peak [d] K | Number of temp.[e] | Slope at plateau [f] K $s^{-1}$ | Plateau temp. diff.[g] K | Rad. temp.[h] K | Stand. dev.[i] K | |
| 1 | rough–L | vacuum | 2500 | 0.6 | 2444.0 | 37 | −14.7 | −0.4 | 2424.0 | 0.5 | 20.0 |
| 2 | smooth | vacuum | 2900 | .5 | 2429.7 | 90 | 2.4 | .2 | 2424.9 | .4 | 4.8 |
| 3 | smooth | vacuum | 2800 | .5 | 2430.1 | 92 | −3.6 | −.3 | 2425.6 | .5 | 4.5 |
| 4 | rough–M | vacuum | 2800 | .4 | 2456.5 | 31 | −9.3 | −.2 | 2424.5 | .5 | 32.0 |
| 5 | rough–H | vacuum | 2700 | .4 | 2460.3 | 30 | −11.6 | −.3 | 2425.2 | .3 | 35.1 |
| 6 | rough–M | vacuum | 2600 | .5 | 2452.3 | 91 | 9.9 | .7 | 2424.8 | .6 | 27.5 |
| 7 | smooth | vacuum | 1000 | .5 | 2429.9 | 106 | −0.8 | −.1 | 2425.9 | .4 | 4.0 |
| 8 | smooth | vacuum | 3000 | .4 | 2428.9 | 54 | 6.3 | .3 | 2424.2 | .3 | 4.7 |
| 9 | smooth | vacuum | 2300 | .4 | 2429.6 | 95 | −7.0 | −.6 | 2425.2 | .4 | 4.4 |
| 10 | smooth | argon | 2400 | .5 | 2429.7 | 32 | −13.3 | −.4 | 2425.8 | .5 | 3.9 |
| 11 | smooth | argon | 11400 | .6 | 2423.7 | 20 | −7.6 | −.1 | 2423.7 | .5 | 0 |
| 12 | smooth | argon | 20700 | .6 | 2424.9 | 12 | 10.3 | .1 | 2424.9 | 1.4 | 0 |

[a] Also represents the experiments in chronological order.

[b] The notations used for surface conditions correspond to the following typical roughnesses in $\mu$m: smooth, 0.10; rough–L, 0.38; rough–M, 0.53; rough–H, 0.95.

[c] Represents standard deviation of an individual temperature as computed from the difference between the measured value and that from the smooth temperature versus time function (quadratic) obtained by the least squares method. Data extends approximately 100 K below the melting point.

[d] Maximum radiance temperature that corresponds to the peak of the spike in temperature observed just before melting of specimen.

[e] Number of temperatures used in averaging the results at the plateau to obtain an average value for the radiance temperature at the melting point of the specimen.

[f] Derivative of the temperature versus time function obtained by fitting the temperature data at the plateau to a linear function in time using the least squares method.

[g] Maximum radiance temperature difference between the beginning and the end of the plateau based on the linear temperature versus time function.

[h] The average (for a specimen) of measured radiance temperatures at the plateau.

[i] Standard deviation of an individual temperature as computed from the difference between the measured value and that from the average plateau radiance temperature.

[j] Difference between peak and average plateau radiance temperatures.

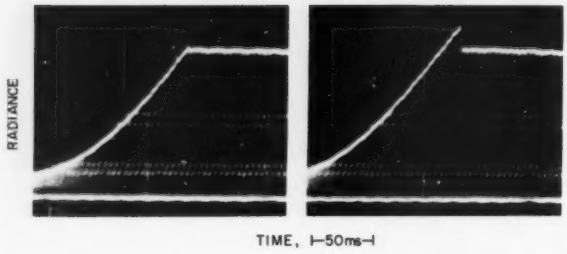


FIGURE 3. *Oscilloscope trace photograph of specimen radiance near and at its melting point as measured with the high-speed pyrometer.*

Photograph on the left is for specimen-2 having a "smooth" surface. Photograph on the right is for specimen-5 having a "rough" surface. Radiance is in arbitrary units.

parison of the traces in figures 1 and 3 verifies the assumptions made regarding the shape of the traces in figure 1. Figure 4 shows the variation of radiance temperature as a function of time near and at the melting point for five typical experiments. These experiments were selected to represent different specimen surface and operational conditions. All the curves, with the exception of "A", show spikes of varying magnitude. The specimen heating rate in experiments corresponding to curves "B", "C", "D", and "E" were four times slower than that of "A". Thus, the lack of a spike in curve "A" may be attributed to the inability of the system to detect it. It is interesting to observe that, regardless of the initial surface and operational conditions, radiance temperature at the melting plateau is approximately the same for all the specimens.

The radiance temperatures at the peak of the spike as well as at the plateau for the 12 specimens are shown in figure 5. It may be seen that the two fast experiments do not show any peak for reasons discussed above. For the same "smooth" surface conditions, the results of six experiments give approximately the same value (within 1 K) for the peak temperature, which is 4.4 K higher than the plateau temperature. Further changes in the heating rate (slowing down) did not affect the results. The experiments on specimens with initially rough surfaces yielded high peak temperatures; however, the plateau temperatures were in good agreement (within 1 K) with those of other specimens. The greatest difference between peak and plateau temperatures, corresponding to the specimen with the roughest surface, is 35 K.

A single value for the radiance temperature at the plateau for each specimen was obtained by averaging the temperatures at the plateau. The number of temperatures used for averaging ranged from 12 to 106 depending on the speed of the experiment and the behavior of the specimen during melting. The standard deviation of an individual temperature from the average was in the range from 0.3 to 0.6 K, with the exception of the very fast experiment which yielded 1.4 K. The details of the results for each experiment are given in table 1. To determine the trend of measured temperatures at the plateau, temperatures for each experiment

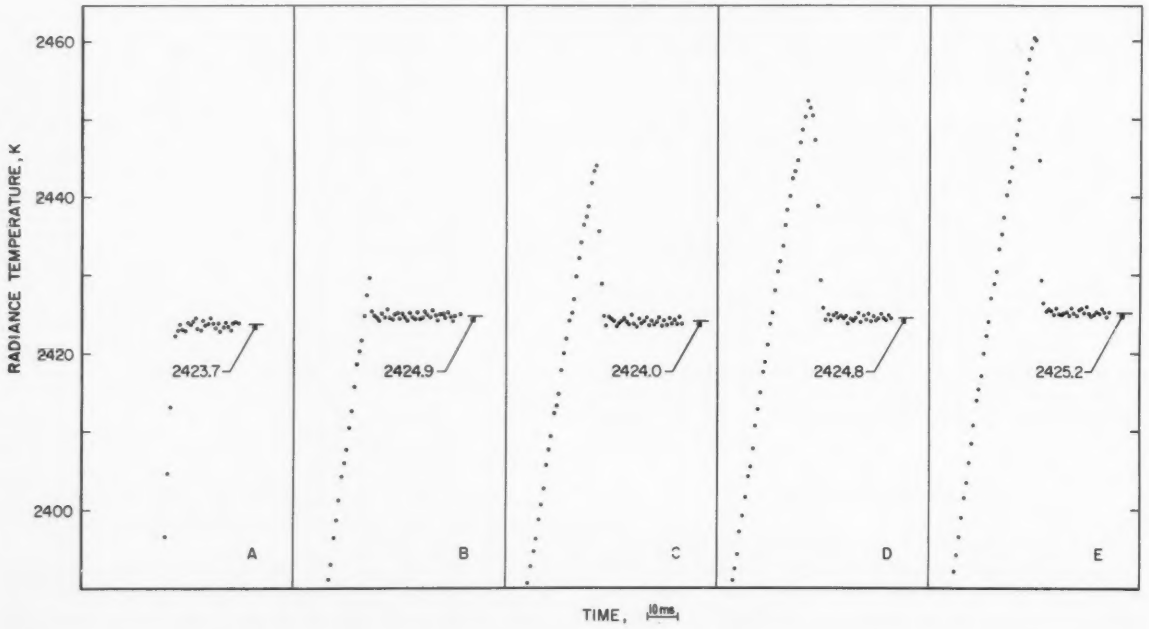


FIGURE 4. *Variation of radiance temperature (at 650 nm) of niobium as a function of time near and at its melting point for five typical experiments.*

Time interval between consecutive temperature points in 0.833 ms. Correspondence between curve codes and experiment numbers are as follows: A, 11; B, 2; C, 1; D, 6; E, 5.

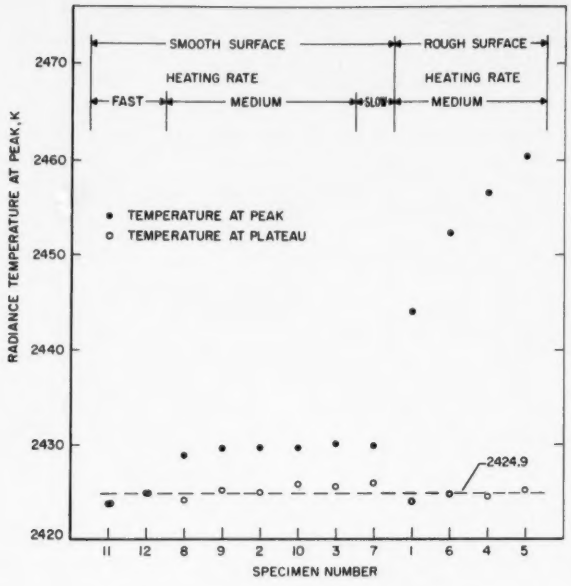


FIGURE 5. *Radiance temperature (at 650 nm) at the peak and at the plateau for the niobium specimens.*

The single value for the plateau of each specimen corresponds to the average over the entire plateau for that specimen.

were fitted to a linear function in time using the least squares method. The slopes of the linear functions (table 1) do not show any significant bias with respect to direction. The maximum temperature difference between the beginning and the end of the plateau (corresponding to the slope in the plateau) was in the range from 0.1 to 0.7 K. The standard deviation of an individual temperature from the linear function was the same as the standard deviation obtained by direct averaging of the temperatures.

The measured radiance temperatures at the plateau are shown in figure 6 for two specimens having "smooth" surfaces representing two different heating rates (table 1). The plateaus do not show any anomalies and are horizontal from the beginning to the end. However, the results are somewhat different in the case of specimens having initially rough surfaces (fig. 7). Temperature instabilities are observed during the initial melting period, which subside during the second half yielding a horizontal plateau. The temperatures in the anomalous region are approximately 1 to 3 K above those at the stable plateau.

The average radiance temperature at the melting point for the twelve specimens was 2424.9 K, with an average absolute difference of 0.6 K and a maximum difference of 1.2 K. The results are presented in figure 8. It may be concluded that the radiance temperature (at 650 nm) of niobium at its melting point is 2425 K.

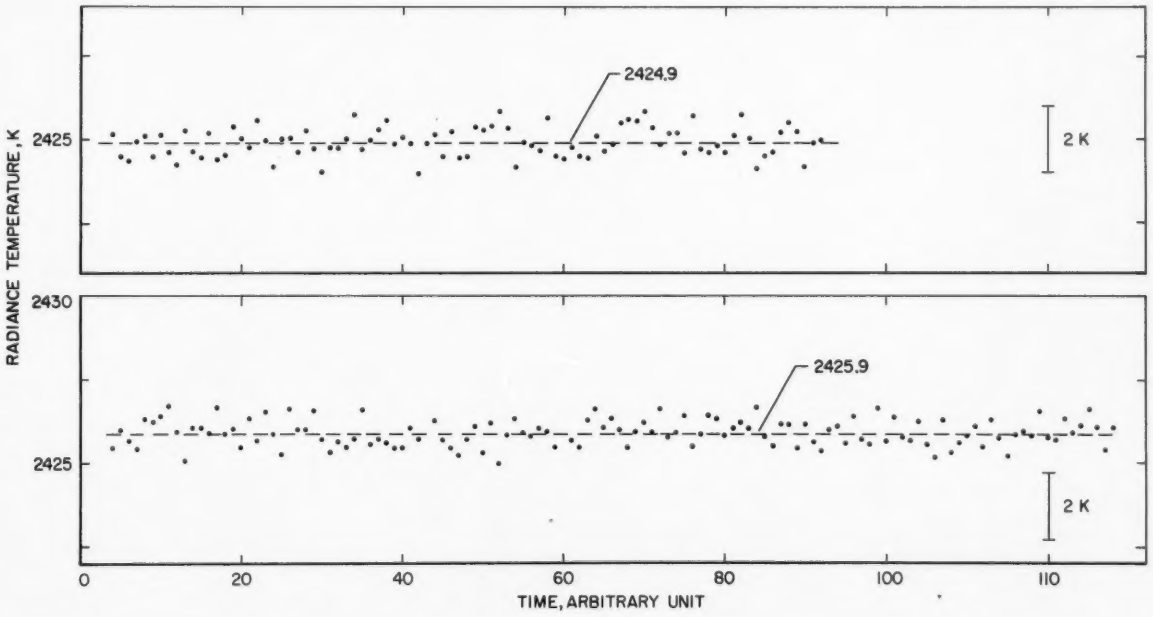


FIGURE 6. *Radiance temperature (at 650 nm) of niobium (with initially "smooth" surface) at its melting point.*

Upper trace is for specimen-2, and lower trace is for specimen-7. One time unit is 0.833 ms.

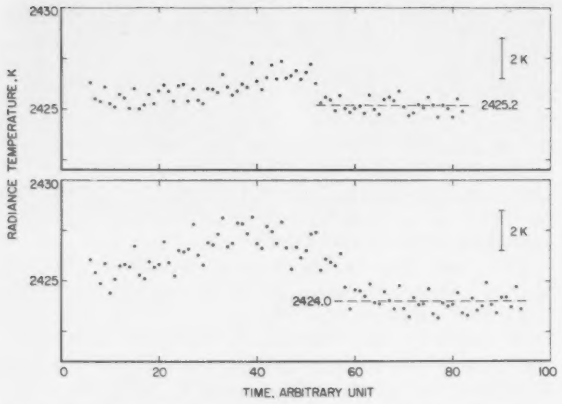


FIGURE 7. *Radiance temperature (at 650 nm) of niobium (with initially "rough" surface) at its melting point.*

Upper trace is for specimen-5, and lower trace is for specimen-1. One time unit is 0.833 ms.

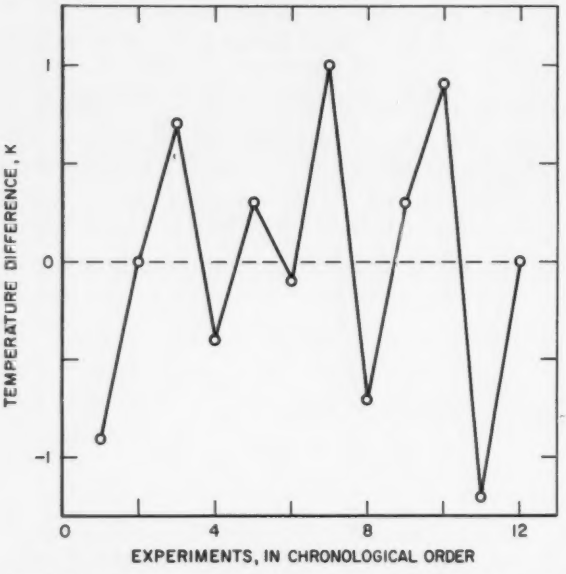


FIGURE 8. *Difference of radiance temperature (at the melting point of niobium, at 650 nm) for individual experiments from their average value of 2424.9 K (represented by the "zero" line).*

## 6. Estimate of Errors

The details of sources and estimates of errors in high-speed experiments similar to those conducted in this study are given in an earlier publication [3]. Specific items in the error analysis were recomputed whenever the present conditions differed from those in the earlier study. The imprecision [2] of temperature measurements, during heating as well as melting periods, is approximately 0.5 K (table 1). Inaccuracy [3] of temperature measurements near and at the melting point of niobium is estimated to be not more than 7 K. The major single source contributing to this inaccuracy is the uncertainty in the calibration of the tungsten filament standard lamp (approximately 3 K at 2400 K). The melting point depression due to the impurities in the specimens is estimated to be not more than 2 K. It may be concluded that the inaccuracy of the measured radiance temperature of niobium at its melting point is not more than 10 K.

It may be seen from table 1 that the imprecision of temperature measurements during heating of the specimen (before reaching the melting point) was approximately the same as that during the melting period. This indicates that in the experiment the initial melting phase progressed normally and that there were no undesirable effects during melting of the specimen, such as vibration of the specimen, instantaneous development of hot spots in the specimen, and random changes in the specimen surface conditions.

## 7. Discussion

The results of this study show that radiance temperature at the melting point of niobium is reproducible and is independent of: (a) the initial surface conditions of the specimen, (b) the environment (vacuum or argon) in which the specimen is heated, and (c) the heating rate of the specimen.

The 12 experiments performed under different conditions yielded an average value of 2424.9 K for the radiance temperature, with an average absolute difference of 0.6 K and a maximum difference of 1.2 K. The preliminary results on two niobium specimens reported in an earlier publication [1] had yielded an average value of 2423.3 K, which is only 1.6 K below the present value.

Considering 2750 K for the melting point of niobium [1] and 2425 K for the radiance temperature at the melting point, a value of 0.340 is obtained for the normal spectral emittance (at 650 nm) at the melting point of niobium. Earlier measurement, utilizing the same pulse heating system, on tubular niobium specimens in the range 1700 to 2300 K showed a linear variation of normal spectral emittance with temperature [6]. Extrapolation of these results to the melting point yields 0.348 for normal spectral emittance, which is approximately 2 percent higher than the present value. Measurement of normal spectral emittance of niobium near its melting point is reported in the literature to be 0.362 [7]; this is approximately 6 percent higher than the present value. In the case of solid surfaces, departure, in varying degrees, from ideal surface conditions may have been partially responsible for the high values.

This may be demonstrated by considering the present results on "rough" specimens. From table 1 (last column) it may be seen that for the "rough" specimens a considerable difference exists between

[2] Imprecision refers to the standard deviation of an individual temperature as computed from the difference between the measured value and that from the smooth function obtained by the least squares method.

[3] Inaccuracy refers to the estimated total error (random and systematic).

the peak and plateau temperatures. This difference in temperature corresponds to a difference in normal spectral emittance ranging from 7 to 14 percent for the four "rough" specimens. In the case of the "smooth" specimens, corresponding average difference in emittance is approximately 2 percent. The above substantiate, both in magnitude and in direction, the difference between present results and those reported in the literature.

The radiance temperature (at 645 nm) of liquid niobium at its melting point was measured recently using a levitation calorimeter [8]. The reported result of 2405 K is 20 K lower than the present value. No satisfactory explanation has been found for this discrepancy.

It may be noted that, with the present system, it was not possible to follow the entire melting process because the specimen collapsed and opened the main electrical circuit prior to the completion of melting.

In conclusion, the results of this study have shown the constancy and reproducibility of the radiance temperature of niobium at its melting point. Compared to the difficulties encountered in the construction and operation of blackbody cavities at temperatures above 2000 K, the scheme of measuring radiance temperature at the melting point of selected substances may be an easier, more accurate, and in addition more practical approach for performing secondary calibration on instruments and for conducting overall on-the-spot checks on complicated measurement systems at high temperatures. This suggests the extension of investigations, similar to those reported in this paper, to other refractory metals at temperatures above 2500 K.

The author expresses his gratitude to C. W. Beckett for his continued interest and encouragement of research in high-speed measurement methods. The contribution of M. S. Morse in connection with electronic instrumentation is also greatly appreciated.

## 8. References

[1] Cezairliyan, A., Measurement of melting point, normal spectral emittance (at melting point), and electrical resistivity (above 2650 K) of niobium by a pulse heating method, High Temperatures-High Pressures, **4**, 453 (1972).

[2] Foley, G. M., High-speed optical pyrometer, Rev. Sci. Instr. **41**, 827 (1970).

[3] Cezairliyan, A., Morse, M. S., Berman, H. A., and Beckett, C. W., High-speed (subsecond) measurement of heat capacity, electrical resistivity, and thermal radiation properties of molybdenum in the range 1900 to 2800 K, J. Res. Nat. Bur. Stand. (U.S.), **74A** (Phys. and Chem.), No. 1, 65–92 (Jan.–Feb. 1970).

[4] Cezairliyan, A., Design and operational characteristics of a high-speed (millisecond) system for the measurement of thermophysical properties at high temperatures. J. Res. Nat. Bur. Stand. (U.S.), **75C** (Eng. and Instr.), No. 1, 7 (1971).

[5] International Practical Temperature Scale of 1968, Metrologia, **5**, 35 (1969).

[6] Cezairliyan, A., High-speed (subsecond) measurement of heat capacity, electrical resistivity, and thermal radiation properties of niobium in the range 1500 to 2700 K, J. Res. Nat. Bur. Stand. (U.S.), **75A** (Phys. and Chem.), No. 6, 565–571 (Nov.–Dec. 1971).

[7] Pemsler, J. P., Thermodynamics of interaction of niobium and tantalum with oxygen and nitrogen at temperatures near the melting point, J. Electrochem. Soc. **108**, 744 (1961).

[8] Bonnell, D. W., Treverton, J. A., Valerga, A. J., and Margrave, J. L., The emissivities of liquid metals at their fusion temperatures, Proceedings of the Fifth Symposium on Temperature, in press.

(Paper 77A3–771)

JOURNAL OF RESEARCH of the National Bureau of Standards—A. Physics and Chemistry
Vol. 77A, No. 3, May–June 1973

# An Experimental Search for Gaseous Reactivity Between $AlF_3$ and HF Near 1200 K*

**Thomas B. Douglas and Ralph F. Krause, Jr.**

**Institute for Materials Research, National Bureau of Standards, Washington, D.C. 20234**

**(December 13, 1972)**

Using an accurate transpiration method, $AlF_3$ was sublimed near 1200 K into argon containing 0, 0.02, and 0.76 atm of HF, but no reaction between $AlF_3$ and the HF was detected within the precision (about 1%). Two alternative structures of $HAlF_4$ are postulated. An upper bound for extent of reaction corresponds to $\Delta H^\circ_{298} > -33$ kcal ($-138$ kJ) for $AlF_3$ (g) + HF (g) = $HAlF_4$ (g); this indicates a far lower stability of $HAlF_4$ (g) than that of $LiAlF_4$ (g) or $NaAlF_4$ (g) when formed similarly.

Key words: Aluminum fluoride; aluminum hydrofluorides; equilibrium constant; hydrogen fluoride; stability limits; transpiration measurements.

## 1. Introduction

The transpiration technique affords precise measurement of not only vapor pressures but also gaseous equilibria, since the vaporization equilibria themselves are fixed. Hence, when a new gas is added to the inert carrier gas, any enhancement of vaporization may ordinarily be attributed to chemical reaction between the extra vapor and the new gas. From earlier such studies at temperatures near 1200 K we determined the vapor pressures of crystalline $AlF_3$ [1][1] and the heats of formation of the gases $AlF_2Cl$ and $AlFCl_2$ [2]. In the present study, in the same temperature range, $AlF_3$ was sublimed in the presence of HF in search of measurable formation of hydrofluorides of aluminum. Mass spectrometric studies [3] have shown that under the same conditions Li or Na in place of H would lead to almost complete reaction. As high-temperature gas species, some *hydroxides* of metals are known to be of considerable importance, though apparently no gaseous metallic hydrofluorides have been reported. No reactivity between $AlF_3$ and HF was detectable in the present study within experimental error, and the implications deduced regarding the stability of $HAlF_4$ (g), presumably the most likely product, are discussed.

## 2. Experimental Procedure and Results

$AlF_3$ was allowed to sublime into flowing pure argon or argon containing a known proportion of HF, the volume of argon and mass of sublimed $AlF_3$ being subsequently determined. The apparatus, high-purity $AlF_3$ and carrier-gas argon, procedure, and precautions were (when applicable) as described earlier [1, 2]. The vessels attached to the original apparatus to handle the HF were of monel, whose surface was conditioned by preliminary flushes of HF. Commercial anhydrous liquid HF, claimed to be 99.9 mol percent pure, was distilled into place, and served to create the desired partial pressure of this gas by bubbling argon at 1 atm through it at either the Dry-Ice or ice temperature. The partial pressures of HF were subsequently determined by absorption in "activated" NaF and weighing. The argon itself had been dried by commercial molecular sieves (claimed residue, 1.5 ppm by volume).

The significant data obtained are given (one run per line) in table 1. In the last column the apparent vapor pressure of $AlF_3$ calculated for each run is compared with that of the smoothed value at the same exact temperature from the earlier work [1], in which $AlF_3$ was sublimed into pure argon. (At these temperatures and pressures HF vapor is nearly all monomer, and it was convenient to count each mole of $Al_2F_6$ as two moles of $AlF_3$.)

The deviations (last column of the table) should be nearly independent of the systematic error (possibly as high as 1%) of the earlier measurements [1] (eight runs from 1194 to 1258 K; standard deviation, 0.15%; flow rates, 1–2 ml/s). The deviations at 1200 K when HF was present are zero within their limited precision, and require no further consideration since the results at 1260 K involve a partial pressure of HF 40 times as great and hence form a much more sensi-

*This work was supported at the National Bureau of Standards by the U.S. Air Force Office of Scientific Research under Agreement Nos. AFOSR–ISSA–68–0004 and –71–0003.

[1] Figures in brackets indicate the literature references at the end of this paper.



496-895 OL - 73 - 3

TABLE 1. *Experimental data*

| Approx. temp., K | Gas flow over $AlF_3$, ml/s | $P_{HF}$, atm | $AlF_3$ enhancement in vapor, %[a] |
|---|---|---|---|
| 1200 | 2.6 | 0 | +0.3 |
| | 2.7 | 0.02 | +0.8 |
| | 2.7 | 0.02 | −0.5 |
| 1260 | 2.3 | 0 | −0.2 |
| | 6.0 | 0 | −1.1 |
| | 6.3 | 0 | −1.0 |
| | 7.2 | 0.76 | −1.3 |
| | 7.4 | 0.76 | −1.2 |

[a] The vapor pressure of $AlF_3$ varies from approximately 0.002 atm at 1200 K to 0.007 atm at 1260 K.

tive test of reaction between $AlF_3$ and HF. There is no reason to believe that HF would appreciably *raise* the effective activity coefficient of $AlF_3(g)$ under these conditions; hence the distinctly negative trend of the deviations at 1260 K for the higher flow rates must be considered to reflect appreciable deviations from vaporization equilibrium (lower flow rates were not feasible when so much of the carrier gas was HF). An attempt to correct empirically for the supposed lack of saturation of the $AlF_3$ vapor gives, for the proportion of the $AlF_3(g)$ reacting with HF in the last two runs, no value different from zero with certainty. However, one type of extrapolation gave us 1 percent; we arbitrarily double this,[2] and conclude that less than 2 percent of the $AlF_3(g)$ reacted with HF under these conditions. This corresponds to a limiting Gibbs-energy value of $\Delta G^\circ_{1260} > 9$ kcal (38 kJ) for the reaction

$$AlF_3(g) + HF(g) = HAlF_4(g). \qquad (1)$$

In contrast, appropriate thermal functions [3] indicate that the same reaction except with Li or Na replacing H proceeds to more than 99.999 percent completion under the same initial conditions.

## 3. Discussion

An estimate of the molecular constants of $HAlF_4$ allows calculation of a free energy function and a corresponding bound on the heat of reaction (1). Two alternative structures were assumed, as follows. *Structure I:* Tetrahedral $AlF_4$ (Al-F, 1.69 Å), with a linear H-F-Al group (H-F, 1.0 Å). (Similar structures had been assumed for $LiAlF_4$ and $NaAlF_4$ [3].) Vibrational fundamentals, the same as those of $AlF_3$ and HF [3], plus (in $cm^{-1}$ and with degeneracies in parentheses) 500(1), 300(2), and 800(2). *Structure II:* Planar. Unaltered $AlF_3$ [3] attached to HF (H-F, 1.0 Å) through a hydrogen bond 1.5 Å long. Vibrational fundamentals, same as for Structure I except with 500(1) replaced by 200(1). These two structures give for $-(G^\circ_{1260} - H^\circ_{298})/1260$ respectively 90.4 and 94.0 cal $mol^{-1}K^{-1}$ (378 and 393 J $mol^{-1}K^{-1}$), and for reaction (1) (with $\Delta G^\circ_{1260} > 9$ kcal) values of $\Delta H^\circ_{298} > -33$ and $> -29$ kcal ($> -138$ and $> -121$ kJ). When H in reaction (1) is replaced by Li or Na, the respective values of $\Delta H^\circ_{298}$ are $-73$ and $-88$ kcal ($-305$ and $-368$ kJ) [3].

One may seek the principal reason why $\Delta H$ for reaction (1) is so much greater than for the Li or Na analog. Considering Structure I for $HAlF_4$, perhaps the large difference can be traced principally to the far greater energy of decomposition to ions for HF than for LiF or NaF. On the other hand, Structure II would make reaction (1) simply the formation of a hydrogen bond. The hydrogen-bond energy in $HF_2^-(g)$ has been evaluated as lying between 37 and 63 kcal $mol^{-1}$ (155 and 264 kJ $mol^{-1}$) by several semi-experimental and theoretical methods, but in other species it is very generally much lower, typically being approximately 6 kcal $mol^{-1}$ (25 kJ $mol^{-1}$) in the gaseous polymers of HF [4].

The present study has shown that gaseous reaction products between $AlF_3$ and HF are not important species near 1200 K (except possibly under high pressures of HF). Assuming their formation to be somewhat exothermic, they would be even less important at higher temperatures and the same pressures, and also at lower temperatures because of the much smaller vapor pressures of $AlF_3$. The transpiration technique, despite its high precision for overall results, is less promising than spectroscopic techniques for detecting and measuring such distinctly minor species.

---

Discussions with Charles W. Beckett and Stanley Abramowitz were very helpful in estimating fundamental frequencies for $HAlF_4$.

## 4. References

[1] Krause, R. F., Jr., and Douglas, T. B., J. Phys. Chem. **72**, 475 (1968).
[2] Krause, R. F., Jr., and Douglas, T. B., *ibid.*, **72**, 3444 (1968).
[3] JANAF Thermochemical Tables, 2nd ed. Nat. Stand. Ref. Data Ser., Nat. Bur. Stand. (U.S.), 37, 1141 pages (June 1971).
[4] Pauling, L., The Nature of the Chemical Bond, 3d ed. (Cornell Univ. Press, Ithaca, N.Y., 1960), p. 460.

(Paper 77A3–772)

[2] This factor of 2 makes only minor differences in the rough limiting values for $HAlF_4$ deduced later in this paper.

JOURNAL OF RESEARCH of the National Bureau of Standards—A. Physics and Chemistry
Vol. 77A, No. 3, May–June 1973

# A Numerical Solution of the Integral Equation Describing a Photometric Integrating Sphere

**Robert L. Brown**

**Institute for Materials Research, National Bureau of Standards, Washington, D.C. 20234**

**(January 10, 1973)**

A photometric integrating sphere containing a single disk-shaped baffle and a point source with an arbitrary angular intensity distribution is described by an integral equation. Numerical solutions of this equation are presented for several different source distributions. The errors involved in comparing the various sources are evaluated as a function of baffle size and position.

Key words: Integrating sphere; photometry.

## 1. Introduction

The integrating sphere is used in photometry to measure total luminous flux. In a sphere with a diffusely reflecting coating, the illuminance by reflected light is approximately the same at all points on the sphere surface and is proportional to the total flux emitted by the lamp. This reflected light is measured at a point on the sphere surface which is shielded from the direct rays of the lamp by a baffle. Its intensity depends somewhat on the geometry and reflectance of the objects inside the sphere and on the angular intensity distribution of the light from the lamp. Unless this dependence is known, errors will occur in measuring the luminous flux from different types of lamps.

It is possible to describe the nonempty integrating sphere by an integral equation [1],[1] whose solution gives the illuminance by reflected light at every point on all the surfaces inside the sphere. The present paper describes a numerical solution of this equation for a sphere containing a point source with an arbitrary angular intensity distribution and a disk-shaped baffle located perpendicular to the polar axis of the sphere. The existence of an $\infty$-fold axis of symmetry simplified the work considerably by making it possible to do the azimuthal integrations analytically. The illuminance of the surface inside the sphere was calculated for several values of the baffle radius and its position along the polar axis. Although hemispherical source distributions were used for most of the calculations, the results are applicable to any small lamp whose intensity distribution is known. The extension of the technique to larger sources, like fluorescent lamps, should not be difficult. For convenience, uniform reflectance was assumed for all surfaces. The model, however, requires only that the reflection coefficient have axial symmetry about the polar axis. No consideration was given here to the effects of nondiffuse reflection.

[1] Figures in brackets indicate the literature references on page.

## 2. Theory

### 2.1. General Integral Equation

Let $da$ be an area element of the baffle or inside sphere surface about a point labeled $a$, and let $da'$ be another element of area about a point $a'$. Let $\mathbf{x}$ be the vector directed from $a'$ to $a$, and let $\mathbf{n}'$ and $\mathbf{n}$ be the respective unit outward normals to $da'$ and $da$. Let $E(a)$ represent the illuminance at point $a$ by reflected light only, and let $E_0(a)$ be the illuminance caused by direct light from the source. This latter quantity is determined by the overall geometry and angular intensity distribution of the source. All surfaces are assumed to be perfect diffuse reflectors. Let $\rho(a)$ be the total reflectance at point $a$. The flux $dF(a, a')$ coming from $da'$ to $da$ is given by the expression

$$dF(a,a')=\rho(a')\,[E_0(a')+E(a')]\,da'\,(-\mathbf{x}\cdot\mathbf{n}')\,da\,(\mathbf{x}\cdot\mathbf{n})\times S(a,a')/(\pi x^4). \qquad (1)$$

A derivation of this equation is given by Jacquez and Kuppenheim [2]. In the present work a factor $S(a, a')$ has been introduced to account for the screening of one part of the sphere's surface from another by the baffle. If all points on $da'$ can be seen from $a$, then $S(a, a')=1$. If $da'$ is completely or partially screened

from $a$ by the baffle, then $S(a, a')$ will be zero or some number less than unity. The illuminance $E(a)$ of $da$ by reflected light is then equal to the integral of the quantity $dF(a, a')/da$ over all the area elements $da'$ on the inside of the sphere. This, of course, includes the baffle surface as well as the sphere surface. The unknown quantity $E(a)$ is thus expressed as an integral containing itself and quantities which are known. We have then,

$$E(a) = \int_{a'} \rho(a')[E_0(a') + E(a')]T(a, a')S(a, a')da'/\pi \qquad (2)$$

where

$$T(a, a') \equiv (-\mathbf{x} \cdot \mathbf{n}')(\mathbf{x} \cdot \mathbf{n})/x^4. \qquad (3)$$

The numerical solution of (2) can be obtained by first dividing the surfaces involved into a number of small area elements $\delta a'$ having roughly the same size, and approximating the integral by a sum over these $\delta a'$. Values of the functions $S(a, a')$ and $T(a, a')$ for all possible pairs of area elements are fixed by the geometry of the system, while $\rho(a)$ and $E_0(a)$ are assumed to be specified. One then guesses a solution for $E(a)$, say $E^0(a)$, and uses (2) to get a first approximation $E^1(a)$. The process is repeated using this first approximation in (2). Repetition of this procedure gives a sequence of functions $E^i(a)$ which may converge. If it does, the accuracy of the solution may be checked by repeating the whole calculation with smaller area elements $\delta a'$, or with a better approximation to the integral, to see whether the limiting value of the function $E(a)$ changes significantly. The former method was used in the present work.

Equation (2) is quite general except for the restriction that the surfaces be diffuse reflectors. In practice, the difficulties involved in evaluating $S(a, a')$ and $T(a, a')$ make it desirable to keep the geometry as simple as possible. This will also reduce the number of terms needed in the representation of (2) as a sum, thereby saving time on the iterative calculations. In particular, the use of an experimental arrangement having an $\infty$-fold ($C_\infty$) axis of symmetry greatly simplifies all aspects of the analysis. Furthermore, this symmetry restriction does not impose any symmetry requirements on the angular intensity distribution of the source. It need be applied only to the geometry and reflectance of the surfaces in the sphere.

### 2.2. Specific Model Used in the Calculation

#### a. Classification of Surfaces

The sphere geometry in the present calculation was chosen to approximate the substitution method of using the sphere. Positions of the various surface elements were specified in spherical coordinates with the origin at the sphere center. This model had the following characteristics:

(a) A point source at the center of the sphere of radius $R$, with no restrictions on its angular intensity distribution.

(b) A flat, infinitely thin, circular baffle of radius $B$ with its center on the polar axis a distance $D$ from the sphere center and oriented normal to the polar axis.

(c) Uniform reflectance for sphere and baffle surfaces.

For this model, the solution of (2) requires the evaluation of five integrals. Let the symbol $s$ designate points on the sphere, $a_N$ points on the north side of the baffle, and $a_S$ points on the south side. Let $dE = dE(a, a')$ be the illuminance at point $a$ produced by the area element $da'$ around $a'$. Equation (2) then takes the form

$$E(s) = \int_{s'} dE(s, s') + \int_{a_{N'}} dE(s, a_{N'}) + \int_{a_{S'}} dE(s, a_{S'})$$

$$E(a_N) = \int_{s'} dE(a_N, s')$$

$$E(a_S) = \int_{s'} dE(a_S, s'). \qquad (4)$$

Numerical integration of (4) is necessary only for the polar angle $\theta$ since the integration over the azimuthal angle $\varphi$ can be done analytically. Throughout the discussion, points on the sphere surface will be specified by the coordinates $\theta$ and $\varphi$ written without subscripts. The radial coordinate $r$ is a constant equal to $R$ for these points. Baffle points will be designated by the subscript $B$ on the spherical coordinates. The radial coordinate $r_B$ is related to $\theta_B$ by the equation

$$r_B = D \cos \theta_B. \qquad (5)$$

#### b. Separation of the Azimuthal and Polar Integrations

When both $a$ and $a'$ are on the sphere, $T(a, a')$ is a constant. If one of the points is on the baffle, the determination of $S(a, a')$ is trivial. To carry out the integration involving the azimuthal variable it is therefore only necessary to calculate the azimuthal dependence of $S(a, a')$ when both points are on the sphere, and that of $T(a, a')$ when one point is on the baffle. These calculations are outlined in appendices I and II. Following this, $E_0(a)$ for the different surfaces must be calculated in terms of the angular intensity distribution of the source. This is done in appendix III. For convenience, it will be assumed that the source intensity distribution is independent of the azimuthal angle $\varphi$. This means that $E(a)$ will also be independent of $\varphi$. It is important to note, however, that the value of $E(a)$ at a pole of the sphere depends only on the values of $E_0(a)$ averaged over $\varphi$, provided the reflection coefficient has $C_\infty$ symmetry. If the observation point is at a pole there are no restrictions on the azimuthal variations in the source intensity. This point will be discussed in appendix IV.

#### c. Method of Integrating Equation (2) over the Polar Angle $\theta$

Because of the $C_\infty$ symmetry of the sphere and baffle, it was possible to perform the integration of (2) over

the azimuthal angle $\varphi$ analytically. This integration is discussed in appendices II and III. After this integration the five integrals in (4) become

$$\int_{s'} dE(s, s') = \int_0^{\pi} \rho(\theta')[E_0(\theta') + E(\theta')]\sigma(\theta, \theta') \sin \theta' d\theta'/(4\pi)$$

$$\int_{a_{N'}} dE(s, a_{N'}) = \int_0^{\theta_s} \rho_N(\theta_{B'}) E_N(\theta_{B'}) \tau(\theta, \theta_{B'}) D^2 \cos \theta_{B'} \sin \theta_{B'} d\theta_{B'}/\pi, \qquad \theta < \theta_e$$

$$\int_{a_{S'}} dE(s, a_{S'}) = \int_0^{\theta_s} \rho_S(\theta_{B'})[E_0(\theta_{B'}) + E_S(\theta_{B'})] \tau(\theta, \theta_{B'}) \times D^2 \cos \theta_{B'} \sin \theta_{B'} d\theta_{B'}/\pi, \qquad \theta > \theta_e$$

$$\int_{s'} dE(a_N, s') = \int_0^{\theta_e} \rho(\theta')[E_0(\theta') + E(\theta')] \tau(\theta', \theta_B) R^2 \sin \theta' d\theta'/\pi$$

$$\int_{s'} dE(a_S, s') = \int_{\theta_e}^{\pi} \rho(\theta')[E_0(\theta') + E(\theta')] \tau(\theta', \theta_B) R^2 \sin \theta' d\theta'/\pi. \qquad (6)$$

The functions $E_0(\theta)$, $E_0(\theta_B)$, $\sigma(\theta, \theta')$, and $\tau(\theta, \theta_B)$ have been defined by (A7), (A8), (A3), and (A5), respectively. Reflection coefficients are designated by $\rho(\theta)$, $\rho_N(\theta)$, and $\rho_S(\theta)$ for sphere points, north baffle points, and south baffle points. The functions $E(\theta)$, $E_N(\theta_B)$, and $E_S(\theta_B)$ are averages over the azimuthal angle of the indirect illuminance for the sphere and baffle points. The parameters $\theta_s$ and $\theta_e$ are discussed below. The next step, integration over the polar angle, was done numerically, by a modified form of the trapazoidal rule.

To do this, the range covered by $\theta$ was divided into 20 (or 40) equal intervals $\delta\theta$. These are shown in figure 1 along with the other sphere and baffle parameters, $D$, $B$, $R$, $\theta_s$, $\theta_e$, and $\theta_i$. The angle $\theta_s$ has the value $\tan^{-1}(B/D)$; it defines the portion of the sphere shielded from the direct rays of the source. Thus, we have $E_0(\theta) = 0$ for $\theta < \theta_s$. The angle $\theta_e$ is determined by the intersection of the plane of the baffle with the surface of the sphere. It has the value $\cos^{-1}(D/R)$. Sphere points for which $\theta < \theta_e$ cannot be seen from the south side of the baffle, while those for which $\theta > \theta_e$ cannot be seen from the north side. We have adopted the restriction that $\theta_e$ must equal a value of $\theta$ which marks a boundary between two $\delta\theta$ intervals (see figure 1). This in turn limits the number of $D$ values that may be used. This is an unnecessary restriction which could be relaxed. The angles $\theta_i$ are defined by the equation

$$\theta_i = (i - \tfrac{1}{2})\delta\theta \qquad i = 1 \ldots 20(\text{or } 40). \qquad (7)$$

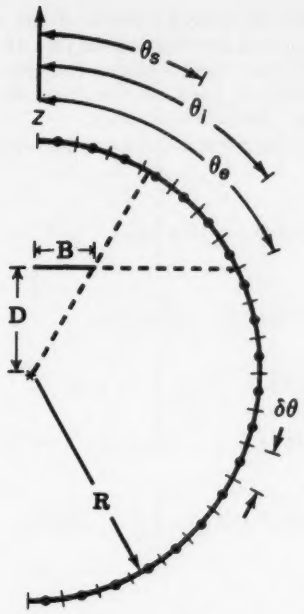


FIGURE 1. *Definition of sphere parameters.*

*R* is the radius of the sphere; *B* is the baffle radius, and *D* its distance from the center of the sphere where the light source is located. The positive *z* axis passes through the north pole. The range of the polar angle $\theta$ is divided into 20 equal intervals $\delta\theta$. Their centers are denoted by the polar angles $\theta_i$, $i = 1 \ldots 20$. $\theta_s$ defines the portion of the sphere shielded from the direct rays of the source. $\theta_e$ is determined by the intersection of the plane of the baffle with the surface of the sphere.

They thus lie at the midpoints of the $\delta\theta$ intervals. In figure 1, the circles on the perimeter of the semicircle indicate the $\theta_i$ values, and the other index lines show the boundaries of the $\delta\theta$ intervals.

The range covered by $\theta_B$ was not divided into equal intervals. Instead, the baffle radius was divided into 4 equal parts, of length $\delta B = B/4$. The centers of these intervals fall at distances $B_i$ from the center of the baffle. The $B_i$ are given by the equation $B_i = (i - \frac{1}{2})\delta B$, $i = 1 \ldots 4$. The values of $\theta_{Bi}$ corresponding to these positions are given by

$$\theta_{Bi} = \tan^{-1}(B_i/D) \qquad i = 1 \ldots 4. \qquad (8)$$

The increment $\delta\theta_B$ thus depends on $i$;

$$\delta\theta_{Bi} = \delta B(D \cos^2 \theta_{Bi})^{-1} \qquad i = 1 \ldots 4. \qquad (9)$$

Before representing the integrals in (6) by summations, let us examine how rapidly the different functions in the integrals vary over intervals of size $\delta\theta$. A study of figure 1 will show that the functions $E(\theta)$, $E_N(\theta_B)$, $E_S(\theta_B)$, and $\tau(\theta, \theta_B)$ experience only small relative changes over any of the $\delta\theta$ or $\delta\theta_B$ intervals. The functions $E_o(\theta)$, $E_o(\theta_B)$, and $\sigma(\theta, \theta')$, however, can change markedly over certain $\delta\theta$ intervals. For instance, $E_o(\theta)$ has a discontinuity in the $\delta\theta$ interval which contains $\theta_s$. To cope with these rapid variations, the slowly varying functions were assumed to be constant over the interval $\delta\theta$ and were taken out from under the inte-

gral sign. The remaining portion of the integral was then approximated by dividing $\delta\theta$ into 10 equal parts and summing over these smaller intervals. The same procedure could be used for the intervals $\delta\theta_B$ if ever there is a large variation in $E_o(\theta_B)$.

Written as a summation, the integral equation (4) has the form

$$\begin{aligned} E_i &= \sum_{j=1}^{m} [\,(DAA)_{ij} + (AA)_{ij}E_j\,] \\ &\quad + \sum_{j=1}^{4} [\,(AN)_{ij}EN_j + (DAS)_{ij} \\ &\quad + (AS)_{ij}ES_j\,] \qquad i = 1 \ldots m \\ EN_i &= \sum_{j=1}^{e} [\,(DNA)_{ij} + (NA)_{ij}E_j\,] \qquad i = 1 \ldots 4 \\ ES_i &= \sum_{j=e+1}^{m} [\,(DSA)_{ij} + (SA)_{ij}E_j\,] \qquad i = 1 \ldots 4 \end{aligned} \tag{10}$$

where $E_i$ is the value of $E(\theta)$ when $\theta = \theta_i$, $EN_i$ and $ES_i$ are the values of $E_N(\theta_B)$ and $E_S(\theta_B)$ when $\theta_B = \theta_{Bi}$, $e = \theta_e/\delta\theta$, $m = 20$ or 40, and the various coefficients are defined as follows:

$$(AA)_{ij} = \rho(\theta_j) \int_{j-}^{j+} \sigma(\theta_i, \theta) \sin\theta d\theta/(4\pi) \tag{11}$$

where $j\pm = \theta_j \pm \frac{1}{2}\delta\theta$, and the integral is evaluated numerically;

$$\begin{aligned} (AN)_{ij} &= \rho_N(\theta_{Bj})\tau(\theta_i, \theta_{Bj})D^2 \cos\theta_{Bj} \sin\theta_{Bj}\delta\theta_{Bj}/\pi \\ &\qquad i = 1 \ldots e \\ &= 0 \qquad i = e+1 \ldots m \end{aligned} \tag{12}$$

$$\begin{aligned} (AS)_{ij} &= \rho_S(\theta_{Bj})\tau(\theta_i, \theta_{Bj})D^2 \cos\theta_{Bj} \sin\theta_{Bj}\delta\theta_{Bj}/\pi \\ &\qquad i = e+1 \ldots m \\ &= 0 \qquad i = 1 \ldots e \end{aligned} \tag{13}$$

$$\begin{aligned} (NA)_{ij} &= \rho(\theta_j)\tau(\theta_j, \theta_{Bi})R^2 \sin\theta_j\delta\theta/\pi \\ &\qquad j = 1 \ldots e \\ &= 0 \qquad j = e+1 \ldots m \end{aligned} \tag{14}$$

$$\begin{aligned} (SA)_{ij} &= \rho(\theta_j)\tau(\theta_j, \theta_{Bi})R^2 \sin\theta_j\delta\theta/\pi \\ &\qquad j = e+1 \ldots m \\ &= 0 \qquad j = 1 \ldots e. \end{aligned} \tag{15}$$

The coefficient $(DAA)_{ij}$ is given by (11) with the addition of $E_0(\theta)$ under the integral sign. We can write $(DAS)_{ij} = E_o(\theta_{Bj})(AS)_{ij}$ unless $E_o(\theta_B)$ shows appreciable variation over $\delta\theta_{Bj}$, in which case $(DAS)_{ij}$ should be written as an integral over $\delta\theta_{Bj}$. The remaining coefficients $(DNA)_{ij}$ and $(DSA)_{ij}$ are equivalent to the expressions (14) and (15), each multiplied by $E_o(\theta)$ and integrated over the range $j\pm$ as in (11).

### 2.3. Solution of the Integral Equation

As outlined in (IIA), an iterative method was used to solve (10), which is the integral equation (2) approximated by a summation. Equation (10) contains the unknown quantities $E_i$, $EN_i$, and $ES_i$ and a series of coefficients which depend on the geometry and reflectance of the surfaces, and on the angular intensity distribution of the source.

A convenient zeroth order approximation is the solution of (2) for a sphere containing only a point source with a uniform intensity distribution. For area elements on a spherical surface, $T(a, a') = 1/(4R^2)$ for all $a$, $a'$. Without the baffle, we also have $S(a, a') = 1$ for all $a$, $a'$. The integral (2) in this case becomes

$$E(a) = \int_{a'} \rho(a')\,[E_0(a') + E(a')]\,da'/(4\pi R^2) \tag{16}$$

where the integration is over the sphere surface. Since this integral contains nothing which depends on $a$, we must have $E(a)$ independent of position. Letting $E(a) = E$, we can solve (16) for $E$ to get

$$E = \int_{a'} \rho(a')E_0(a')\,da' \left[1 - \int_{a'} \rho(a')\,da'/(4\pi R^2)\right]^{-1} (4\pi R^2)^{-1}. \tag{17}$$

For uniform reflectance $\rho$, and a centrally placed source with a uniform angular intensity distribution, one has $E_0(a) = E_0$, and (17) becomes

$$E = \rho E_0/(1-\rho). \tag{18}$$

The value $E$ calculated from this equation was used as the first approximation to all the unknowns, $E_i$, $EN_i$, and $ES_i$.

With $\rho = 0.9$, values of $E(a)$ satisfied (10) to better than 1 part in $10^5$ after about 35 iterations on a high speed computer for both the 24 and 44 point models. The solutions were checked to see that they satisfied the condition of flux balance. This is given by the relation

$$\int_a E_0(a)da = \int_a [1-\rho(a)][E_0(a) + E(a)]da$$

where the integrations are over all the surfaces in the sphere. The integral on the left is the total flux into the sphere, and that on the right, the total flux out.

## 3. Calculations and Results

### 3.1. Description of Source Distributions

Two source intensity distributions, each uniform in one hemisphere and zero in the other, were used for most of the calculations. Specifically, these distributions were

$$\begin{aligned} I_N(\theta) &\equiv 2 \text{ lm/sr} && 0 \leqq \theta < \pi/2 \\ &\equiv 0 && \pi/2 \leqq \theta \leqq \pi \\ I_S(\theta) &\equiv 0 && 0 \leqq \theta < \pi/2 \\ &\equiv 2 && \pi/2 \leqq \theta \leqq \pi. \end{aligned} \tag{19}$$

The total flux $F_0$ in each case is, by (A10), equal to $4\pi$ lm.

With the sphere geometry discussed in the next section, an additional group of distributions having the form

$$I_i(\theta) \equiv [\sin\theta_i \sin(\tfrac{1}{2}\delta\theta)]^{-1} \text{ lm/sr} \qquad \theta_i - \tfrac{1}{2}\delta\theta < \theta < \theta_i + \tfrac{1}{2}\delta\theta$$

$$\equiv 0 \qquad \text{(all other } \theta \text{ values)} \tag{20}$$

was used. The $\theta_i$ are given by (7). The total flux is the same for each distribution and is equal to $4\pi$ lm. We shall discuss later how the results obtained from this series of distributions can be used to determine $E(a)$ for an arbitrary source distribution.

### 3.2. Results for a Reference Sphere

For much of the work, a particular set of sphere parameters was used. They were chosen to correspond roughly to those of a typical experimental sphere. They were, $R = 1$, $B = 0.1$, and $D = 0.31$ m. A uniform reflection coefficient of 0.9 was used for all surfaces. Calculated values of the indirect illuminance $E(\theta)$ for the 24-point model are shown as polar plots in figures 2 and 3 for the north and south hemispherical source distributions, respectively. If there were no baffle, $E(\theta)$ would have a uniform value of 9 lm/m$^2$. The $E(\theta)$ values shown in figures 2 and 3 are lower than this on the average because of light absorption by the baffle. The $E(\theta)$ values are enhanced on the side of the sphere opposite that being directly illuminated. Values of the indirect illuminance of the baffle show the same effect. They are shown in table 1 for the reference sphere and the hemispherical distributions. For the north distribution, the north side of the baffle, being opposite the directly illuminated surfaces, receives more indirect illumination than the south side. The opposite situation holds for the south distribution.

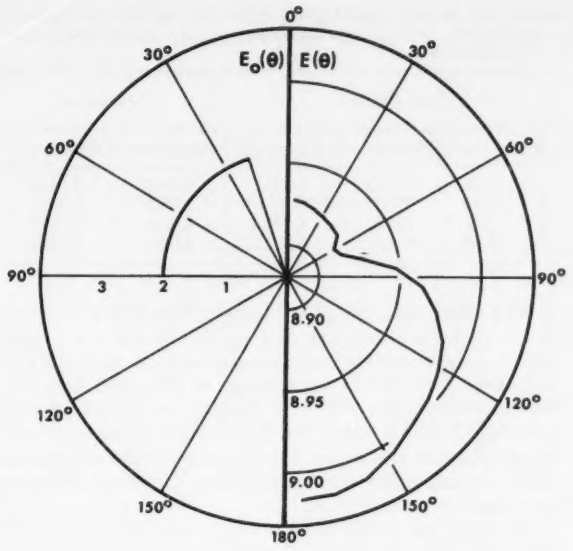


FIGURE 2. *Variation with the polar angle of the indirect illuminance* E(θ) *for the northward directed hemispherical source distribution, and the reference sphere geometry.*

$E_o(\theta)$ is the direct illuminance.

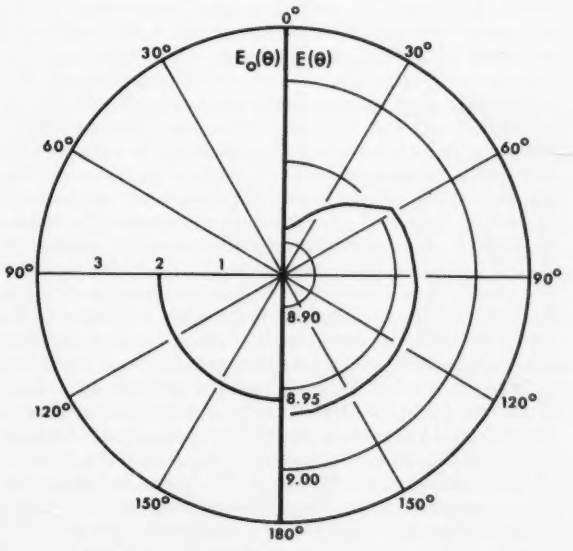


FIGURE 3. *Variation with the polar angle of the indirect illuminance* E(θ) *for the southward directed hemispherical source distribution, and the reference sphere geometry.*

$E_o(\theta)$ is the direct illuminance.

TABLE 1. *Indirect illuminance of baffle for reference sphere dimensions, $\rho = 0.9$, hemispherical source distributions, and 24-point model*

| | | $I_N(\theta)$ (lm/sr) | | $I_S(\theta)$(lm/sr) | |
|---|---|---|---|---|---|
| $i$ | $\theta_{Bi}$(deg) | $EN_i$(lm/m²) | $ES_i$(lm/m²) | $EN_i$(lm/m²) | $ES_i$(lm/m²) |
| 1 | 2.32 | 9.5510 | 8.2733 | 8.0889 | 9.7416 |
| 2 | 6.94 | 9.5522 | 8.2736 | 8.0888 | 9.7413 |
| 3 | 11.46 | 9.5547 | 8.2743 | 8.0886 | 9.7407 |
| 4 | 15.86 | 9.5583 | 8.2754 | 8.0883 | 9.7398 |

This table also shows the large difference in indirect illuminance of the north and south sides of the baffle, and its large dependence on the source distribution. Actually, it is the large change in $EN_i$ which is primarily responsible for the change in $E_1 \approx E(\theta=0)$ (see figs. 2 and 3) when the distribution shifts from one hemisphere to the other. The changes in the amount of light coming to the $\theta_1$ position from the other surfaces are small by comparison.

Because the detector would normally be at the north pole, it is the change in $E_1$ that is of primary interest. For the reference sphere, $E_1$ changes by 0.25 percent when the hemispherical source distribution is switched from north to south; values of $E(\theta)$ at other $\theta$ values change to a greater or lesser degree.

### 3.3. Effect of Changing the Baffle Position

The effect of changing the position of the baffle along the polar axis is shown in figure 4. Here, values of $E(\theta)$ are plotted as a function of $\theta$ for four different baffle positions $D$, including that occurring in the reference sphere. The radius of the baffle was held constant at $B=0.1$ m. For each case, there are two curves corresponding to the two hemispherical distributions. That arising from the north distribution is labeled $N$. Of the four positions, the difference in $E_1$ between the two source distributions is smallest for the baffle position used in the reference sphere. This position does not, however, minimize this difference. A plot of $E_1(N)-E_1(S)$ versus $D$ at constant $B$, where $N$ and $S$ designate the distributions, is shown in figure 5 by the filled-in circles. This plot shows that for $D \approx 0.28$ m there would be no difference at all in $E_1$ between the two distributions. This optimum baffle position differs considerably from the value of $D=$ 0.372 R, which minimizes the screened areas of the sphere surface [3]. Minimizing the screened areas does, however, minimize the change in $E(\theta)$ averaged over the sphere that occurs when the hemispherical source is directed from north to south. The sum of the squares of the differences $E_i(N)-E_i(S)$, each weighted by sin $\theta_i$ to account for the different sizes of the sphere areas represented by the $\theta_i$, was smaller for $D=0.38$ than for $D=0.31$, 0.45, or 0.28 m. (Values of $E_i(N)$ and $E_i(S)$ for $D=0.28$ and 0.38 m were estimated by interpolation between the curves shown in fig. 4.) Thus, while the dependence of the $E(\theta)$ values around the sphere on the source distribution is minimized by $D=0.372$, the experimentally important quantity

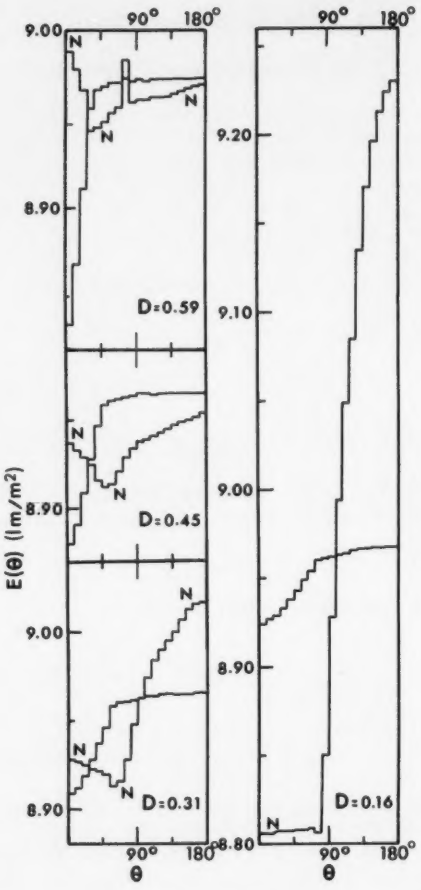


FIGURE 4. *Indirect illuminance* E($\theta$) *versus* $\theta$ *arising from the north (labeled* N*) and south hemispherical distributions for different values of the baffle position.*

The other parameters have reference sphere values.

$E_1(N)-E_1(S)$ is minimized by $D=0.28$ m. At this stage in the calculations it is not possible to generalize this result to other source distributions. The optimum baffle position may not be the same for source distributions differing from the hemispherical ones considered here.

### 3.4. Effect of Changing the Baffle Radius

At a fixed value of $D$, decreasing the baffle radius will decrease the error $E_1(N) - E_1(S)$ made in observing the hemispherical distributions. Examples of this are shown in figure 5. The three points connected by the dotted line correspond to combinations of $B$ and $D$ which keep constant the area of the sphere screened by the baffle from the observation port.

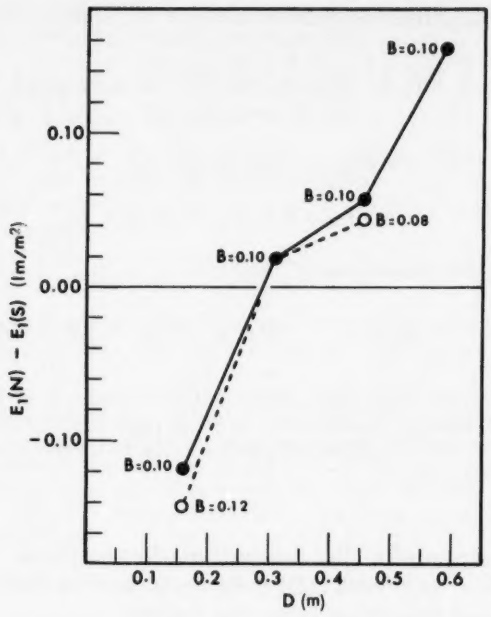


FIGURE 5. *Difference* $E_1(N) - E_1(S)$ *between the indirect illuminances near the north pole produced by the north and south hemispherical distributions as a function of baffle radius and position.*

### 3.5. Determination of $E(\theta \approx 0)$ for an Arbitrary Source Intensity Distribution $I(\theta)$

Calculations of $E_1$ using the reference geometry with the 24-point model were done for a number of the distributions $I_i(\theta)$ defined by (20). Several of the $E_1$ values were obtained from the others by graphical interpolation. All are shown in table 2.

Consider a source with an intensity distribution $I(\theta)$ which can be approximated by a linear combination of the $I_i(\theta)$ distributions. Let

$$I(\theta) = \sum_{i=1}^{20} w_i I_i(\theta),$$

where the weights $w_i$ satisfy the relation

$$\sum_{i=1}^{20} w_i = 1.$$

Then, if we define $E_1(i)$ as the value of $E_1$ calculated for the distribution $I_i(\theta)$ we have simply

$$E_1 = \sum_{i=1}^{20} w_i E_1(i),$$

where $E_1$ is the value for the distribution $I(\theta)$. Values of $E_1(i)$ from table 2 were used with appropriate weights to calculate $E_1$ for the hemispherical distributions $I_N(\theta)$ and $I_S(\theta)$. The results differed by 0.03 percent from those calculated directly from $I_N(\theta)$ and $I_S(\theta)$. The use of interpolated values for some of the $E_1(i)$ is probably responsible for most of the difference.

TABLE 2. *Indirect illuminance of north pole region for reference sphere dimensions,* $\rho = 0.9$, *source distributions* $I_1(\theta)$, *and 24-point model*

| $i$ | $\theta_i$ (deg) | $I_i(\theta)$ (lm/sr) | $E_1$ (lm/m²) |
|---|---|---|---|
| 1 | 4.5 | 159.4 | 7.8329 |
| 2 | 13.5 | 54.65 | 8.1143 |
| 3 | 22.5 | 33.33 | 9.0464 |
| 4 | 31.5 | 24.41 | 9.0216 |
| 5 | 40.5 | 19.64 | 9.0010 |
| 6 | 49.5 | 16.77 | 8.9823 |
| 7 | 58.5 | 14.96 | 8.9666 |
| 8 | 67.5 | 13.81 | 8.9542 |
| 9 | 76.5 | 13.12 | [a] 8.951 |
| 10 | 85.5 | 12.79 | [a] 8.950 |
| 11 | 94.5 | 12.79 | 8.9500 |
| 12 | 103.5 | 13.12 | [a] 8.950 |
| 13 | 112.5 | 13.81 | [a] 8.949 |
| 14 | 121.5 | 14.96 | 8.9487 |
| 15 | 130.5 | 16.77 | [a] 8.947 |
| 16 | 139.5 | 19.64 | [a] 8.944 |
| 17 | 148.5 | 24.41 | 8.9387 |
| 18 | 157.5 | 33.33 | 8.8056 |
| 19 | 166.5 | 54.65 | 8.4642 |
| 20 | 175.5 | 159.4 | 8.0655 |

[a] These values were obtained by graphical interpolation between the unmarked values.

## 4. Discussion

The integral equation description of the integrating sphere offers an accurate way to determine the errors caused by the screening effects of objects inside the sphere. While its numerical solution is possible, in principle, for any sphere geometry, a great simplification results when an $\infty$-fold axis of symmetry exists for the various surfaces and their reflection coefficients. The computation time is so short for such a system, that it becomes feasible to improve the accuracy by using smaller area elements and to extend the calculations to spheres containing several objects.

The effect of increasing the number of sphere points from 20 to 40 is shown in table 3 for the reference sphere dimensions. The biggest change in the $E_i$ values occurred for $E_1$. There were decreases in $E_1(N)$ and $E_1(S)$ of around 0.03 percent and an increase in their difference $E_1(N) - E_1(S)$ of 3.1 percent. Further improvements in the accuracy of the calculation could be achieved by using more points, and/or by using a better approximation to the integral.

An extension of the method to spherical and cylindrical sources located anywhere along the sphere axis appears feasible. This would greatly increase the number of systems to which the method could be applied.

TABLE 3. *Effect on indirect illuminance near[a] the north pole of decreasing the interval size $\delta\theta$, for reference sphere dimensions, $\rho=0.9$, and hemispherical source distributions*

| | 20 sphere points | 40 sphere points[b] | Change (percent) |
|---|---|---|---|
| $E_1(N)$ | 8.9277 lm/m² | 8.9259 lm/m² | 0.020 |
| $E_1(S)$ | 8.9087 | 8.9063 | 0.027 |
| $E_1(N)-E_1(S)$ | 0.0190 | 0.0196 | −3.1 |

[a] The $E(\theta)$ values given here are those at $\theta=4.5°$.

[b] The values at $\theta=4.5°$ for the 40 sphere point case were obtained by linear interpolation between the $E(\theta)$ values calculated at $\theta=2.25$ and 6.75°.

The writer thanks S. R. Kraft for suggesting the integral equation approach to the baffle problem and for guidance in the initial phase of the work. Acknowledgment is also given to W. B. Fussel for many valuable discussions.

## References

[1] Moon, P., J. Opt. Soc. Am. **30**, 195 (1940).
[2] Jacquez, J. A., Kuppenheim, H. F., J. Opt. Soc. Am. **45**, 460 (1955).
[3] Rosa, E. B., and Taylor, A. H., Sci. Papers Bur. Standards No. 447, p. 281 (1922).

(Paper 77A3-773)

## 6. Appendix I: Azimuthal dependence of $S(a, a')$ when both $a$ and $a'$ are on the Sphere Surface

Consider two points $(\theta, \varphi)$ and $(\theta', \varphi')$ on the surface of the sphere. These points determine a line which intersects the plane containing the baffle at some point. Let $\beta$ be the distance in the plane of the baffle between this point of intersection and the polar axis. Because of the $C_\infty$ symmetry of the system, the azimuthal dependence of $\beta$ can be specified in terms of the difference $\varphi-\varphi'$. One can thus let $\varphi=0$ and calculate $\beta$ as a function of the three parameters $\theta$, $\theta'$, and $\varphi'$. It can be shown that

$$\beta^2=f+g\cos\varphi' \tag{A1}$$

where

$$f=\tfrac{1}{4}R^2\left[(1-\Gamma)^2\sin^2\theta+(1+\Gamma)^2\sin^2\theta'\right]$$

$$g=\tfrac{1}{2}R^2(1-\Gamma)(1+\Gamma)\sin\theta\sin\theta'$$

$$\Gamma=[2D-R(\cos\theta+\cos\theta')][R(\cos\theta'-\cos\theta)]^{-1}.$$

The line between $(\theta, \varphi)$ and $(\theta', \varphi')$ will intersect the baffle under the conditions, $0\leqq\theta<\theta_e<\theta'\leqq\pi$, and $\beta^2\leqq B^2$, where $\theta_e$ is the polar angle determined by the intersection of the baffle plane with the surface of the sphere (see fig. 1). Let $\varphi_s'$ be that value of $\varphi'$ for which $\beta^2=B^2$. From (A1) we have

$$\varphi_s'=\cos^{-1}\left[(B^2-f)/g\right]. \tag{A2}$$

The azimuthal dependence of $S(\theta;\theta',\varphi')$ is thus

$S(\theta;\theta',\varphi')=1$ for $0\leqq\varphi'\leqq\varphi_s'$ and

$$2\pi-\varphi_s'\leqq\varphi'\leqq2\pi$$

$$=0 \text{ for } \varphi_s'<\varphi'<2\pi-\varphi_s'$$

$$=0 \text{ for } 0\leqq\theta<\theta_e<\theta'\leqq\pi.$$

For the integral over $\varphi'$ we have

$$\sigma(\theta,\theta')\equiv\int_0^{2\pi}S(\theta;\theta',\varphi')d\varphi'=2\varphi_s'. \tag{A3}$$

The azimuthal integration in the evaluation of the first integral $\int_{s'}dE(s,s')$ in (6) is thus accomplished since $S(a, a')$ is the only factor in the integrand which contains $\varphi'$.

## 7. Appendix II: Azimuthal Dependence of $T(a, a')$ When One Point Is on the Baffle and the Other Is on the Sphere

Consider a point $(\theta, \varphi)$ on the sphere surface and a point $(\theta_B, \varphi_B)$ on the baffle. It can be shown that

$$T(\theta,\varphi;\theta_B,\varphi_B)=k[f_1+g_1\cos(\varphi-\varphi_B)]$$
$$[f_2+g_2\cos(\varphi-\varphi_B)]^{-2} \tag{A4}$$

where

$$k=\pm(D\cos^2\theta_B-R\cos\theta)$$

$$f_1=R-D\cos^2\theta_B\cos\theta$$

$$g_1=-D\cos\theta_B\sin\theta_B\sin\theta$$

$$f_2=R^2+D\cos^2\theta_B(D-2R\cos\theta)$$

$$g_2=-2RD\cos\theta_B\sin\theta_B\sin\theta.$$

In the expression for $k$, the negative sign is used for baffle points on the north side, and the positive sign for points on the south side.

As one would expect from the $C_\infty$ symmetry, $T(\theta,\varphi;\theta_B,\varphi_B)$ depends on the difference $\varphi-\varphi_B$ between the azimuthal angles. The integral over either azimuthal angle is

$$\tau(\theta,\theta_B)\equiv\int_0^{2\pi}T(\theta,\varphi;\theta_B,\varphi_B)d\varphi$$

$$=\int_0^{2\pi}T(\theta,\varphi;\theta_B,\varphi_B)d\varphi_B$$

$$=2\pi k(f_1f_2-g_1g_2)(f_2^2-g_2^2)^{-3/2}. \tag{A5}$$

This function $\tau(\theta, \theta_B)$ furnishes the azimuthal portion of all the integrals in (4) except the first.

## 8. Appendix III: Determination of the Direct Illuminance $E_0(a)$

Let $I(\theta, \varphi)$ be the angular intensity distribution of the point source in lumen/steradian. The direct illuminance $E_0(\theta, \varphi, r)$ at a point $(\theta, \varphi, r)$ is given by the expression

$$E_0(\theta, \varphi, r) = I(\theta, \varphi)(\mathbf{r} \cdot \mathbf{n})r^{-3} \tag{A6}$$

where $\mathbf{r}$ is the vector from the source (located at the origin) to the point and $\mathbf{n}$ is the unit outward normal from the area element about the point. For sphere points $(\mathbf{r} \cdot \mathbf{n})r^{-3}$ has the value $1/R^2$, while for baffle points it has the value $1/(D^2 \cos \theta_B)$. When $\rho(a)$ has $C_\infty$ symmetry, $E(a)$ at the poles is independent of the azimuthal dependence of $I(\theta, \varphi)$. If the observation point is at a pole it is permissible (see appendix IV) to use the average of $E_0(\theta, \varphi)$ over $\varphi$ in the calculation.

For points on the sphere surface, excepting those screened from the source by the baffle, we have

$$E_0(\theta) \equiv (1/2\pi) \int_0^{2\pi} E_0(\theta, \varphi)\, d\varphi = (1/2\pi) \int_0^{2\pi} I(\theta, \varphi)\, d\varphi / R^2. \tag{A7}$$

For baffle points, we have

$$E_0(\theta_B) \equiv (1/2\pi) \int_0^{2\pi} E_0(\theta_B, \varphi_B)\, d\varphi_B = (D^2 \cos \theta_B)^{-1} (1/2\pi) \int_0^{2\pi} I(\theta_B, \varphi_B)\, d\varphi_B. \tag{A8}$$

The north, south designation is not needed here, since $E_0(\theta_B)$ is zero on the north side of the baffle. One need only know $I(\theta, \varphi)$ averaged over $\varphi$; i.e.,

$$I(\theta) \equiv (1/2\pi) \int_0^{2\pi} I(\theta, \varphi)\, d\varphi. \tag{A9}$$

The total flux $F_0$ from this source is given by the integral

$$F_0 = \int_{4\pi} I(\theta, \varphi)\, d\Omega = 2\pi \int_0^{\pi} I(\theta) \sin \theta d\theta \tag{A10}$$

where $d\Omega$ is the element of solid angle and the integration is over $4\pi$ steradians.

## 9. Appendix IV: On the Absence of Symmetry Restrictions on the Source Intensity Distribution

When the reflection coefficient has $C_\infty$ symmetry, and the observation point is at the pole, there are no symmetry restrictions on the angular intensity distribution of the source. To see why this is so consider the integral equation (2) for points on the sphere near the north pole.

$$E(\theta, \varphi) = \int_0^{\pi} \rho(\theta') \left[ \int_0^{2\pi} [E_0(\theta', \varphi') + E(\theta', \varphi')] S(\theta, \varphi; \theta', \varphi') d\varphi' \right] \times \sin \theta' d\theta' / 4\pi + \int_0^{\theta_s} \rho_N(\theta_{B'}) \left[ \int_0^{2\pi} E_N(\theta_{B'}, \varphi_{B'}) T(\theta, \varphi; \theta', \varphi') d\varphi_{B'} \right] \times D^2 \cos \theta_{B'} \sin \theta_{B'} d\theta_{B'} / \pi$$

The average of $E(\theta, \varphi)$ over $\varphi$ is

$$E(\theta) \equiv (1/2\pi) \int_0^{2\pi} E(\theta, \varphi) d\varphi = \int_0^{\pi} \rho(\theta') [E_0(\theta') + E(\theta')] \sigma(\theta, \theta') \sin \theta' d\theta' / 4\pi + \int_0^{\theta_s} \rho_N(\theta_{B'}) E_N(\theta_{B'}) \tau(\theta, \theta_{B'}) D^2 \cos \theta_{B'} \sin \theta_{B'} d\theta' / \pi \tag{A11}$$

where we have used the relations (A3) and (A5). The function $E_0(\theta)$ is the average of $E_0(\theta, \varphi)$ over $\varphi$ as defined by (A7), and $E_N(\theta_B)$ is defined for the baffle points in the same way that $E(\theta)$ was defined for the sphere points. This expression shows that $E(a)$ values averaged over the azimuthal angle will satisfy the integral equation.

The flux striking a small round observation port of radius $p$, centered on the north pole of the sphere, is given by the integral

$$\int_0^{2\pi} \left[ \int_0^{\theta_p} E(\theta, \varphi) \sin \theta d\theta \right] d\varphi = 2\pi \int_0^{\theta_p} E(\theta) \sin \theta d\theta$$

where the upper limit of integration is equal to $\sin^{-1}(p/R)$. As (A11) shows, this integral depends only on the average azimuthal dependence of the source intensity distribution.

JOURNAL OF RESEARCH of the National Bureau of Standards—A. Physics and Chemistry
Vol. 77A, No. 3, May–June 1973

# Crystallization of Random Copolymers

**Isaac C. Sanchez* and R. K. Eby**

**Institute for Materials Research, National Bureau of Standards, Washington, D.C. 20234**

**(January 18, 1973)**

A theory of crystallization is formulated for random copolymers which crystallize with the noncrystallizable co-units incorporated into the crystalline lattice as defects. The appropriate melting point equation and other associated thermodynamic properties are derived for this model as a function of crystal thickness and comonomer concentration. The formation of lamellar type morphology is assumed to be a kinetically determined phenomena and nucleation theory is utilized accordingly. The isothermal lamella thickness is predicted to increase in a definitive manner as the noncrystallizable comonomer concentration $X$ increases, while the associated isothermal growth rate is predicted to decrease. The variation of lamella thickness with $X$ when the copolymer is quenched or cooled at a uniform rate is also qualitatively predicted. Under these conditions lamella thickness decreases with increasing $X$, which is in accord with previous experimental observations on random copolymers of tetrafluoroethylene and hexafluoropropylene as well as other random copolymers. Theory also suggests how the surface free energy parameters $\sigma_e$ and $\sigma$ can be determined from isothermal crystallization experiments for a series of random copolymers of varying composition.

Key words: Copolymers; crystallization; growth rate; lamella thickness; melting temperature.

## 1. Introduction

A random copolymer can potentially crystallize in two extreme ways. It can form a two-phase system in which the crystalline phase is composed entirely of $A$ units and is in equilibrium with a mixed amorphous phase of $A$ units and noncrystallizable comonomer $B$ units (comonomer exclusion). Alternatively, the copolymer may form a two phase system in which the crystalline phase is a solid solution of $A$ and $B$ units; the comonomer $B$ units produce defects in the crystalline $A$ lattice and both phases have the same composition (comonomer inclusion). The question arises as to which state is more characteristic of the experimentally observed crystalline state. One can try to answer this question by invoking thermodynamics: if the observed state is a true thermodynamic state, then we need only determine the state of lowest free energy. Figure 1 schematically illustrates the two models.

In Flory's theory of copolymer crystallization [1][1] it is tacitly assumed that the state of lowest free energy is the two phase system where the comonomer $B$ units are excluded from the crystal. However, on *a priori* grounds, there is no reason to believe that the exclusion model is thermodynamically more stable than the inclusion model. Moreover, the question as to which state is more stable is largely academic because the observed state probably corresponds to a metastable state determined by kinetic factors. This is certainly the case in homopolymer crystallization. Thick crystals are thermodynamically more stable than thin lamellar crystals with high surface to volume ratios; nevertheless, metastable lamellar morphology develops under the usual kinetic conditions of homopolymer crystallization.

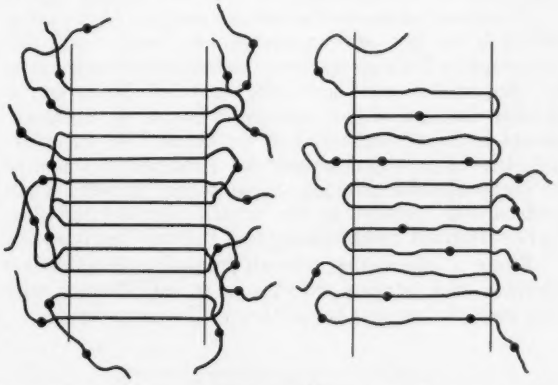

FIGURE 1. *Two extreme representations of lamellar random copolymer crystals, the exclusion model (left) and inclusion model (right).*

Real copolymer crystals may exhibit a morphology intermediate to the two extremes in figure 1. In the present paper, a simple theory for random copolymer

*Present address: Polymer Science and Engineering, University of Massachusetts, Amherst, Mass. 01002. Portions of this work were carried out while an NRC–NAS Postdoctoral Research Associate at NBS.

[1]Figures in brackets indicate the literature references at the end of this paper.

crystallization is formulated which adopts the view that lamella crystalline morphology is kinetically determined and that the inclusion model is more characteristic of the crystalline state. A preliminary account of this theory has been given previously [2].

In section 2 melting temperature relationships are derived as a function of copolymer composition and crystal thickness. The heats of fusion associated with the two models are also considered. In section 3 an elementary kinetic theory of crystallization is formulated and in section 4 the conclusions of the study are briefly outlined.

## 2. Thermodynamics

### 2.1. Equilibrium Melting Point

Melting point equations have previously been derived for the exclusion [1] and inclusion [3], [4] models. What follows is an alternative derivation of the equilibrium melting point for the inclusion model. First, we enumerate the assumptions upon which the derivation rests:

1. The heat of fusion $\Delta H$ and the entropy of fusion $\Delta S$ are independent of temperature; $\Delta H(T) = \Delta H(T_m^0)$ and $\Delta S(T) = \Delta S(T_m^0) = \Delta H(T_m^0)/T_m^0$ where $T_m^0$ is the equilibrium melting point of the homopolymer.

2. Compositional changes do not affect the entropy of fusion; if $X$ is the mole fraction of $B$ co-units in the copolymers, then $\Delta S(T, X) = \Delta S(T, 0) = \Delta S(T_m^0)$.

3. The heat of fusion is a simple linear function of the number of comonomer units that enter the crystal:

$$\Delta H(T, X) = \Delta H(T_m^0) - X\,\Delta H_d \tag{1}$$

where $\Delta H_d$ is the heat of transition (an excess enthalpy) associated with the formation of a defect in the crystalline lattice, $\Delta H_d \geq 0$.

Assumption 1 is the usual and simplest approximation employed in determining the bulk free energy difference between melt and crystal; an analysis of the error inherent in this approximation has been made [5]. Assumption 2 is a good approximation if the composition of the crystal and melt are identical. Moreover, a sizable fraction of the entropy of fusion is configurational entropy (estimated to be about 75% for polyethylene [6]) which should be relatively insensitive to compositional changes. Assumption 3 is valid when comonomer defects in the crystal are isolated (low concentrations required) so that they do not interact.

When a copolymer crystal, free of nonequilibrium defects and surface effects, is in equilibrium with the melt, the melting temperature $T_m^0$ is given by

$$T_m^0(X) = \frac{\Delta H(T_m^0\ (X))}{\Delta S(T_m^0\ (X))}. \tag{2a}$$

Utilization of the previously mentioned assumptions then yields

$$T_m^0(X) = \left[\frac{\Delta H(T_m^0,\ X))}{\Delta H(T_m^0)}\right] T_m^0 = (1 - AX)T_m^0 \tag{2b}$$

where $A \equiv \Delta H_d/\Delta H(T_m^0)$.

### 2.2. Melting Temperature of Lamellar Crystals

Small crystals with high surface to volume ratios will melt at temperatures below the equilibrium melting temperature $T_m^0$. Denoting by $\Delta G$ the bulk free energy difference between copolymer crystal and melt, a thin lamellar crystal of thickness $l$ is in equilibrium with the melt when [5]

$$\Delta G - 2\sigma_e/l = 0 \tag{3}$$

where $\sigma_e$ is the surface free energy of the basal plane of the lamellar crystal. For $T \leq T_m^0$ the bulk free energy difference $\Delta G(T, X)$ is given by

$$\Delta G(T, X) = \Delta H(T, X) - T\Delta S(T, X) \tag{4a}$$

and thus from assumption 2 and eqs (1) and (2)

$$\Delta G(T, X) = \Delta H(T_m^0)(T_m^0(X) - T)/T_m^0. \tag{4b}$$

Combining eqs (2b), (3), and (4b), the following equation for the melting temperature $T_m(l)$ of a lamellar copolymer crystal obtains:

$$T_m(l) = \left\{1 - \frac{2\sigma_e}{\Delta H(T_m^0)}\,(1/l) - AX\right\} T_m^0. \tag{5}$$

Notice that eq (5) reduces to eq (2b) for large $l$, as it should.

Equation (5) is slightly different in functional form than the melting point equation first derived by Eby [3], [4] for solid solution copolymer crystals. In addition to the assumptions mentioned above, there is an unnecessary series expansion; the effect of comonomer concentration and finite crystal thickness on the melting temperature is evaluated to first order (higher order corrections which are small are ignored). The present derivation has avoided the use of series expansions and thus the melting point depression $(T_m^0 - T_m)$ is predicted to be slightly larger by a factor $T_m^0/T_m$ than the original Eby equation. However, refitting[2] the data of [4] yielded constants which agreed within the limits of error with the former ones and which did not alter the conclusions in [4].

As mentioned previously, Flory [1] assumes that the copolymer crystal is composed entirely of $A$ units; $B$ co-units are excluded and remain in an amorphous phase. The melting point depression is caused by the fact that preferential ordering of the copolymer chains is required for crystallization (an entropy effect) whereas in the present case, the melting point depression is caused by the defective heat of fusion that accompanies the crystallization (an enthalpy effect).

[2] Melting point data [4] for tetrafluoroethylene and hexafluoroethylene random copolymers were reanalyzed using eq (5). The following new results were obtained: $T_m^0 = 612 \pm 4$ K, $\sigma_e = 61 \pm 23$ ergs/cm$^2$, and $\Delta H_d = 0.042 \pm 0.003$ eV. For the purposes of comparison the the original results were $T_m^0 = 617 \pm 5$ K, $\sigma_e = 77 \pm 27$ ergs/cm$^2$ and $\Delta H_d = 0.047 \pm 0.003$ eV.

For a random copolymer and low comonomer concentrations, the Flory equation reduces to

$$T_m \simeq (1 - A'X)T_m^0 \tag{6}$$

where $A' = RT_m/\Delta H(T_m^0)$. Comparison of eq (6) with eq (2b) shows that they are identical in form except that $RT_m$ has replaced $\Delta H_d$ in eq (2b)—a manifestation of the different effects considered (entropy versus enthalpy). Although Flory did not consider the effect of crystal size on the melting temperature, such an effect is obtainable from his theory [see eq (14) of ref. [1]]. The resulting equation is similar to eq (5) which implies that melting temperature data taken as a function of copolymer composition and crystal thickness cannot distinguish between the comonomer exclusion and inclusion crystal models.

### 2.3. Heats of Fusion

Crystallinity studies (density or x-ray) combined with calorimetric studies can, in principle, determine which model is more appropriate. By assuming that enthalpy effects are additive it can be shown in a straightforward fashion that the observed heat of fusion $\Delta H^*$ for the *inclusion* model is given by

$$\Delta H^*/\chi = \Delta H - X\Delta H_d - 2\Delta H_e/l \tag{7}$$

where $\chi$ is the degree of crystallinity and $\Delta H_e$ is the excess enthalpy associated with forming the basal surfaces of the lamellar crystal. However, for the *exclusion* model, we have

$$\Delta H^*/\chi = \Delta H - 2\Delta H_e/l. \tag{8}$$

Note that for the exclusion model $\Delta H^*/\chi$ is independent of the co-unit concentration $X$ whereas it is linearly dependent on $X$ for the inclusion model.

## 3. Kinetics

### 3.1. Lamella Thickness

When nucleation theory is applied to the crystallization of linear chain molecules, the theoretical crystal thickness $l^*$ is given by [7]

$$l^* = l_c + \delta l \tag{9}$$

where $l_c = 2\sigma_e/\Delta G$ is the critical crystal thickness and $\delta l$ is a small additive term (usually about 10 Å) which is a weak function of termperature in the usual crystallization temperature range. Crystal thicknesses less than $l_c$ are thermodynamically unstable.

The experimentally observed crystal thickness $l_{obs}$ may differ from $l^*$ because crystals may thicken with time [8]. In general,

$$l_{obs} = l_c + C(T) \tag{10}$$

where $C(T)$ includes $\delta l$ plus any thickening that may occur at the crystallization temperature $T$. Of course, $C(T)$ is also a function of time, but it will be assumed throughout that we are dealing with the long time (or an isochronal) value of $C(T)$. The thermodynamic driving force $\Delta G$ for the crystallization of a random copolymer is given by eq (4b); thus

$$l_{obs} = \frac{2\sigma_e T_m^0}{\Delta H(T_m^0)(T_m^0(X) - T)} + C(T). \tag{11}$$

If $\sigma_e$ is independent of the comonomer concentration $X$, then

$$l_{obs} = l_c^0\left[1 + \frac{T_m^0 - T_m^0(X)}{T_m^0(X) - T}\right] + C(T) \tag{12}$$

or if $C(T)$ is independent of $X$,

$$= l_{obs}^0 + l_c^0\left[\frac{T_m^0 - T_m^0(X)}{T_m^0(X) - T}\right] \equiv l_{obs}^0 + l_c^0 f(X, T) \tag{13}$$

where the superscript 0 on $l_{obs}$ and $l_c$ indicates that these quantities refer to the homopolymer; from eq (2b) we have

$$f(X, T) = AX/[(1 - T/T_m^0) - AX] \tag{14}$$

Note that $f(X, T)$ increases monotonically with both $X$ and $T$; that is, $\partial f/\partial T > 0$ and $\partial f/\partial X > 0$. Therefore, eqs (13) and (14) show that *isothermal* plots of $l_{obs}$, say at $T_1$, against $f(X, T_1)$ are linear with intercept $l_{obs}^0(T_1)$ and positive slope $l_c^0(T_1)$. Random copolymers of various comonomer concentrations crystallized at the same temperature should form crystals with thicknesses that increase with increasing comonomer concentration (see fig. 2). For low concentrations we have

$$f(X, T) = \left(\frac{AT_m^0}{T_m^0 - T}\right)X \tag{15}$$

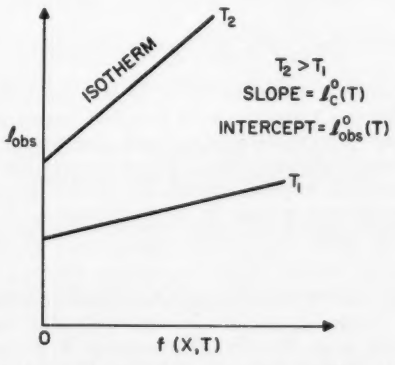


FIGURE 2. *Variation of theoretical, isothermal lamellar thickness with the comonomer concentration* X.

The variable $f(X, T)$ plotted along the abscissa increases monotonically with $X$ and is proportional to $X$ for small $X$.

and thus, isothermal plots of $l_{obs}$ against $X$ are initially linear with a positive slope equal to $l_c^0(T)AT_m^0/(T_m^0 - T)$.

The derivation of eq (13) from eq (12) assumed that the thickening that occurs at the crystallization temperature $T$ was independent of the comonomer concentration $X$. A better approximation is

$$\left.\frac{\partial C}{\partial X}\right|_T = \text{constant.} \tag{16}$$

In general

$$C(T, X) = C(T, 0) + \left.\frac{\partial C}{\partial X}\right|_T X + \left.\frac{\partial^2 C}{\partial X^2}\right|_T \frac{X^2}{2!} + \cdots \tag{17}$$

but when eq (16) holds, eq (13) becomes

$$l_{obs} = l_{obs}^0 + l_c^0 f(X, T) + \left.\frac{\partial C}{\partial X}\right|_T X. \tag{18}$$

Even if approximation (16) is not strictly true, eq (18) will hold approximately when second and higher order terms in eq (17) are small compared to the first order term.

The equilibrium theory of Flory [1] for the exclusion model also predicts that crystallite thicknesses increase with increasing $X$ for a random copolymer. At first this result for the exclusion model seems unreasonable because long uninterrupted sequence lengths of crystallizable units are decreasing with increasing $X$. However, in the Flory theory a compensating decrease in crystallinity accompanies the increase in crystallite thickness. Thus, both the exclusion and inclusion models (equilibrium and kinetic theories, respectively) predict that the isothermal crystal thickness increases with increasing concentration of the non-crystallizable co-unit.

### 3.2. Nucleation and Crystal Growth

In the simplest approximation, the nucleation rate $S$ of a coherent surface nucleus is given by [7–9]

$$S = S_0 \exp(-\Delta G^*/RT) \exp(-2\sigma l_c/RT) \tag{19a}$$

where $S_0$ is a constant, $\Delta G^*$ is the activation free energy for the transport of a polymer segment across the melt-crystal interface and $\sigma$ is the lateral surface free energy of the lamellar polymer crystal. For nucleation controlled crystal growth, the lateral growth rate of a copolymer crystal is proportional to $S$ [7, 10]. Therefore, since $l_c = l_c^0\ [1 + f(X, T)]$ from eq (12), we have

$$\ln S + \Delta G^*/RT = -2\sigma l_c^0\ [1 + f(X, T)]/RT + \ln S_0. \tag{19b}$$

Equation (19b) suggests that isothermal plots of $\ln S + \Delta G^*/RT$ against $f(X, T)$ are linear with a negative slope equal to $2\sigma l_c^0/RT$ (see fig. 3). In principle, the homopolymer critical thickness value $l_c^0$ can be obtained from isothermal crystallization experiments (crystal thickness measurements required) by using

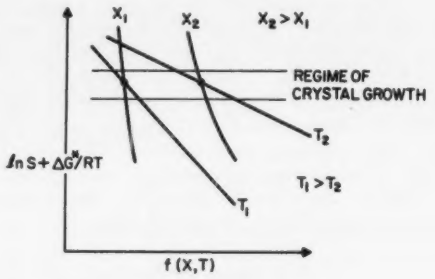


FIGURE 3. *A schematic for the variation of the theoretical nucleation rate with temperature and composition.*

The line labeled $X_1$ indicates how the nucleation rate might vary when quenching a copolymer with composition $X_1$ from a high to low temperature. Most of the crystallization will occur over a narrow range of temperature of average temperature $T_1$. A second copolymer with composition $X_2$ ($X_2 > X_1$) will crystallize during similar quenching with an average temperature $T_2$ which is less than $T_1$.

eqs (13) or (18); thus, the surface free energy parameter $\sigma$ can be determined from eq (19b) by measuring isothermal growth (nucleation) rates. The other surface free energy parameter $\sigma_e$ is obtained, of course, from the relation

$$l_c^0 = 2\sigma_e/\Delta G^0 = 2\sigma_e T_m^0/\Delta H(T_m^0)(T_m^0 - T). \tag{20}$$

If we ignore for the moment the presence of $\Delta G^*$ in eq (19), then two copolymers, one with comonomer concentration $X_1$ and the other with a higher concentration $X_2$, will grow at approximately the same rate if $T_m^0(X_1) - T_1 = T_m^0(X_2) - T_2$; that is, $S(X_1, T_1) \simeq S(X_2, T_2)$ at equal undercoolings. Since $X_2 > X_1$, $T_m^0(X_2) < T_m^0(X_1)$ by eq (2b) and, therefore, $T_2 < T_1$. To obtain the same crystallization rates as $X$ increases requires lower absolute temperatures.

Now the temperature coefficient of $\Delta G^*$ is negative ($S$ decreases with decreasing $T$) and the *effect of diffusional transport is to lower even farther the temperature* ($T_2$) *required to obtain equal growth rates.* Usually a WLF type of free energy is employed for $\Delta G^*$:

$$\Delta G_{WLF}^*/RT = C_1/(C_2 + T - T_g) \tag{21}$$

where $C_1$ and $C_2$ are positive constants and $T_g$ is the glass transition temperature of the polymer [8, 9].

Experimentally, it has been observed that the crystal thickness of tetrafluoroethylene and hexafluoropropylene random copolymers [3] as well as other random copolymers [11, 12] tends to decrease as comonomer concentration $X$ increases in apparent contradiction to the results of section 3.1. However, some of these copolymer crystals were prepared under rapid cooling

conditions (quenching of thin films of melt in ice water [13]) or at uniform cooling rates. During cooling most of the crystal growth will occur over a small temperature interval; say the average temperature in this interval is $T_1$ for a copolymer of concentration $X_1$. If a second copolymer of higher concentration $X_2$ is quenched in the same way, then the average temperature $T_2$ of the temperature interval where most crystal growth occurs will be lower than $T_1$ for reasons discussed above (see fig. 3). In the absence of diffusional transport effects, the two copolymers would crystallize approximately at the same effective undercooling and thus, we might expect crystal thicknesses to be independent of comonomer concentration. However, the transport term tends to reduce $T_2$ causing the effective undercooling of the second sample of higher concentration $X_2$ to be greater than the first. Higher effective undercoolings would cause a decrease in lamellar thickness.

The argument that the transport term $\Delta G^*_{WLF}$ causes the effective undercooling for equal growth rates to *increase* as the co-unit concentration $X$ *increases* assumes that $T_g$ is independent of $X$. What is the situation if $T_g$ varies with $X$? If $T_g$ *increases* with $X$ the argument is strengthened; if $T_g$ *decreases* with $X$, a more careful analysis is required to determine whether or not the argument is valid. In the appendix such an analysis is carried out and the conditions for which the argument is still valid are defined.

For the tetrafluoroethylene-hexafluoropropylene random copolymers, annealing studies [14] have shown that the rate of annealing is determined by the undercooling $(T^0_m(X) - T_{\text{anneal}})$; i.e., the crystal thickness of copolymers with different concentrations will thicken approximately at the same rate at equal undercoolings. The rate of annealing decreases exponentially as $(T^0_m(X) - T_{\text{anneal}})$ increases. Thus, if diffusional transport increases the effective undercooling at which crystal growth occurs, as has been argued, then the contribution that crystal thickening makes to the observed crystal thickness decreases as $X$ increases.

In summary for experiments where the copolymer is quenched or cooled at a uniform rate, diffusional transport effects can cause the effective undercooling at which crystallization occurs to increase as the noncrystallizable co-unit concentration $X$ increases. Higher undercoolings cause both terms in eq (10) for the observed crystal thickness to decrease with increasing $X$.

## 4. Conclusions

The main conclusions of this theoretical study are summarized below:

(1) Both the inclusion and exclusion models predict a depression of the crystalline melting point. For the inclusion model the melting point depression is caused by a defective heat of fusion that accompanies the crystallization, whereas for the exclusion model, the depression is caused by the fact that preferential ordering of the copolymer chains is required for crystallization which raises the entropy of fusion. However, careful crystallinity studies combined with calorimetric determinations of heats of fusion can ascertain which model is more appropriate for a given random copolymer system.

(2) The kinetically determined, isothermal lamella thickness is predicted to increase while the growth rate decreases with increasing concentration $X$ of the noncrystallizable comonomer. Flory's equilibrium theory for the exclusion model also predicts that the crystal thickness increases with $X$ and thus, both theories are qualitatively equivalent in this respect. This aspect of the theory has yet to be tested experimentally.

(3) Qualitatively, the crystal thickness is predicted to decrease with increasing $X$ when the copolymers are crystallized by quenching or cooling at a uniform rate. This is in accord with existing experimental evidence.

(4) The surface free energy parameters $\sigma_e$ and $\sigma$ can be determined from isothermal crystallization experiments by measuring crystal growth rates and thicknesses as a function of copolymer composition. This method is unlike the usual method employed for homopolymer crystal growth studies where temperature is a variable.

(5) The kinetic theory of crystallization formulated herein is applicable, in principle, to any model. Both inclusion and exclusion models or any intermediate model will depress the equilibrium melting point $T^0_m$ of the homopolymer to some new equilibrium value $T^0_m(X)$. Since the kinetics of crystallization ultimately depend on thermodynamic quantities, in particular $T^0_m$ and $T^0_m(X)$, all models will qualitatively affect the kinetics in the same manner. The fundamental quantity which enters the kinetic theory is

$$(T^0_m - T^0_m(X))/(T^0_m(X) - T)$$

For the inclusion model this quantity depends on composition $(X)$ in a specific way and is defined as $f(X, T)$ in this paper. However, it has been shown that for low concentrations of the noncrystallizable co-unit, both inclusion and exclusion models yield equivalent expressions for $T^0_m(X)$ [see eqs (2b) and (6)]. It seems reasonable, therefore, to conjecture that in the limit of low concentrations the functional form of $f(X, T)$ is correct for all molecular models of the crystalline state.

## 5. Appendix. Variations in $\Delta G^*_{WLF}$ With Composition and Temperature

In the main text it was argued that diffusional transport effects can result in higher effective undercoolings for copolymers of higher concentration $(X)$ when quenching on cooling at a uniform rate. The argument assumes that $T_g$ either is unaffected or increases as $X$ increases. If $\partial T_g/\partial X$ is negative the argument must be qualified. For this purpose the variations in $\Delta G^*_{WLF}/RT$ with respect to composition and temperature are calculated below.

Let $Z \equiv \Delta G^*_{WLF}/RT$, then from eq. (21), we have



496-895 OL - 73 - 4

$$\left|\frac{\partial \ln Z}{\partial T}\right| = \frac{1}{C_2 + T - T_g}$$

and

$$\left|\frac{\partial \ln Z}{\partial X}\right| = \frac{\partial T_g/\partial X}{C_2 + T - T_g}.$$

If $\partial T_g/\partial X$ is negative the argument will be valid if the change in $Z$ between the two crystallization temperatures, $T_1 - T_2 = T_m^0(X_1) - T_m^0(X_2)$, exceeds the change in $Z$ with concentration. To a first approximation this condition can be expressed as

$$\left|\frac{\partial \ln Z}{\partial T}\right| [T_m^0(X_1) - T_m^0(X_2)] > \left|\frac{\partial \ln Z}{\partial X}\right| [X_2 - X_1]$$

or

$$-\frac{\partial T_g}{\partial X} < \frac{T_m^0(X_1) - T_m^0(X_2)}{X_2 - X_1}.$$

From eq (2b), we have

$$-\frac{\partial T_g}{\partial X} < A T_m^0.$$

For example, $A = 1.4$ and $T_m^0 = 612$ K for the tetrafluoroethylene-hexafluoropropylene random copolymers and thus, the argument is valid if $T_g$ decreases at a rate less than 8 K for a 1 percent change in composition.

The authors thank J. S. Weeks for his helpful suggestions and critical reading of the manuscript. Preliminary efforts in the direction of this work were reported previously to the American Physical Society [15].

## 6. References and Notes

[1] Flory, P. J., Trans. Faraday Soc. **51**, 848 (1955).
[2] Eby, R. K., and Sanchez, I. C., Bull. Amer. Phys. Soc. **16**, 367 (1971).
[3] Eby, R. K., J. Appl. Phys. **34**, 2442 (1963).
[4] Colson, J. P., and Eby, R. K., J. Appl. Phys. **37**, 3511 (1966).
[5] Sanchez, I. C., and DiMarzio, E. A., Macromolecules **4**, 677 (1971).
[6] Robertson, R. E., Macromolecules **2**, 250 (1969).
[7] Gornick, F., and Hoffman, J. D., Ind. Eng. Chem. **58**, 41 (1966).
[8] Hoffman, J. D., and Weeks, J. J., J. Chem. Phys. **37**, 1723 (1962).
[9] Hoffman, J. D., SPE Transactions **4**, 315 (1964).
[10] Sanchez, I. C., and DiMarzio, E. A., J. Chem. Phys. **55**, 893 (1971).
[11] Hendus, H., Ergeb. Exakt, Naturw. **31**, 331 (1959).
[12] Sella, C., Compt. Rend. **248**, 1819 (1959).
[13] Bolz, L. H., and Eby, R. K., J. Res. Nat. Bur. Stand. (U.S.), 69A, (Phys. and Chem.), No. 5, 481–486 (Sept.–Oct. 1965).
[14] Sanchez, I. C., Colson, J. P., and Eby, R. K., J. Appl. Phys. **44**, Oct. (1973).
[15] Eby, R. K., Bull Amer. Phys. Soc. **10**, 355 (1965).

(Paper 77A3–774)

JOURNAL OF RESEARCH of the National Bureau of Standards—A. Physics and Chemistry
Vol. 77A, No. 3, May–June 1973

# Theory of Disclinations: III. Continuous and Discrete Disclinations in Isotropic Elasticity

**Roland deWit**

**Institute for Materials Research, National Bureau of Standards, Washington, D.C. 20234**

**(February 22, 1973)**

A general theory of stationary disclinations is developed for a linearly elastic, infinitely extended, homogeneous, isotropic body. It is shown to be a special case of the anisotropic theory. Integral expressions are derived for the total displacement, elastic strain and bend-twist, and stress. Both continuous distributions and discrete lines are treated.

Key words: Burgers vector; continuum mechanics; defect; disclination; dislocation; distortion; Green's tensor; incompatibility; plasticity; strain.

## Contents

| | Page |
|---|---|
| 1. Introduction | 359 |
| 2. Isotropy | 360 |
| 3. Review of incompatible theory | 360 |
| 3.1. The plastic strain problem | 360 |
| 3.2. Application: The point defect | 361 |
| 3.3. The incompatibility problem | 362 |
| 4. Review of dislocation theory | 362 |
| 4.1. Continuous distribution of dislocations | 362 |
| 4.2. The discrete dislocation line | 364 |
| 5. Continuous distribution of defects | 364 |
| 6. The discrete defect line | 366 |
| 7. Summary | 367 |
| 8. References | 368 |

## 1. Introduction

In a previous paper [2][1] we have developed the general theory of stationary disclinations in a linearly elastic, infinitely extended, homogeneous, *anisotropic* body. In the present paper we wish to specialize some of those results to the case of an *isotropic* material.

The purpose for this is three-fold. First, for many special applications of the general theory, the isotropic calculations can be carried through analytically; therefore it is convenient to have the isotropic formulas. Second, it will be easier to compare the present results with those in the general lietature; many of the latter have been derived independently with isotropy assumed a priori. Third, when the relation between isotropic and anisotropic theory is clearly revealed, it is often possible to adapt isotropic techniques to anisotropic problems; this has often been successful, and the literature on isotropy is vastly greater than that on anisotropy.

The general approach in this paper is to develop the isotropic theory *ab initio* and show its correspondence to the anisotropic results at many convenient and illustrative points.

In section 2 we give the isotropic forms of certain key relations, i.e., the elastic constants, Green's tensor, and the incompatibility source tensor.

In section 3 we review incompatible elasticity theory without specifying the nature of the defects. We first solve the plastic strain problem which gives the integral expression for the total displacement, which is useful for all the rest of defect theory. We illustrate the result by Eshelby's simplest model of a point defect. Second, we solve the incompatibility problem, which gives the state quantity of elastic strain as an integral over the incompatibility tensor.

[1] Figures in brackets indicate the literature references at the end of this paper.

In section 4 we review classical dislocation theory.

In section 5 we develop the theory of a continuous distribution of defects. Integral expressions are derived for the basic elastic fields (i.e., strain and bend-twist) and the stress. The expressions for these state quantities are given in terms of the defect densities, i.e., the dislocation and disclination densities.

In section 6 we specialize to the discrete defect line. We give the total displacement as a surface integral, and the basic elastic fields and stress as line integrals.

In this paper we shall freely refer to the results of two previous papers [1, 2], which will be denoted as I and II.

## 2. Isotropy

For an isotropic material the elastic constants $C_{ijkl}$ reduce to only two independent constants. In terms of the modulus of rigidity $G$ and Poisson's ratio $\nu$ we can express them as follows [3]:

$$C_{ijkl}=2G\left(\delta_{ik}\delta_{jl}+\frac{\nu}{1-2\nu}\delta_{ij}\delta_{kl}\right)_{(ij)}, \tag{2.1}$$

where $\delta_{ij}$ is the Kronecker delta, and the symbol $(ij)$ indicates that the quantity in parentheses is symmetrized with respect to $i$ and $j$. We have used Cartesian coordinates for simplicity.

For isotropy it is also possible to give the explicit expression of Green's tensor, as follows [3]:

$$G_{jn}(\mathbf{r})=\frac{1}{8\pi G}\left(\delta_{jn}r_{,qq}-\frac{1}{2(1-\nu)}r_{,jn}\right), \tag{2.2}$$

where $r$ is the radius vector, and the comma indicates differentiation. The combination $C_{ijkl}G_{jn,i}$ occurs extensively throughout II. From (2.1–2) we find that it reduces to

$$C_{ijkl}G_{jn,i}(\mathbf{r})=\frac{1}{8\pi}\left(\delta_{ln}r_{,kqq}+\delta_{kn}r_{,lqq}-\frac{1}{1-\nu}r_{,kln}+\frac{\nu}{1-\nu}\delta_{kl}r_{,nqq}\right). \tag{2.3}$$

Another quantity that occurs in II is the incompatibility source tensor, defined by (II4.25)[2]

$$I_{mnpq}(\mathbf{r})=\frac{1}{4\pi}\int\epsilon_{pmk}\epsilon_{qsl}C_{ijkl}G_{jn,i's'}(\mathbf{r}')\,R^{-1}\,dV'_{(mn)}, \tag{2.4}$$

where $\epsilon_{pmk}$ is the permutation symbol and $R$ is the magnitude of the vector $\mathbf{R}=\mathbf{r}-\mathbf{r}'$. From (2.3) this reduces for isotropy to

$$I_{mnpq}(\mathbf{r})=\frac{1}{32\pi^2}\int\epsilon_{pmk}\epsilon_{qsl}\left(\delta_{ln}r'_{,i'i'k's'}+\frac{\nu}{1-\nu}\delta_{kl}r'_{,i'i'n's'}\right)R^{-1}\,dV'_{(mn)}, \tag{2.5}$$

where we have used the antisymmetry or skewsymmetry of $\epsilon_{qsl}$. From the integral

$$\int r'_{,i'i'}R^{-1}\,dV'=2\int(r'R)^{-1}\,dV'=-4\pi r \tag{2.6}$$

this reduces by partial integration to

$$I_{mnpq}(\mathbf{r})=-\frac{1}{8\pi}\epsilon_{pmk}\epsilon_{qsl}\left(\delta_{ln}r_{,ks}+\frac{\nu}{1-\nu}\delta_{kl}r_{,ns}\right)_{(mn)}. \tag{2.7}$$

Finally by (II4.26) this reduces to

$$I_{mnpq}(\mathbf{r})=-\frac{1}{8\pi}\left[\delta_{mq}\delta_{np}r_{,kk}-\delta_{mn}\delta_{pq}r_{,kk}+\delta_{mn}r_{,pq}-\delta_{np}r_{,mq}+\frac{1}{1-\nu}(\delta_{pq}r_{,mn}-\delta_{mq}r_{,np})\right]_{(mn)}. \tag{2.8}$$

The specializations of this section will reduce all the results of II to isotropy, as we shall see. Throughout the paper repeated indices are summed according to the Einstein summation convention. This convention also applies between primed and unprimed indices, as in (2.4).

## 3. Review of Incompatible Theory

In this section we shall give the formal solution of two problems, which can be posed without specifying the nature of the defects involved, i.e., the plastic strain problem and the incompatibility problem.

### 3.1. The Plastic Strain Problem

Given an infinitely extended homogeneous isotropic body with the plastic strain $e^P_{ij}$ given as a prescribed function of space. We seek to find the resulting displacement $u^T_i$ throughout the body.

We solve this problem by a method similar to that of section II2.[3] The equilibrium equation for the stress $\sigma_{ij}$ is (II2.1)

$$\sigma_{ij,i}=0. \tag{3.1}$$

For the isotropic case Hooke's law (II2.2) reduces by (2.1) to

$$\sigma_{ij}=2G\left(e_{ij}+\frac{\nu}{1-2\nu}\delta_{ij}\,e\right), \tag{3.2}$$

where we have written $e$ for dilatation, or trace of the elastic strain $e_{ij}$, i.e., $e=e_{ii}$. The total strain is defined in terms of the total displacement (II2.4) and consists of an elastic and a plastic part (II2.5)

$$e^T_{ij}\equiv u^T_{(j,i)}=e_{ij}+e^P_{ij}. \tag{3.3}$$

The above relations (3.1–3) are conveniently combined into the expression (c.f. II2.6)

[2] The symbol (II4.25) is eq (4.25) in ref. [2].

[3] Section II2 is Section 2 in ref. [2].

$$u^T_{i,jj} + \frac{1}{1-2\nu}\, u^T_{j,ij} = 2e^P_{ij,j} + \frac{2\nu}{1-2\nu}\, e^P_{,i}. \tag{3.4}$$

This is the set of partial differential equations we have to solve for $u^T_i$ when $e^P_{ij}$ is given. The most straightforward method of attack is to reduce (3.4) to a biharmonic equation. First we take the derivative of (3.4) with respect to $x_i$ to obtain

$$\frac{1-\nu}{1-2\nu}\, u^T_{i,ijj} = e^P_{ij,ij} + \frac{\nu}{1-2\nu}\, e^P_{,ii}. \tag{3.5}$$

Next, we take the Laplacian operator of (3.4) and find

$$u^T_{i,jjkk} + \frac{1}{1-2\nu}\, u^T_{j,ijkk} = 2e^P_{ij,jkk} + \frac{2\nu}{1-2\nu}\, e^P_{,ijj}. \tag{3.6}$$

Combining (3.5–6) we have

$$u^T_{i,jjkk} = 2e^P_{ij,jkk} - \frac{1}{1-\nu}\, e^P_{jk,ijk} + \frac{\nu}{1-\nu}\, e^P_{,ijj}. \tag{3.7}$$

To integrate this equation we shall use the following relation

$$(8\pi)^{-1} r_{,jjkk} + \delta(\mathbf{r}) = 0, \tag{3.8}$$

where $\delta(\mathbf{r})$ is the three-dimensional Dirac delta function, defined in Appendix IIB. One interesting way to derive this relation is by substituting (2.3) into (II2.7). This shows that (3.8) is the isotropic equivalent of the defining equation for Green's function.

The solution of our problem now follows easily

$$\begin{aligned}
u^T_i(\mathbf{r}) &= \int \delta(\mathbf{R})\, u^T_i(\mathbf{r}')\, dV' \\
&= -\frac{1}{8\pi} \int R_{,jjkk}\, u^T_i(\mathbf{r}')\, dV' \\
&= -\frac{1}{8\pi} \int R\, u^T_{i,j'j'k'k'}(\mathbf{r}')\, dV' \\
&= -\frac{1}{8\pi} \int R \left[ 2e^P_{ij,j'k'k'}(\mathbf{r}') - \frac{1}{1-\nu}\, e^P_{jk,i'j'k'}(\mathbf{r}') \right. \\
&\quad \left. + \frac{\nu}{1-\nu}\, e^P_{,i'j'j'}(\mathbf{r}') \right] dV' \\
&= \frac{1}{8\pi} \int \left[ 2R_{,jkk}\, e^P_{ij}(\mathbf{r}') - \frac{1}{1-\nu}\, R_{,ijk}\, e^P_{jk}(\mathbf{r}') \right. \\
&\quad \left. + \frac{\nu}{1-\nu}\, R_{,ijj}\, e^P(\mathbf{r}') \right] dV',
\end{aligned} \tag{3.9}$$

where the integrations are taken over all space. In the above derivation the first equality follows from the property of the delta function (IIB3), the second equality from (3.8), the third by partial integrations, the fourth from (3.7), and the fifth again by partial integrations. In the above partial integrations the surface integrals at infinity vanish. For this to happen the following two conditions must be satisfied: the boundary condition for the total displacement is that $u^T_i(\mathbf{r}) \to 0$ as $r \to \infty$; and the condition on the prescribed plastic strain is that $e^P_{ij}(\mathbf{r})$ approaches zero faster than $r^{-1}$ as $r \to \infty$. This last condition also insures that the integral (3.9) is finite. It is easily shown that (3.9) also follows by substituting (2.3) into (II2.15), verifying the consistency between isotropic and anisotropic theory. For the case that $e^P_{ij}$ is constant within a bounded volume and vanishes outside this volume, (3.9) immediately reduces to Eshelby's result [4]. The total distortion is easily obtained from (3.9)

$$\begin{aligned}
\beta^T_{ij}(\mathbf{r}) &= u^T_{j,i}(\mathbf{r}) \\
&= -\frac{1}{8\pi} \int \left[ 2R_{,ikll}\, e^P_{jk}(\mathbf{r}') - \frac{1}{1-\nu}\, R_{,ijkl}\, e^P_{kl}(\mathbf{r}') \right. \\
&\quad \left. + \frac{\nu}{1-\nu}\, R_{,ijkk}\, e^P(\mathbf{r}') \right] dV'.
\end{aligned} \tag{3.10}$$

The equations of this section will form the basis of the expressions for the fields of the more specific defects treated in subsequent sections.

Eshelby pointed out that the field of a defect can also be simulated by a fictitious distribution of body force. For the isotropic case it is obtained by substituting (2.1) into (II2.16). So the defect described by $e^P_{ij}$ is simulated by the fictitious body force

$$-f_j = -2G\left( e^P_{ij,i} + \frac{\nu}{1-2\nu}\, e^P_{,j} \right). \tag{3.11}$$

### 3.2. Application: The Point Defect

It will be instructive to consider a simple application of the relations (3.9) and (3.11). Eshelby [5] regards the discrete point dilatation as the simplest elastic model of a point defect. In our formulation this is easily given by the expression

$$e^P_{ij}(\mathbf{r}) = \frac{1}{3}\, \Delta V\, \delta_{ij}\, \delta(\mathbf{r}), \tag{3.12}$$

where $\Delta V$ is a constant which represents the plastic volume change. Then we find for (3.9)

$$u^T_i(\mathbf{r}) = c x_i / r^3, \tag{3.13}$$

where $c$ is the "strength" of the point defect:

$$c = \frac{1+\nu}{1-\nu}\, \frac{\Delta V}{12\pi} \tag{3.14}$$

From (3.11) we find that this point defect can be simulated by the fictitious body force

$$-f_j = -\Delta V K \delta_{,j}(\mathbf{r}), \tag{3.15}$$

where $K$ is the bulk modulus

$$K = \frac{1+\nu}{1-2\nu}\frac{2G}{3}. \tag{3.16}$$

These results agree with Eshelby, who elaborates this problem further.

In view of section II3.3 the plastic distortion $\beta^P_{ij}$ can be regarded as equivalent to a dislocation loop density $\gamma_{ij}$ (II3.34). Hence eq (3.12) shows that the point defect can be represented by a set of three equal discrete prismatic loops at right angles. This then is an example showing that a point defect can be represented by a discrete defect loop density.

Equation (3.15) furthermore shows that the point defect can also be simulated by a set of three equal fictitious discrete double forces at right angles.

### 3.3. The Incompatibility Problem

The incompatibility tensor $\eta_{ij}$ is given as a prescribed function of space. To find the resulting elastic strain $e_{ij}$ throughout the body.

We solve this problem by exploiting the concept of plastic strain. If the plastic strain field $e^P_{ij}$ is given, then the symmetric incompatibility tensor is defined by (II4.11)

$$\eta_{ij} \equiv \epsilon_{ikl}\,\epsilon_{jmn}\,e^P_{ln,km} \tag{3.17}$$

and satisfies the continuity condition (II4.13)

$$\eta_{ij,i} = 0. \tag{3.18}$$

The expression (3.17) can be expanded by (II4.26) into

$$\eta_{ij} = -e^P_{ij,kk} - e^P_{,ij} + e^P_{jk,ik} + e^P_{ik,jk} + \delta_{ij}\,(e^P_{,ll} - e^P_{kl,kl}). \tag{3.19}$$

From this we derive the two results

$$\eta = e^P_{,ll} - e^P_{kl,kl}, \tag{3.20}$$

$$\eta_{ij} - \delta_{ij}\,\eta = -e^P_{ij,kk} - e^P_{,ij} + e^P_{jk,ik} + e^P_{ik,jk}. \tag{3.21}$$

The solution of our problem now follows easily:

$$\begin{aligned} e_{ij}(\mathbf{r}) &= -\frac{1}{8\pi}\int\Big[R_{,ll}\,(e^P_{jk,i'k'} + e^P_{ik,j'k'}) \\ &\quad -\frac{1}{1-\nu}R_{,ij}\,e^P_{kl,k'l'} + \frac{\nu}{1-\nu}R_{,kk}\,e^P_{,i'j'}\Big]dV' \\ &\quad -e^P_{ij}(\mathbf{r}) \\ &= -\frac{1}{8\pi}\int\Big[R_{,ll}\,(\eta_{ij} - \delta_{ij}\,\eta + e^P_{ij,k'k'} + e^P_{,i'j'}) \\ &\quad +\frac{1}{1-\nu}R_{,ij}\,(\eta - e^P_{,l'l'}) + \frac{\nu}{1-\nu}R_{,kk}\,e^P_{,i'j'}\Big]dV' \\ &\quad -e^P_{ij}(\mathbf{r}) \\ &= -\frac{1}{8\pi}\int\Big[R_{,kk}\,\eta_{ij}(\mathbf{r}') \\ &\quad +\Big(\frac{R_{,ij}}{1-\nu} - \delta_{ij}\,R_{,kk}\Big)\,\eta(\mathbf{r}')\Big]\,dV'. \end{aligned} \tag{3.22}$$

Here the first equality follows from (3.3), (3.10), and some partial integrations, the second equality from (3.20–21), and the third by partial integrations, (3.8), and cancellations. It is easily shown that (3.22) also follows by substituting (2.8) into (II4.31), and using (3.18). In the latter calculation it will be noted that the terms in (2.8) containing $r_{,p}$ and $r_{,q}$ make no contribution to the integral. This shows that the precise form of (2.8) is somewhat indeterminate.

We see that the elastic strain $e_{ij}$ is a state quantity, because it is given entirely in terms of an integral over the incompatibility $\eta_{ij}$, which represents a defect distribution, and is therefore itself also a state quantity. By a state quantity we mean a quantity that can be measured experimentally without any knowledge of former states of the body.

## 4. Review of Dislocation Theory

### 4.1. Continuous Distribution of Dislocations

In this section we give a formal solution to the following problem: The plastic distortion $\beta^P_{ij}$, or the dislocation density $\alpha_{in}$, is given as a prescribed function of space. To find the resulting elastic distortion $\beta_{ij}$.

We solve this problem basically by using the solution for the displacement found in section 3.1. We also derive expressions for the strain, dilatation, stress, and rotation. The dislocation density is defined by (II3.4)

$$\alpha_{in} \equiv -\epsilon_{ikl}\,\beta^P_{ln,k} \tag{4.1}$$

and satisifies the continuity condition (II3.6)

$$\alpha_{in,i} = 0. \tag{4.2}$$

Instead of the dislocation density it is sometimes convenient to use the contortion (I5.11b)

$$K_{lk} = \frac{1}{2}\,\delta_{kl}\,\alpha - \alpha_{kl}. \tag{4.3}$$

The total distortion is defined in terms of the total displacement and for dislocations only consists of an elastic and plastic part (II3.9)

$$\beta^T_{ij} \equiv u^T_{j,i} = \beta_{ij} + \beta^P_{ij}. \tag{4.4}$$

Once the elastic distortion is found, the elastic strain and rotation easily follow from (II3.13–14)

$$e_{ij}=\beta_{(ij)}, \tag{4.5}$$

$$\omega_k=\frac{1}{2}\epsilon_{ijk}\beta_{ij}. \tag{4.6}$$

To solve our problem we recall that the plastic strain is the symmetric part of the plastic distortion (II3.2)

$$e^P_{ij}=\beta^P_{(ij)}, \tag{4.7}$$

and therefore we find the total displacement in terms of the plastic distortion from (3.9)

$$u^T_i(\mathbf{r})=-\frac{1}{8\pi}\int\left[R_{,jjk}\beta^P_{ik}(\mathbf{r}')+R_{,jkk}\beta^P_{ji}(\mathbf{r}')\right.$$
$$\left.-\frac{1}{1-\nu}R_{,ijk}\beta^P_{jk}(\mathbf{r}')+\frac{\nu}{1-\nu}R_{,ijj}\beta^P(\mathbf{r}')\right]dV'. \tag{4.8}$$

By (4.4) it is then simple to express the elastic distortion in terms of the plastic distortion, which solves the first part of our problem. Next, we want to find the expression in terms of the dislocation density:

$$\begin{aligned}\beta_{ij}(\mathbf{r})&=-\frac{1}{8\pi}\int\left[R_{,lnn}\beta^P_{jl,i'}+R_{,knn}\beta^P_{kj,i'}\right.\\&\quad\left.-\frac{1}{1-\nu}R_{,jkl}\beta^P_{kl,i'}+\frac{\nu}{1-\nu}R_{,jnn}\beta^P_{,i'}\right]dV'-\beta^P_{ij}(\mathbf{r})\\&=\frac{1}{8\pi}\int\left[R_{,lnn}(\epsilon_{ijk}\alpha_{kl}-\beta^P_{il,j'})\right.\\&\quad+R_{,knn}(\epsilon_{ikl}\alpha_{lj}-\beta^P_{ij,k'})\\&\quad-\frac{1}{1-\nu}R_{,jkl}(\epsilon_{ikm}\alpha_{ml}-\beta^P_{il,k'})\\&\quad\left.+\frac{\nu}{1-\nu}R_{,jnn}(\epsilon_{ilm}\alpha_{ml}-\beta^P_{il,l'})\right]dV'-\beta^P_{ij}(\mathbf{r})\\&=\frac{1}{8\pi}\int\left[R_{,lnn}\epsilon_{ijk}\alpha_{kl}(\mathbf{r}')+R_{,knn}\epsilon_{ikl}\alpha_{lj}(\mathbf{r})\right.\\&\quad-\frac{1}{1-\nu}R_{,jkl}\epsilon_{ikm}\alpha_{ml}(\mathbf{r}')\\&\quad\left.+\frac{\nu}{1-\nu}R_{,jnn}\epsilon_{ilm}\alpha_{ml}(\mathbf{r}')\right]dV'.\end{aligned} \tag{4.9}$$

Here the first equality follows from (4.4), (4.8) and some partial integrations, the second from (4.1), and the third by partial integrations, (3.8), and some cancellations. This result could also have been obtained more directly by substituting (2.3) into (II3.17).

There is another convenient form for (4.9), which is obtained by using the identities

$$\epsilon_{ikl}\alpha_{lj}\equiv\epsilon_{ikl}\alpha_{jl}-\epsilon_{klm}\delta_{ij}\alpha_{ml}+\epsilon_{ilm}\delta_{jk}\alpha_{ml}, \tag{4.10}$$

$$R_{,t}\epsilon_{ikm}\equiv R_{,m}\epsilon_{ikl}-R_{,i}\epsilon_{klm}+R_{,k}\epsilon_{ilm}. \tag{4.11}$$

With these we find

$$\beta_{ij}(\mathbf{r})=\frac{1}{8\pi}\int[R_{,lnn}\epsilon_{ijk}\alpha_{kl}(\mathbf{r}')+R_{,knn}\epsilon_{ikl}\alpha_{jl}(\mathbf{r}')$$
$$-R_{,knn}\epsilon_{klm}\delta_{ij}\alpha_{ml}(\mathbf{r}')$$
$$+\frac{1}{1-\nu}(R_{,ijk}\epsilon_{klm}-R_{,jkm}\epsilon_{ikl})\alpha_{ml}(\mathbf{r}')]\,dV'. \tag{4.12}$$

The last term in this expression vanishes by a partial integration and (4.2). So we obtain finally

$$\beta_{ij}(\mathbf{r})=\frac{1}{8\pi}\int\left[R_{,lnn}\epsilon_{ijk}\alpha_{kl}(\mathbf{r}')+R_{,knn}\epsilon_{ikl}\alpha_{jl}(\mathbf{r}')\right.$$
$$\left.+\left(\frac{R_{,ijk}}{1-\nu}-\delta_{ij}R_{,knn}\right)\epsilon_{klm}\alpha_{ml}(\mathbf{r}')\right]dV'. \tag{4.13}$$

This is the elastic distortion due to the prescribed dislocation distribution $\alpha_{in}$. It is a state quantity. By (4.1) we can also express it in terms of the plastic distortion. This then solves the originally posed problem.

Next, we find the elastic strain from (4.5) and (4.13)

$$e_{ij}(\mathbf{r})=\frac{1}{8\pi}\int\left[R_{,knn}(\epsilon_{ikl}\alpha_{jl}(\mathbf{r}'))_{(ij)}\right.$$
$$\left.+\left(\frac{R_{,ijk}}{1-\nu}-\delta_{ij}R_{,knn}\right)\epsilon_{klm}\alpha_{ml}(\mathbf{r}')\right]dV'. \tag{4.14}$$

From this we find the dilatation

$$e(\mathbf{r})=-\frac{1-2\nu}{1-\nu}\frac{1}{8\pi}\int R_{,knn}\epsilon_{klm}\alpha_{ml}(\mathbf{r}')\,dV',$$

and the stress by (3.2)

$$\sigma_{ij}(\mathbf{r})=\frac{G}{4\pi}\int\left[R_{,knn}(\epsilon_{ikl}\alpha_{jl}(\mathbf{r}'))_{(ij)}\right.$$
$$\left.+\frac{1}{1-\nu}(R_{,ijk}-\delta_{ij}R_{,knn})\epsilon_{klm}\alpha_{ml}(\mathbf{r}')\right]dV'. \tag{4.16}$$

The rotation is found from (4.6) and (4.13)

$$\omega_k(\mathbf{r})=\frac{1}{8\pi}\int\left[R_{,lnn}\alpha_{kl}(\mathbf{r}')-\frac{1}{2}R_{,knn}\alpha(\mathbf{r}')\right.$$
$$\left.+\frac{1}{2}R_{,jnn}\alpha_{jk}(\mathbf{r}')\right]dV'. \tag{4.17}$$

The last term in this expression vanishes by a partial integration and (4.2). So we have

$$\omega_k(\mathbf{r}) = \frac{1}{8\pi}\int\left[R_{,lnn}\alpha_{kl}(\mathbf{r}') - \frac{1}{2}R_{,knn}\alpha(\mathbf{r}')\right]dV'$$

$$= -\frac{1}{8\pi}\int R_{,lnn}K_{lk}(\mathbf{r}')\,dV', \tag{4.18}$$

where the last equality follows from (4.3).

To summarize, in this section we have derived explicit integral expressions for the most useful elastic fields (distortion, strain, dilatation, stress, and rotation) of a continuous distribution of dislocations in an infinite isotropic body.

### 4.2. The Discrete Dislocation Line

For a discrete dislocation line with Burgers vector $b_j$ along the curve $L$ the plastic distortion has the special form (II3.21)

$$\beta^P_{ij}(\mathbf{r}) = -\delta_i(S)\,b_j, \tag{4.20}$$

where $\delta_i(S)$ is the Dirac delta function for a surface $S$ whose boundary is $L$, defined in Appendix IIB. Therefore we find for the displacement (4.8)

$$u^T_i(\mathbf{r}) = \frac{1}{8\pi}\int_S\Big[R_{,jjk}b_k dS'_i + R_{,jkk}b_i dS'_j$$

$$-\frac{1}{1-\nu}R_{,ijk}b_k dS'_j + \frac{\nu}{1-\nu}R_{,ijj}b_k dS'_k\Big], \tag{4.21}$$

where we have used (IIB9). This expression could also have been obtained directly by substituting (2.3) into (II3.30), as was done in ref. [3]. The same result was also obtained by Kroupa [6, 7].

For the discrete dislocation line the dislocation density is given by (II3.23)

$$\alpha_{in}(\mathbf{r}) = \delta_i(L)\,b_j, \tag{4.22}$$

where $\delta_i(L)$ is the Dirac delta function for the closed curve $L$. We therefore find for the elastic distortion (4.13)

$$\beta_{ij}(\mathbf{r}) = \frac{b_l}{8\pi}\oint_L\Big[R_{,lnn}\epsilon_{ijk}dL'_k + R_{,knn}\epsilon_{ikl}dL'_j$$

$$+\left(\frac{R_{,ijk}}{1-\nu} - \delta_{ij}R_{,knn}\right)\epsilon_{klm}dL'_m\Big], \tag{4.23}$$

where we have used (IIB8). Similarly we find the elastic strain from (4.14) or from (4.23)

$$e_{ij}(\mathbf{r}) = \frac{b_l}{8\pi}\oint_L\Big[R_{,knn}(\epsilon_{ikl}dL'_j)_{(ij)}$$

$$+\left(\frac{R_{,ijk}}{1-\nu} - \delta_{ij}R_{,knn}\right)\epsilon_{klm}dL'_m\Big], \tag{4.24}$$

which agrees with ref. [3]. We find the dilatation from (4.15) or (4.24)

$$e(\mathbf{r}) = -\frac{1-2\nu}{1-\nu}\frac{b_l}{8\pi}\oint_L R_{,knn}\epsilon_{klm}dL'_m, \tag{4.25}$$

and we find the stress from (4.16)

$$\sigma_{ij}(\mathbf{r}) = \frac{Gb_l}{4\pi}\oint_L\Big[R_{,knn}(\epsilon_{ikl}dL'_j)_{(ij)}$$

$$+\frac{1}{1-\nu}(R_{,ijk} - \delta_{ij}R_{,knn})\,\epsilon_{klm}dL'_m\Big], \tag{4.26}$$

which agrees with ref. [3], and has been called the formula of Peach and Koehler. Finally, we find the rotation from (4.18)

$$\omega_k(\mathbf{r}) = \frac{b_l}{8\pi}\oint_L\Big[R_{,lnn}dL'_k - \frac{1}{2}R_{,knn}dL'_l\Big]. \tag{4.27}$$

In this section we have derived explicit closed line integrals for the most useful elastic fields of a discrete dislocation line in an infinite isotropic body. Most of these expressions have already been given before in the literature and proved very valuable for specific calculations and applications of dislocation theory.

## 5. Continuous Distribution of Defects

As in II we shall denote the combination of dislocations and disclinations by the word *defects*. Similarly we shall refer to the strain and bend-twist as the *basic fields*. Further discussion of the basic total, elastic, and plastic fields is given in ref. [10].

In this section we give a formal solution to the following problem: The basic plastic fields $e^P_{ij}$ and $\kappa^P_{ij}$, or the defect densities $\alpha_{in}$ and $\theta_{ij}$, are given as prescribed functions of space. To find the basic elastic fields $e_{ij}$ and $\kappa_{ij}$.

Again, we solve this problem basically by using the solution for the displacement found in section 3.1. In addition we also derive an expression for the stress. If the basic plastic fields are given then the defect densities are defined by (II4.1–2)

$$\alpha_{in} \equiv -\epsilon_{ikl}(e^P_{ln,k} - \epsilon_{jkn}\kappa^P_{lj}), \tag{5.1}$$

$$\theta_{ij} \equiv -\epsilon_{ikl}\kappa^P_{lj,k}, \tag{5.2}$$

which satisfy the continuity conditions (II4.3–4)

$$\alpha_{in,i} + \epsilon_{ijn}\theta_{ij} = 0, \tag{5.3}$$

$$\theta_{ij,i} = 0 \tag{5.4}$$

The conditions (5.3–4) can be combined into

$$\epsilon_{ikl}\alpha_{ml,mk} + \theta_{il,l} = 0. \tag{5.5}$$

The incompatibility (3.17) can also be expressed as (II4.12)

$$\eta_{ij} = -(\epsilon_{jmn}\alpha_{in,m} + \theta_{ij})_{(ij)}. \tag{5.6}$$

Instead of the dislocation density $\alpha_{in}$ it is sometimes convenient to use the contortion which is still defined as before (I6.5b)

$$K_{lk} = \frac{1}{2}\delta_{kl}\alpha - \alpha_{kl}. \tag{5.7}$$

For the disclination density $\theta_{ij}$ it is useful to have the expression

$$\begin{aligned}\theta_{ij} - \delta_{ij}\theta &= -\epsilon_{ikl}\kappa^P_{lj,k} + \delta_{ij}\epsilon_{klm}\kappa^P_{lm,k} \\ &= -\epsilon_{ikl}(\kappa^P_{jl,k} - \kappa^P_{kl,j}),\end{aligned} \tag{5.8}$$

where the second equality follows from the identity (4.10) with $\alpha$ replaced by $\kappa$. The basic total fields are defined in terms of the total displacement and consist of elastic and plastic parts (II4.14–15)

$$e^T_{ij} \equiv u^T_{(j,i)} = e_{ij} + e^P_{ij}, \tag{5.9}$$

$$\kappa^T_{ij} \equiv \omega^T_{j,i} = \kappa_{ij} + \kappa^P_{ij}, \tag{5.10}$$

where the total rotation is defined by

$$\omega^T_k \equiv \frac{1}{2}\epsilon_{ijk}u^T_{j,i}. \tag{5.11}$$

For completeness we also include the expressions for the characteristic vectors, i.e., the total Burgers vector $B_n$ and the Frank vector $\Omega_j$ (II4.5–8):

$$\begin{aligned}B_n &\equiv -\oint_\lambda (e^P_{ln} - \epsilon_{jmn}\kappa^P_{lj}x_m)\, dL_l \\ &= \int_\sigma (\alpha_{in} - \epsilon_{jmn}\theta_{ij}x_m)\, dS_i,\end{aligned} \tag{5.12}$$

$$\begin{aligned}\Omega_j &\equiv -\oint_\lambda \kappa^P_{lj}\, dL_l \\ &= \int_\sigma \theta_{ij} dS_i,\end{aligned} \tag{5.13}$$

where $\lambda$ is a Burgers circuit and $\sigma$ the Burgers surface which spans $\lambda$.

To solve our problem we use the distortion given by (3.10). By some partial integrations and changes in dummy indices we have

$$\begin{aligned}u^T_{j,i}(\mathbf{r}) = -\frac{1}{8\pi}\int\Big[&R_{,lnn}e^P_{jl,i'}(\mathbf{r}') + R_{,knn}e^P_{kj,i'}(\mathbf{r}') \\ &- \frac{1}{1-\nu}R_{,jkl}e^P_{kl,i'}(\mathbf{r}') + \frac{\nu}{1-\nu}R_{,jnn}e^P_{il,i'}(\mathbf{r}')\Big]\, dV'\end{aligned} \tag{5.14}$$

By (5.9–11) it is then simple to express the basic elastic fields in terms of the basic plastic fields, which solves the first part of our problem. Next, we wish to find the expressions in terms of the defect densities. First we find from (5.14)

$$\begin{aligned}u^T_{j,i}(\mathbf{r}) = \frac{1}{8\pi}\int\Big[&R_{,lnn}\{\epsilon_{ijk}(\alpha_{kl} - \kappa^P_{lk}) - e^P_{il,j'} + \epsilon_{ijl}\kappa^P\} \\ &+ R_{,knn}\{\epsilon_{ikl}(\alpha_{lj} - \kappa^P_{jl}) - e^P_{ij,k'} - \epsilon_{ijk}\kappa^P\} \\ &- \frac{1}{1-\nu}R_{,jkl}\{\epsilon_{ikm}(\alpha_{ml} - \kappa^P_{lm}) - e^P_{il,k'} + \epsilon_{ikl}\kappa^P\} \\ &+ \frac{\nu}{1-\nu}R_{,jnn}\{\epsilon_{ilm}(\alpha_{ml} - \kappa^P_{lm}) - e^P_{il,l'}\}\Big]\, dV' \\ = \frac{1}{8\pi}\int\Big[&R_{,lnn}\epsilon_{ijk}(\alpha_{kl} - \kappa^P_{lk}) + R_{,knn}\epsilon_{ikl}\alpha_{ij} \\ &- \frac{1}{1-\nu}R_{,jkl}\epsilon_{ikm}\alpha_{ml} + \frac{\nu}{1-\nu}R_{,jnn}\epsilon_{ilm}\alpha_{ml} \\ &- R_{,nn}\epsilon_{ikl}\kappa^P_{jl,k'} + \frac{1}{1-\nu}R_{,jl}\epsilon_{ikm}\kappa^P_{lm,k'} \\ &- \frac{\nu}{1-\nu}R_{,jnn}\epsilon_{ilm}\kappa^P_{lm}\Big]\, dV' + e^P_{ij}(\mathbf{r}) \\ = \frac{1}{8\pi}\int\Big[&R_{,lnn}\epsilon_{ijk}(\alpha_{kl} - \kappa^P_{lk}) - R_{,knn}\epsilon_{ikl}\alpha_{jl} \\ &- R_{,knn}\epsilon_{klm}\delta_{ij}\alpha_{ml} \\ &+ \frac{1}{1-\nu}(R_{,ijk}\epsilon_{klm} - R_{,jkm}\epsilon_{ikl})\alpha_{ml} \\ &+ R_{,nn}(\theta_{ij} - \delta_{ij}\theta) - \frac{1}{1-\nu}R_{,jl}(\theta_{il} - \delta_{il}\theta)\Big]\, dV' \\ &+ e^P_{ij}(\mathbf{r}) \\ = \frac{1}{8\pi}\int\Big[&R_{,lnn}\epsilon_{ijk}(\alpha_{kl}(\mathbf{r}') - \kappa^P_{lk}(\mathbf{r}')) \\ &+ R_{,knn}\epsilon_{ikl}\alpha_{jl}(\mathbf{r}') \\ &+ \left(\frac{R_{,ijk}}{1-\nu} - \delta_{ij}R_{,knn}\right)\epsilon_{klm}\alpha_{ml}(\mathbf{r}') \\ &+ R_{,nn}\theta_{ij}(\mathbf{r}') + \left(\frac{R_{,ij}}{1-\nu} - \delta_{ij}R_{,nn}\right)\theta(\mathbf{r}')\Big] \\ &+ e^P_{ij}(\mathbf{r}).\end{aligned} \tag{5.15}$$

Here the first equality follows from (5.1), the second from partial integrations, (3.8), and cancellations, the third from (4.10–11), (5.8), partial integrations and

cancellations, and the fourth from partial integrations and (5.5).

From (5.15) we then find the elastic strain by (5.9)

$$e_{ij}(\mathbf{r}) = \frac{1}{8\pi}\int \Big[R_{,knn}(\epsilon_{ikl}\alpha_{jl}(\mathbf{r}'))_{(ij)} + \Big(\frac{R_{,ijk}}{1-\nu} - \delta_{ij}R_{,knn}\Big)\epsilon_{klm}\alpha_{ml}(\mathbf{r}') + R_{,nn}\theta_{(ij)}(\mathbf{r}') + \Big(\frac{R_{,ij}}{1-\nu} - \delta_{ij}R_{,nn}\Big)\theta(\mathbf{r}')\Big]dV'. \quad (5.16)$$

This is the elastic strain due to the prescribed defect distributions $\alpha_{in}$ and $\theta_{ij}$. The result could also have been obtained by substituting (2.3) and (2.8) into (II4.29), using (5.4–5). In the latter calculation it will be noted that the terms in (2.8) containing $r_{,q}$ do not contribute to the integral. We see that $e_{ij}$ is a state quantity because it is given in terms of the defect densities. By (5.1–2) we can also express the elastic strain in terms of the basic plastic fields. So (5.16) solves half of the originally posed problem. We note that when the disclination density vanishes, $\theta_{ij}=0$, (5.16) reduces to (4.14), as expected. There is another way to write (5.16), by doing some partial integrations

$$e_{ij}(\mathbf{r}) = \frac{1}{8\pi}\int \Big[R_{,nn}(\epsilon_{klm}\alpha_{jl,k'}(\mathbf{r}') + \theta_{ij}(\mathbf{r}'))_{(ij)} + \Big(\frac{R_{,ij}}{1-\nu} - \delta_{ij}R_{,nn}\Big)(\epsilon_{kln}\alpha_{ml,k'}(\mathbf{r}') + \theta(\mathbf{r}'))\Big]dV',$$

which agrees with (3.22) by (5.6). This then shows an alternative way of deriving (5.16). Next we find the dilatation from (5.16).

$$e(\mathbf{r}) = -\frac{1-2\nu}{1-\nu}\frac{1}{8\pi}\int [R_{,knn}\epsilon_{klm}\alpha_{ml}(\mathbf{r}') + R_{,nn}\theta(\mathbf{r}')]dV', \quad (5.18)$$

and the stress by (3.2)

$$\sigma_{ij}(\mathbf{r}) = \frac{G}{4\pi}\int \Big[R_{,knn}(\epsilon_{ikl}\alpha_{jl}(\mathbf{r}'))_{(ij)} + \frac{1}{1-\nu}(R_{,ijk} - \delta_{ij}R_{,knn})\epsilon_{klm}\alpha_{ml}(\mathbf{r}') + R_{,nn}\theta_{(ij)}(\mathbf{r}') + \frac{1}{1-\nu}(R_{,ij} - \delta_{ij}R_{,nn})\theta(\mathbf{r}')\Big]dV'. \quad (5.19)$$

To find the elastic bend-twist, we first find the total rotation from (5.11) and (5.15)

$$\omega_k^T(\mathbf{r}) = \frac{1}{8\pi}\int \Big[R_{,lnn}(\alpha_{kl} - \kappa_{lk}^p) - \frac{1}{2}R_{,knn}\alpha + \frac{1}{2}R_{,jnn}\alpha_{jk} + R_{,nn}\epsilon_{ijk}\theta_{ij}\Big]dV'$$

$$= -\frac{1}{8\pi}\int R_{,lnn}[K_{lk}(\mathbf{r}') + \kappa_{lk}^p(\mathbf{r}')]dV', \quad (5.20)$$

where the second equality follows from (5.7), a partial integration, and (5.3). Finally we find the elastic bend-twist

$$\kappa_{ij}(\mathbf{r}) = -\frac{1}{8\pi}\int [R_{,klnn}K_{kj} + R_{,knn}\kappa_{kj,l'}^p]dV' - \kappa_{ij}^p(\mathbf{r})$$

$$= -\frac{1}{8\pi}\int [R_{,klnn}K_{kj} + R_{,knn}(\epsilon_{ikl}\theta_{lj} - \kappa_{lj,k'}^p)]dV' - \kappa_{ij}^p(\mathbf{r})$$

$$= -\frac{1}{8\pi}\int [R_{,klnn}K_{kj}(\mathbf{r}') + R_{,knn}\epsilon_{ikl}\theta_{lj}(\mathbf{r}')]dV'. \quad (5.21)$$

Here the first equality follows from (5.10), (5.20), and a partial integration, the second from (5.2), and the third by a partial integration, (3.8), and a cancellation. This is the elastic bend-twist due to prescribed defect distributions $\alpha_{in}$ and $\theta_{ij}$. The same result can also be obtained by substituting (2.3) into (II4.34), and using (5.3) and (5.5). We see that it is also a state quantity. By (5.1–2) we can also express it in terms of the basic plastic fields. So (5.21) and (5.16) solve the originally posed problem. When the disclination density vanishes, $\theta_{ij}=0$, (5.21) reduces to the derivative of (4.18), as expected.

In this section we have derived explicit integral expressions for the basic elastic fields and the stress of a continuous distribution of defects in an infinite isotropic body. We have seen that when the disclination density vanishes, $\theta_{ij}=0$, the results reduce to these for dislocations in section 4.1. Due to the assumption of isotropy the above integrals are given in terms of the relative radius vector $R$ and its derivatives. Hence those are straightforward integrations for any given distribution of defects. For example, in the next section we shall see how they apply to a discrete defect line.

## 6. The Discrete Defect Line

For a discrete defect line along the curve $L$ the basic plastic fields reduce to the special form (II5.14–15)

$$e_{ln}^p = \beta_{(ln)}^*, \quad (6.1)$$

$$\kappa_{ij}^p = 1/2\epsilon_{jmn}\beta_{mn,l}^* + \phi_{ij}^*, \quad (6.2)$$

where the defect loop densities are defined by (II5.12–13)

$$\beta_{ln}^*(\mathbf{r}) \equiv -\delta_l(S)\{b_n + \epsilon_{jmn}\Omega_j(x_m - x_m^0)\}, \quad (6.3)$$

$$\phi^*_{ij}(\mathbf{r}) \equiv -\delta_l(S)\Omega_j. \tag{6.4}$$

Here $b_n$ and $\Omega_j$ are the characteristic vectors, i.e., the dislocation Burgers vector and the Frank vector, $x^0_m$ is a point thru which the axis of the disclination passes, and $\delta_l(S)$ is the Dirac delta function for a surface $S$ whose boundary is $L$. The defect densities are given by (II5.19–20)

$$\alpha_{in}(\mathbf{r}) = \delta_l(L)\{b_n + \epsilon_{jmn}\Omega_j(x_m - x^0_m)\}, \tag{6.5}$$

$$\theta_{ij}(\mathbf{r}) = \delta_l(L)\Omega_j, \tag{6.6}$$

where $\delta_l(L)$ is the Dirac delta function for the closed curve $L$. The contortion is by (5.7) and (6.5)

$$K_{kj}(\mathbf{r}) = 1/2\delta_{jk}\delta_l(L)\{b_l + \epsilon_{lpq}\Omega_p(x_q - x^0_q)\} - \delta_j(L)\{b_k + \epsilon_{kpq}\Omega_p(x_q - x^0_q)\}. \tag{6.7}$$

The total Burgers vector is (II5.17)

$$B_n = b_n - \epsilon_{jmn}\Omega_j x^0_m, \tag{6.8}$$

and the displacement jump across the surface $S$ is (II5.1, II5.5)

$$[u_n] = B_n + \epsilon_{jmn}\Omega_j x_m = b_n + \epsilon_{jmn}\Omega_j\,(x_m - x^0_m). \tag{6.9}$$

We now find the total displacement from (3.9), (6.1), and (6.3)

$$u^T_i(\mathbf{r}) = \frac{1}{8\pi}\int_S \{b_k + \epsilon_{kmn}\Omega_m\,(x'_n - x^0_n)\} \left[R_{,jjk}dS'_i + R_{,jli}\delta_{ik}dS'_j - \frac{1}{1-\nu}R_{,ijk}dS'_j + \frac{\nu}{1-\nu}R_{,ijj}dS'_k\right], \tag{6.10}$$

where we have used (IIB9). When the disclination vanishes, $\Omega_m = 0$, this equation reduces to (4.21). We find the elastic strain from (5.16) and (6.5–6).

$$e_{ij}(\mathbf{r}) = \frac{1}{8\pi}\oint_L \Big[\{b_l + \epsilon_{lpq}\Omega_p(x'_q - x^0_q)\} \Big\{R_{,knn}\,(\epsilon_{ikl}dL'_j)_{(ij)} + \left(\frac{R_{,ijk}}{1-\nu} - \delta_{ij}R_{,knn}\right)\epsilon_{klm}dL'_m\Big\} + R_{,nn}\,(\Omega_j dL'_i)_{(ij)} + \left(\frac{R_{,ij}}{1-\nu} - \delta_{ij}R_{,nn}\right)\Omega_m dL'_m\Big], \tag{6.11}$$

where we have used (IIB8). Again, for $\Omega_m = 0$, this reduces to (4.24).

The dilatation becomes

$$e(\mathbf{r}) = -\frac{1-2\nu}{1-\nu}\frac{1}{8\pi}\oint_L [\{b_l + \epsilon_{lpq}\Omega_p(x'_q - x^0_q)\} R_{,knn}\epsilon_{klm} + R_{,nn}\Omega_m]dS'_m, \tag{6.12}$$

and the stress becomes

$$\sigma_{ij}(\mathbf{r}) = \frac{1}{8\pi}\oint_L \Big[\{b_l + \epsilon_{lpq}\Omega_p(x'_q - x^0_q)\} \Big\{R_{,knn}(\epsilon_{ikl}dL'_j)_{(ij)} + \frac{1}{1-\nu}\,(R_{,ijk} - \delta_{ij}R_{,knn})\epsilon_{klm}dL'_m\Big\} + R_{,nn}(\Omega_j dL'_i)_{(ij)} + \frac{1}{1-\nu}\,(R_{,ij} - \delta_{ij}R_{,nn})\Omega_m dL'_m\Big]. \tag{6.13}$$

Finally we find the elastic bend-twist from (5.21) and (6.6–7)

$$\kappa_{ij}(\mathbf{r}) = \frac{1}{8\pi}\oint_L \Big[\{b_k + \epsilon_{kpq}\Omega_p(x'_q - x^0_q)\} \Big\{R_{,klnn}dL'_j - \frac{1}{2}\,R_{,jlnn}dL'_k\Big\} - R_{,knn}\epsilon_{ikl}\Omega_j dL'_i\Big]. \tag{6.14}$$

In this section we have derived explicit closed line integrals for the basic elastic fields and the stress of a discrete defect line in an infinite isotropic body. We have seen that when the disclination vanishes, $\Omega_m = 0$, the results reduce to those for a discrete dislocation line in section 4.2. All the above integrals are given in terms of radius vectors. Hence they should be straightforward for given geometries of the discrete defect lines. As in the case of dislocation lines this should make the above expressions useful for the practical application of disclinations.

## 7. Summary

We have specialized previous results derived for anisotropic disclination theory to the special case of isotropy. We have also derived the isotropic theory independently and showed that anisotropic theory reduces to it.

We have given a short review of incompatible theory which serves as the basis of departure for all subsequent applications to defects. We have also reviewed dislocation theory which forms a basis of comparison for defect theory.

For a continuous distribution of defects we have derived the expressions for the state quantities: the basic elastic fields and the stress. These expressions are given in terms of the defect densities, the disclination and the dislocation density, which in turn can be expressed in terms of the basic plastic fields. Next,

we specialized these results to a discrete defect loop. These expressions are given in terms of the characteristic vectors, the total Burgers vector and the Frank vector, as line integrals along the defect line. We have shown explicitly that these results reduce to those for dislocation theory when the disclinations vanish.

The results for the discrete defect line are in a useful form for application to special geometries. In future publications we shall apply them to straight lines [8] and loops [9].

## 8. References


[1] deWit, R., in Fundamental aspects of dislocation theory, Nat. Bur. Stand. (U.S.) Spec. Publ. 317, Vols. 1 and 2 (1970), p. 651. In this paper referred to as I.

[2] deWit, R., J. Res. Nat. Bur. Stand. (U.S.) **77A**, (Phys. and Chem.), No. 1, 49–100 (Jan.–Feb. 1973). In this paper referred to as II.

[3] deWit, R., Sol. State Phys. **10**, 269 (1960).

[4] Eshelby, J. D., Progr. Solid Mech. **II**, 89 (1961).

[5] Eshelby, J. D., Sol. State Phys. **3**, 79 (1956).

[6] Kroupa, F., Czech. J. Phys. **B12**, 191 (1962).

[7] Kroupa, F., in Theory of Crystal Defects, Ed., B. Gruber (Academic Press, N. Y., 1966), p. 275.

[8] deWit, R., Theory of Disclinations IV. Straight Disclinations (to be published).

[9] deWit, R., Theory of Disclinations V. Disclination Loops (to be published).

[10] deWit, R., Continuous Distribution of Disclination Loops, submitted to phys. stat. sol.


(Paper 77A3–775)

JOURNAL OF RESEARCH of the National Bureau of Standards—A. Physics and Chemistry
Vol. 77A, No. 3, May–June 1973

# Compressive Fatigue Coaxing in Composites

**C. A. Berg* and M. Salama****

**Institute for Basic Standards, National Bureau of Standards, Washington, D.C. 20234**

**(December 11, 1972)**

Compressive fatigue experiments on unidirectional fiber reinforced composites, of both fiberglass and graphite fiber, reveal that compressive fatigue damage takes place by crack extension directly transverse to the fibers. It is also found that specimens which are first subjected to a few hundred thousand cycles of compressive fatigue at low stress levels, and then subjected to compressive fatigue at high stress levels, will survive longer at high stress levels than specimens which are placed under high compressive fatigue stresses from the outset. The increase of fatigue life at high compressive stress levels can be quite large; increases of fatigue life by as much as a factor of five were observed. The phenomenon of prolonging fatigue life at high stress levels by first "running in" a specimen at low stress levels is called coaxing, and is directly opposite to the often reported cumulative damage phenomena observed in tensile fatigue of composites. A possible mechanism for coaxing in compressive fatigue of composites is offered, and practical applications of the effect are suggested.

Key words: Coaxing; composites; compressive fatigue; fatigue.

## 1. Introduction

With certain metal alloys it is observed that by fatiguing the alloy first at a low stress level and later at a higher stress level, one may obtain a longer fatigue life at the higher stress level than if one had not first applied the low amplitude fatigue loading [1].[1] In metals the magnitude of this effect, called coaxing, is not large (a 20% increase in fatigue life at high stress is a large coaxing effect), and the mechanisms responsible are not presently understood.

In a study of compressive fatigue of fiber reinforced composites the authors observed very strong coaxing effects (in some cases the fatigue life of the specimen at high stress could be increased by a factor of 5 by first subjecting the specimen to low amplitude fatigue loading). The mechanism of the coaxing effect in fiber reinforced composites appears to derive from differential fatigue cracking rates in the longitudinal and transfibrile directions. This brief paper is offered as a report of the coaxing effects which the authors observed. In addition, certain possible applications of this effect are discussed.

*Professor and Chairman, Dept. of Mechanical Engineering, University of Pittsburgh, Pittsburgh, Pa. Presently Visiting Scientist, Institute for Basic Standards, National Bureau of Standards, Washington, D.C.

**Dept. of Mechanical Engineering, Massachusetts Institute of Technology, Cambridge, Mass.

[1] Figures in brackets indicate literature references at the end of this paper.

## 2. Fatigue Experiments

A set of experiments in which long flat plates (22.8 × 2.54 × 0.280 cm) of unidirectional fiber reinforced plastics were subjected to pure bending fatigue were carried out. The oscillating bending moment was biased in such a way that the specimen was bent in one direction only. Thus, one side of the specimen was subjected to cyclic tension-release loading while the other side was subjected to cyclic compression-release loading. The specimens were oriented so that the fiber direction was parallel to the principal axis of bending stress in the specimen. In different experiments bending was applied about both the minimum (0.280 cm) and maximum (2.54 cm) cross-sectional dimension of the specimens. A typical specimen is shown in the photograph of figure 1. As indicated in the figure, the ends of the specimens were clamped between aluminum blocks, which were in turn held in the (4 point) bending grips of an SF-IU (Sonntag) fatigue testing machine. This machine applies fatigue loads of fixed amplitude. By proper setting of the static load control of the fatigue machine, the biased moment which gave pure tensile fatigue on one side of the specimen and pure compressive fatigue on the other side, was obtained.



496-895 OL - 73 - 5

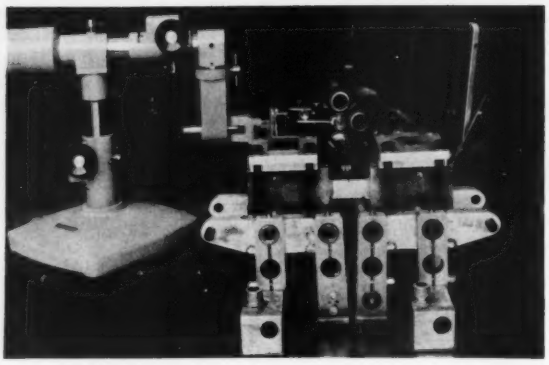

FIGURE 1. *Compressive fatigue experiment in progress.*

## 3. Materials Studied

Two different materials were studied. Unidirectional fiberglass specimens formed by hot pressing of fiberglass-epoxy pre-preg tape were used.[2] The fiber volume fraction of the final specimens was approximately 60 percent. The tensile strength in the fiber direction was $1.1 \times 10^9$ Pa and the elastic modulus in the same direction was $3.26 \times 10^{10}$ Pa.[3] In addition, specimens of unidirectional graphite fiber reinforced epoxy were formed by hot pressing of pre-preg tape.[4] The final fiber volume fraction of these specimens was approximately 62 percent; the tensile strength of the specimens loaded in the fiber direction was $8.3 \times 10^8$ Pa and the elastic modulus in this direction was $1.5 \times 10^{11}$ Pa.

## 4. Observations of Experiments

In each specimen fatigue produced fatigue cracking extending directly across the fibers, and originating on the compressive side of the specimen. A more extensive report of compressive fatigue notch extension has been given by the authors elsewhere [2]. In unnotched fiberglass specimens compressive fatigue cracking originated at the points where the aluminum blocks contacted the edges of the specimens. The crack gradually worked its way along the line of contact between the aluminum grip block and the specimen.[5] Several similar specimens were run to failure under different values of nominal compressive stress. Of course, the nominal bending stress gives only an average measure of the intensity of stress in a specimen suffering fatigue. It is used here only as a parameter to indicate the coaxing effect described in this note. (For a treatment of compressive fatigue which takes into account the character of stress at the tip of the propagating notch see ref. 2.) In addition, a collection of specimens was subjected first to fatigue at low stress levels and then to fatigue at high stress levels. Figure 2 shows

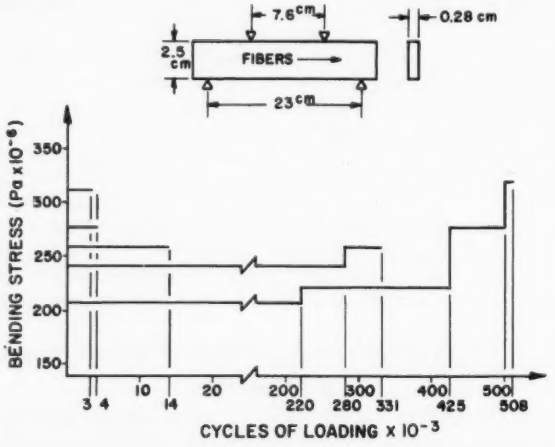


FIGURE 2. *Coaxing of unnotched fiberglass specimens in compressive fatigue (specimens oriented as shown).*

results obtained for a collection of fiberglass specimens. Specimens which were subjected to a nominal bending stress of $314 \times 10^6$ Pa fractured, by the compressive fatigue notch extension described above, after only $3 \times 10^3$ cycles of loading. At a nominal stress of $272 \times 10^6$ Pa the specimen survived only $4 \times 10^3$ cycles of loading, and at $255 \times 10^6$ Pa the specimen survived only $14 \times 10^3$ cycles of loading. However, when a specimen was first subjected to $236 \times 10^6$ Pa for $2.8 \times 10^5$ cycles (no evidence of fracture was observed) and then raised to $256 \times 10^6$ Pa, it survived $5.1 \times 10^4$ additional cycles of loading at the higher stress. Similarly, a specimen first subjected to $204 \times 10^6$ Pa for $2.2 \times 10^5$ cycles of loading, then raised to $216 \times 10^6$ Pa for an additional $2.05 \times 10^5$ cycles of loading, could then be raised to $272 \times 10^6$ Pa for an additional $7.5 \times 10^4$ cycles of loading without any evidence of fracture being

[2] The fiberglass pre-preg was supplied by the 3-M Company, and formed and cured according to the manufacturer's specifications. Certain commercial products and instruments are identified in this paper in order to specify adequately the experimental procedure. In no case does such identification imply recommendation or endorsement by the National Bureau of Standards, nor does it imply that the products or equipment identified are necessarily the best available for the purpose.

[3] The symbol Pa represents the Pascal, the SI unit of stress (1 N/m² or $1.450 \times 10^{-4}$ lbf/in²). Experimental determinations of strength and modulus were carried out by the authors prior to the fatigue study reported here.

[4] The graphite fiber pre-preg tape was supplied by Whittaker Corp., and consisted of Whittaker Modmor II graphite fiber in B staged 4617 epoxy resin. Forming and curing were carried out according to the manufacturer's recommendations.

[5] While there is nothing surprising in the fact that fatigue damage originated at the contact line between the specimen and the grip, the propagation of a crack directly across the fibers under compression was somewhat unexpected, and the increased fatigue life of specimens subjected to prior fatigue loading was most surprising.

observable, and then raised to $310 \times 10^6$ for yet another $8 \times 10^3$ cycles of loading before fracture terminated the test.

Fatigue experiments conducted with graphite fiber reinforced specimens also showed coaxing. Figure 3

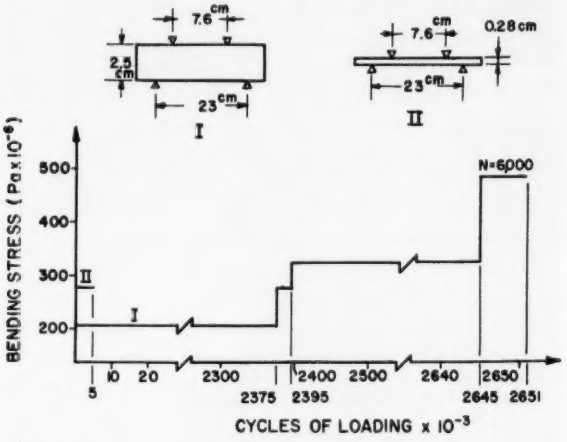


FIGURE 3. *Coaxing of unnotched graphite fiber epoxy specimens in compressive fatigue.*

shows data obtained from pure bending experiments.[6] A nominal compressive stress of $272 \times 10^6$ Pa produces a failure of the specimen after $5 \times 10^3$ cycles of loading. However, a specimen which is first subjected to $204 \times 10^6$ Pa stress for $2.375 \times 10^6$ cycles can then be subjected to $275 \times 10^6$ Pa for an additional $2.0 \times 10^4$ cycles without any evidence of fracture being observable. The specimen can then be subjected to $325 \times 10^6$ Pa for $2.5 \times 10^5$ cycles without observable fatigue damage, and finally can be subjected to $475 \times 10^6$ Pa for an additional $6 \times 10^3$ cycles of loading before failure of the specimen occurs. The failure of these specimens also occurred by extension of compressive fatigue cracking which originated at the line of contact of the aluminum grip block on the specimen surface.

Finally, prenotched graphite fiber reinforced specimens were studied. The specimens were bent as indicated in figure 4, and were initially notched to depth of 0.254 cm on the side of the specimen subjected to cyclic compression. The notch was cut with a fragment of a diamond impregnated resin, and the notch width at its tip was $7.60 \times 10^{-3}$ cm; for details of the

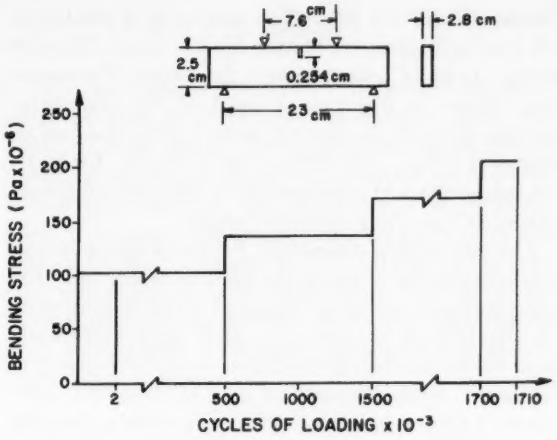


FIGURE 4. *Coaxing of prenotched graphite fiber reinforced epoxy specimens in compressive fatigue.*

notch configuration see reference 2. Freshly notched specimens were found to survive a nominal bending stress of $204 \times 10^6$ Pa for only $2 \times 10^3$ cycles of loading. Compressive fatigue crack extension began immediately upon application of the load; when the crack had progressed approximately two thirds the way across the specimen, tensile fracture occurred on the opposite side of the specimen and terminated the experiment. However, a notched specimen subjected first to a nominal bending stress of $104 \times 10^6$ Pa showed no notch extension for $5 \times 10^5$ cycles of loading. The specimen was then subjected to $147 \times 10^6$ Pa for an additional $10^6$ cycles of loading without showing any notch extension, and then to $172 \times 10^6$ Pa for yet an additional $2 \times 10^5$ cycles without any notch extension occurring. Finally the specimen was subjected to $204 \times 10^6$ Pa, and survived for an additional $10^4$ cycles of loading before failure. As in the specimens described above, failure occurred via compressive fatigue crack extension from the original notch. Data gathered from experiments with prenotched graphite fiber specimens are shown in figure 4.

## 5. Summary of Observations

In each of the cases cited above, it was found that initial fatigue loading at a low stress level in some way conditioned the specimen to survive fatigue loading at a high stress level for a greater period than if the low stress fatigue had not been applied. Typically, coaxing extended the fatigue life at high stress level by a factor of 5 (e.g. in fig. 4 a virgin specimen survives $2 \times 10^3$ cycles whereas a specimen first subjected to low stress

[6] In the experiments with graphite uncoaxed specimens were bent about the minor axis of the cross section of the specimen and coaxed specimens were bent about the major axis of the cross section, as is indicated in figure 3. This should have no effect on coaxing unless gradients of stress—rather than stress itself—are significant in activating damage. This is viewed as unlikely, but for the sake of completeness the difference in the bending of uncoaxed (II, fig. 3) and coaxed (I, fig. 3) specimens is noted.

fatigue will survive $10^4$ cycles; also in fig. 2 similar extensions of high stress fatigue life are seen). The very strong "coaxing" effect seen in the record of compressive fatigue is just the opposite of the cumulative damage phenomena observed in tensile fatigue, and interpreted by (e.g.), Broutman and Sahu [3]. Evidently the mechanisms of compressive fatigue are of different character than those of tensile fatigue.

The mechanism responsible for compressive fatigue crack extension is micro buckling of fibers [2]. The material near the line of contact of the aluminum block on the fiberglass specimens underwent sufficiently large lateral displacements that it could be observed to "breathe" under illumination by a stroboscopic lamp. Figure 5 shows a drawing of the deformation observed

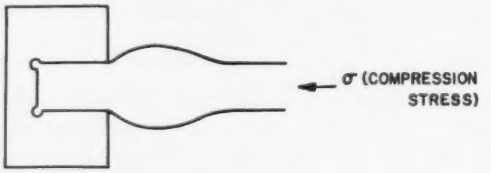


FIGURE 5. *Bulging at contact between grip block and specimen, as observed during fatigue experiments. (Scale exaggerated for purposes of illustration.)*

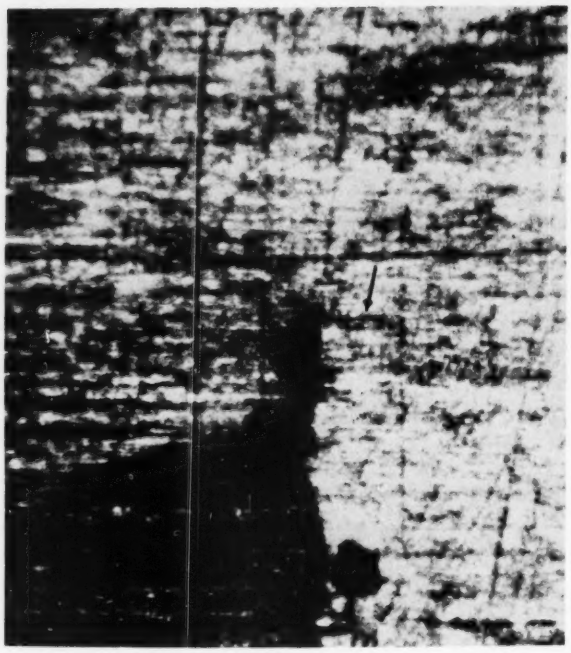

FIGURE 6. *Longitudinal notch extension (arrow) from compressive fatigue crack which underwent complete arrest.*

at the juncture of the specimen and grip block as the specimen was subjected to compression. The bulging of the specimen against the hard surface of the grip evidently served to nucleate the fatigue crack which ultimately caused failure. Bulging of the unnotched graphite fiber specimen probably also occurred, but the deflections of the specimen were too small to observe with the low power microscope used in these experiments.

In another set of experiments [2] it was found that under certain conditions compressive fatigue notches would propagate and then arrest. Figure 6 shows a photograph of a crack which has arrested after propagation. Note that a longitudinal crack has extended from the tip of the main fatigue crack. The authors observed that once longitudinal crack extension occurred at the tip of a transfibrile notch it was extremely difficult to restart fatigue cracking in the transfibrile direction. This suggests a mechanism which may be responsible for the strong coaxing effect observed in the experiments reported above. The authors suggest that at a given stress level there are different rates of fatigue crack nucleation and subsequent crack extension transverse to the fiber direction, and parallel to the fiber direction (i.e., in the matrix). At low stress levels fatigue cracking transverse to the fiber direction may take place very slowly, or might actually cease; since the main mechanism of transfibrile compressive crack extension is micro buckling it would be reasonable to expect that at stress levels below some threshold value no crack nucleation or extension will occur; such thresholds have been observed previously [2]. However, it may still be possible to extend fatigue cracking through the matrix at low stress levels (say, levels below the threshold for transfibrile cracking). In this case, compressive fatigue at low stress levels would result in longitudinal crack extension from the tips of any small notches or flaw sites which might serve as potential nuclei for transfibrile cracking. If the longitudinal cracking is permitted to extend sufficiently far, the entire flaw structure in the material will be changed; all of the flaws which could have served as nuclei of transfibrile cracking will have been converted to T shaped cracks from which only further longitudinal cracking, which is relatively harmless, may proceed. In this case, in order to produce transfibrile fatigue cracking new flaw sites would have to be created, which in most materials takes a long time. The authors propose that different fatigue crack nucleation and extension rates in the fibrile and transfibrile direction is responsible for the coaxing effect shown in figures 2, 3 and 4.

Figure 6 shows a crack tip in a graphite fiber reinforced specimen, which was subjected to tensile fatigue after having first been subjected to compressive fatigue which produced the transfibrile crack [2]. The longitudinal crack extension shown in the figure occurred within the first few cycles of tensile loading; such longitudinal cracking from transfibrile notches under tension is highly typical of unidirectional composites. When the specimen of figure 6 was subjected to compressive fatigue it behaved essentially as an unnotched specimen (longitudinal cracking had obviously removed the main transfibrile notch from the specimen). This observation, and the observations of coaxing of unidirectional composites given above suggest two things which may be of substantial practical importance in structural applications of fiber composites, including composites of more complex configuration. First, if a composite part is to be subjected primarily to compressive loading in service then compressive fatigue by transfibrile cracking should be recognized as one of the most important damage mechanisms which might operate on the part. Second, it would seem to be possible to extend the compressive fatigue life of the part. One way to do this would be to run the part in at low stress level before placing it in service (i.e., to use the coaxing effect of figs. 2, 3, 4). Another way to achieve the same effect would be, where it is possible, to remove the part from service at regular intervals and to subject it to a tensile loading (i.e., to use the "crack removal" phenomenon of fig. 6). Combinations of tensile load excursions and low level fatigue loading might also provide possibilities for extending compressive fatigue life of composite structures.

## 6. Closure

This report has been based on observations of only a small number of specimens and the data have been taken only on specific coaxing histories (the coaxing curves of figs. 2, 3, 4). While the data here are in no way statistically complete, the phenomenon of coaxing is clear. It is the authors' hope in offering the present note that others may be alerted to the existence of the coaxing phenomenon, and that those to whom the phenomenon may be of value or interest, will undertake their own studies to develop sufficient data to meet their own needs.

---

Financial support of the Celanese Research Company, Summit, N.J. through a grant in aid to Massachusetts Institute of Technology is gratefully acknowledged. Preparation of this report was supported by the National Bureau of Standards.

## 7. References

[1] Sinclair, G. M., Corten, H. T., Dolan, T. J., Effect of Surface Finish on the Fatigue Strength of Titanium Alloys R C 130B and T i 140A, Trans. ASME **79**, 89-96 (1957).

[2] Berg, C., and Salama, M., Compressive Fatigue in Fiber Reinforced Materials, to appear in Journal of Materials (ASTM), June 1972.

[3] Broutman, L., and Sahu, S., A New Theory to Predict Cumulative Fatigue Damage in Fiber Reinforced Plastics, Proc. Second ASTM Conference on Composite Materials, Testing and Design (April 20-22, 1971) in press (1972).

(Paper 77A3–776)

JOURNAL OF RESEARCH of the National Bureau of Standards — A. Physics and Chemistry
Vol. 77A, No. 3, May-June 1973

# Publications of the National Bureau of Standards*

## Citations with Selected Abstracts

SP260-44. **Standard reference materials: Preparation and use of superconductive fixed point devices, SRM 767,** J. F. Schooley, R. J. Soulen, Jr., and G. A. Evans, Jr., Nat. Bur. Stand. (U.S.), Spec. Publ. 260-44, 35 pages (Dec. 1972) 75 cents, SD Catalog No. C13.10:260-44.

Key words: Aluminum; cadmium; cryogenics; indium; lead; magnetic susceptibility; superconductive transition temperature; superconductivity; thermometric fixed points; zinc.

The preparation, testing, and use of SRM 767 devices are described. These devices incorporate samples of lead, indium, aluminum, zinc, and cadmium within a mutual inductance coil pair. These elements become superconductive at temperatures near 7.2, 3.4, 1.2, 0.85 and 0.5 K, respectively, and the transition midpoints, when attained by observing the sample magnetic susceptibilities in negligible small magnetic fields, provide thermometric reference points which are reproducible to ± 1 mK.

SP304, Revised October 1972. **The modernized metric system—The international system of units (SI),** Nat. Bur. Stand. (U.S.), Spec. Publ. 304, 1 chart (Oct. 1972) 55 cents, SD Catalog No. C13.10:304.

Key words: International system of units; measurement systems; metric system; modernized metric system; SI; weights and measures.

The seven base units of the modernized metric system (also called the International System of Units, abbreviated SI), two supplementary units, several derived units, a meter stick and, for purposes of comparison, a yardstick are all shown on this four-color wall chart. Additional information shown includes a brief statement on the nature of the modernized metric system and its use in the United States, a table permitting conversion of commonly used units from SI to customary units and vice versa, and a table listing the names and symbols of decimal multiples and submultiples used with SI units.

SP304A, Revised October 1972. **Brief history of measurement systems with a chart of the modernized metric system,** Nat. Bur. Stand. (U.S.), Spec. Publ. 304A, 4 pages (Oct. 1972) 25 cents, SD Catalog No. C13.10:304A.

Key words: International system of units; measurement systems; metric system; modernized metric system; SI; weights and measures.

The Modernized Metric System (also called the International System of Units) is made up of seven base units, two supplementary units, and many derived units. The chart describes this entire system, including details about the standards for each base unit and information on how the system is used.

The reverse side of the chart contains a brief history of measurement systems. The need for measurement began with primitive man, who used parts of his body and his natural surroundings for measurement standards and measuring instruments. As societies evolved, weights and measures became more complex. Two systems became predominant: the English system, rooted in the history and tradition of England; and the metric system, a scientifically based system using decimal notation. The metric system, with its inherent decimal advantages, gained widespread acceptance and is now the official measurement system in nearly all countries of the world.

SP357. **The mechanisms of pyrolysis, oxidation, and burning of organic materials.** Based on Invited Papers and Discussion, 4th Materials Research Symposium held at the National Bureau of Standards, Gaithersburg, Md., Oct. 26-29, 1970, L. A. Wall, Editor, Nat. Bur. Stand. (U.S.), Spec. Publ. 357, 199 pages (June 1972) $3.25, SD Catalog No. C13.10:357.

Key words: Burning; hydrocarbons; organic materials; oxidation; polymers; pyrolysis.

A symposium on The Mechanisms of Pyrolysis, Oxidation, and Burning of Organic Materials was held at the National Bureau of Standards in October 1970. This volume contains the nineteen papers presented and much of the discussion which followed.

These papers review and discuss the current status of kinetic studies on the reactions of organic materials in both gas and condensed phases. The topics covered include: pyrolysis of hydrocarbons, pyrolysis of polymers, oxidation of polymers, oxidation of organic compounds, burning of organic compounds and burning of polymers. Particular emphasis is placed on the elucidation of the mechanisms of reaction in terms of free radicals or other transient species and physical effects.

SP367. **National Bureau of Standards Brochure, 1972,** W. E. Small, Editor, Nat. Bur. Stand. (U.S.), Spec. Publ. 367, 67 pages (Dec. 1972) $1.00, SD Catalog No. C13.10:367.

Key words: National Bureau of Standards; organization; overview; program descriptions.

This publication presents an in-depth look at the National Bureau of Standards. An overview of the Bureau's history, programs, and major contributions preceeds individual chapters detailing the programs of each of the four NBS Institutes: Institute for Basic Standards; Institute for Materials Research; Institute for Applied Technology; and Institute for Computer Sciences and Technology. Supersedes NBS Miscellaneous Publication 282 and Special Publication 360.

SP376. **Ruler: 15 cm/6 in, with metric-customary units and equivalents,** Nat. Bur. Stand. (U.S.), Spec. Publ. 376, Both Sides (Dec. 1972) 10 cents, SD Catalog No. C13.10:376.

**Publications with prices and SD Catalog numbers may be purchased directly from the Superintendent of Documents, U.S. Government Printing Office, Washington, D.C. 20402 (foreign: one-fourth additional). Microfiche copies are available from the National Technical Information Service (NTIS), Springfield, Va. 22151. Reprints from outside journals and the NBS Journal of Research may often be obtained directly from the authors.*

TN361. (Revised October 1972). **Liquid densities of oxygen, nitrogen, argon, and parahydrogen,** H. M. Roder, R. D. McCarty, and V. J. Johnson, Nat. Bur. Stand. (U.S.), Tech. Note 361 (Revised), 181 pages (Oct. 1972) $1.25, SD Catalog No. C13.46:361 (Revised).

Key words: Argon; compressed liquid; density; graphs; liquid; nitrogen; oxygen; parahydrogen; pressure; saturated liquid; tables; temperatures; uncertainties; volume; volume correction factor.

Tables of pressure, volume, density and temperature for the saturated liquid and for compressed liquid states from the triple point to the critical point, of oxygen, nitrogen, argon, and parahydrogen are presented. The table entries of temperature are in Kelvin and Rankine, table entries in pressure are in atmospheres and psia. Volumes or densities are given in several different units, and density ratios or "volume correction factors" are tabulated for each entry. Estimates of the uncertainty for the tabulated data are given. The tables and graphs were prepared in the style and in the units preferred by users. They are intended as source for both technician and engineer. Revises and updates NBS Technical Note 361, issued January 31, 1968.

TN622. **Thermophysical properties of helium-4 from 4 to 3000 R with pressures to 15,000 psia,** R. D. McCarty, Nat. Bur. Stand. (U.S.), Tech. Note 622, 141 pages (Sept. 1972) $1.25, SD Catalog No. C13.46:622.

Key words: Density; dielectric constant; enthalpy; entropy; equation of state; fixed points; heat transfer coefficients; helium 4; index of refraction; Joule-Thomson coefficient; lambda line; latent heat; melting point; Prandtl number; specific heats; speed of sound; surface tension; thermal conductivity; thermal diffusivity; vapor pressure; viscosity; volume.

Tables of thermophysical properties of helium 4 are presented for temperatures from 4 to 3000 Rankine for pressures to 15,000 psia. The tables include entropy, enthalpy, internal energy, density, volume, speed of sound, specific heat, thermal conductivity, viscosity, thermal diffusivity, Prandtl number and the dielectric constant for 74 isobars. Also included in the isobaric tables are quantities of special utility in heat transfer calculations: $(\partial P/\partial V)_T$, $(\partial P/\partial T)_\rho$, $V(\partial H/\partial V)_P$, $V(\partial P/\partial U)_V$, $-V(\partial P/\partial V)_T$, $1/V(\partial V/\partial T)_P$.

In addition to the isobaric tables, tables for the saturated vapor and liquid are given which include all of the above properties, plus the surface tension. Tables for the $P\rho T$ of the freezing liquid, $P\rho T$ of the lambda line, index of refraction and the derived Joule-Thomson inversion curve are also presented.

TN625. **Computer programs for thermodynamic and transport properties of hydrogen (Tabcode-II),** H. M. Roder, R. D. McCarty, and W. J. Hall, Nat. Bur. Stand. (U.S.), Tech. Note 625, 226 pages (Oct. 1972) $1.75, SD Catalog No. 13.46:625.

Key words: Computer programs; density; enthalpy; entropy; heat capacity at constant pressure; heat capacity at constant volume; heat capacity ratio; heat transfer coefficient; hydrogen; pressure; saturation boundary; temperature; thermal conductivity; velocity of sound; viscosity.

The thermodynamic and transport properties of para and equilibrium hydrogen have been programmed into a series of computer routines. Input variables are the pair's pressure-temperature and pressure-enthalpy. The programs cover the range from 1 to 5000 psia (34 $MN/m^2$) with temperatures from the triple point to 6000 °R (3300 K) or enthalpies from − 130 Btu/lb (− 623 J/mol) to 25,000 Btu/lb (117000 J/mol). Output variables are enthalpy or temperature, density, entropy, thermal conductivity, viscosity, velocity of sound, heat capacity at constant pressure, heat capacity at constant volume, the heat capacity ratio, and a heat transfer parameter. Property values on the liquid and vapor boundaries are conveniently obtained through two small routines. The programs achieve high speed by using linear interpolation in a grid of precomputed points which define the surface of the property returned. The maximum errors arising from the linear interpolation are shown on individual deviation plots for each combination of variables. Error estimates for the sources of data are similarly displayed.

TN626. **The generation of an accurate and uniform time scale with calibrations and prediction,** K. Yoshimura, Nat. Bur. Stand. (U.S.), Tech. Note 626, 64 pages (Nov. 1972) 60 cents, SD Catalog No. C13.46:626.

Key words: Accurate and uniform time scale; Allan variance; dispersion of time scale; ensemble time (error); prediction interval; primary standard and clocks.

We express a predicted time interval (or frequency) of a single clock as a weighted sum of frequency data obtained by calibrations against a primary standard, and derive a matrix equation for the optium weighting coefficients (called the optimum filter response function) involving the Allan variances. Two approaches are used. One of the approaches turns out to be a generalization of Barnes' approach in his 1966 IEEE paper.

We solve the matrix equation to get the optimum filter response functions for white noise frequency modulation (FM), flicker noise FM and linear combinations of them. Other important time dispersive mechanisms exist in practice but are not considered here. We obtain the result that the mean square time prediction error would increase as elapsed time $t^2$ for the case without intermediate calibrations.

We obtain the result that with a small number of good clocks one can construct a time scale whose accuracy is limited by the accuracy of a primary standard. We show that, over a long time range, linear prediction algorithms based on frequency calibrations with a primary standard give a time scale of much better accuracy and stability than when intermittent calibrations are not used, and that (at least for statistically identical clocks), *no advantage is gained* by using the time scale itself as a "primary standard" for intermediate calibrations.

TN631. **Thermophysical properties of helium-4 from 2 to 1500 K with pressures to 1000 atmospheres,** R. D. McCarty, Nat. Bur. Stand. (U.S.), Tech. Note 631, 161 pages (Nov. 1972) $1.25, SD Catalog No. C13.46:631.

Key words: Density; dielectric constant; enthalpy; entropy; equation of state; fixed points; heat transfer coefficients; helium 4; index of refraction; Joule-Thomson coefficient; lambda line; latent heat; melting point; Prandtl number; specific heats; speed of sound; surface tension; thermal conductivity; thermal diffusivity; vapor pressure; viscosity; volume.

Tables of thermophysical properties of helium 4 are presented for temperatures from 2 to 1500 K for pressures to 1000 atmospheres. The tables include, entropy, enthalpy, internal energy, density, volume, speed of sound, specific heat, thermal conductivity, viscosity, thermal diffusivity, Prandtl number and the dielectric constant for 62 isobars. Also included in the isobaric tables are quantities of special utility in heat transfer calculations: $(\partial P/\partial V)_T$, $(\partial P/\partial T)_\rho$, $V(\partial H/\partial V)_P$, $V(\partial P/\partial U)_V$, $-V(\partial P/\partial V)_T$, $1/V(\partial V/\partial T)_P$.

In addition to the isobaric tables, tables for the saturated vapor and liquid are given which include all of the above properties, plus the surface tension. Tables for the $P\rho T$ of the freezing liquid, $P\rho T$ of the lambda line, index of refraction and the derived Joule-Thomson inversion curve are also presented. A computer program to calculate the various properties is also available. Inquiries should be addressed to the National Bureau of Standards, Cryogenic Data Center, Boulder, Colo. 80302.

TN710-6. **Building research translation: Ventilation air inlets for dwellings,** M. Croiset and H. Bizebard, Nat. Bur. Stand. (U.S.), Tech. Note 710-6, 62 pages (Jan. 1973) $1.00, SD Catalog No. C13.46:710-6.

Key words: Air inlet; discomfort index; draft; outside wall; ventilation; wind.

Preliminary tests have shown the existence of a "discomfort index," a function firstly of the difference between the temperature in the room and the temperature of the air current and, secondly of the speed of the air stream. The permissible limit for this index has been fixed at 2 °C, at least in that part of the room situated more than 20 cm from the outside walls and less than 2 meters in height.

Systematic artificial tests have resulted in satisfactory solutions being found for the air inlets into the outside walls.

—An elongated aperture placed above a radiator and fitted with a deflector so that cold air entering the room mingles with the ascending warm air current.

—An aperture located behind a convector heater so that the same result is achieved as in the case of the radiator.

—A row of apertures located along the heated ceiling placed so that entering air is diffused into the warm air before reaching the occupied zone.

Some calculations aimed at determining the orders of magnitude of the necessary sections and the possible force of the air current in a high wind, have revealed the need for a manual or an automatic regulator where a wall is exposed to wind.

TN743. **Methods of measurement for semiconductor materials, process control, and devices. Quarterly report April 1 to June 30, 1972,** W. M. Bullis, Editor, Nat. Bur. Stand. (U.S.), Tech. Note 743, 57 pages (Dec. 1972) $1.00, SD Catalog No. C13.46:743.

TN749. **The flammable fabrics program 1971. U.S. Department of Commerce report of activities under the Flammable Fabrics Act 1971,** Nat. Bur. Stand. (U.S.), Tech. Note 749, 92 pages (Dec. 1972) $1.50, SD Catalog No. C13.46:749.

Key words: Annual report to Congress; blankets; children's sleepwear; flammability; flammability reduction; mattresses; research; sampling plans; standards; test development; upholstered furniture.

This Annual Report to the Congress, required by the Flammable Fabrics Act, covers calendar year 1971. Specific flammability standards outputs were standards for children's sleepwear in sizes 0 through 6X, a proposed standard for mattresses, and a finding of possible need for amendment of the children's sleepwear standard to add sampling plans for the periodic testing by manufacturers of subject garments and materials. Research included studies, in-house and under contract, on subjects such as the contribution of floor covering systems to fire spread along building corridors and the parameters related to the burning of cotton/polyester blends and of multilayer fabrics. Studies of the feasibility of reducing flammability included the effects of treatments on combustion products and the effects of heavy metal ions on flammability. Test development, in addition to that basic to the standards developments already mentioned, included work on a blanket test, an upholstered furniture test, and on a general apparel test. A series of formal training sessions was initiated to supplement the continuing informal training, presentations, etc. Extensive cooperation was carried out with HEW, the public, industry, and voluntary standards groups.

TN750. **Matches and lighters in flammable fabric incidents: The magnitude of the problem,** J. A. Slater, B. Buchbinder, and H. Tovey, Nat. Bur. Stand. (U.S.), Tech. Note 750, 27 pages (Dec. 1972) 55 cents, SD Catalog No. C13.46:750.

Key words: Fabric fires; FFACTS; fire injuries; flammable fabrics; ignition sources; lighters; matches.

Matches and lighters were a major factor in the 1,838 flammable fabric incidents studied for which ignition sources are known. They accounted for 430, almost one-fourth, of the ignitions and led to 375 injuries, of which 57 were fatal. Children and the elderly were the groups most frequently involved in fires started by matches or lighters. Nearly half the incidents involved children under age 11, and two-thirds of these were children under age 6. Forty-four of the 57 fatalities were children under age 11 or adults over 65. The highest fatality rate, 57 percent, was experienced by persons over age 65. The home was the predominant location of fires involving matches and lighters. Of the fabric items ignited by matches and lighters, garments were first to ignite four times as frequently as nonapparel items such as furnishings and bedding. Over one-third of the incidents involved intermediary materials in the ignition sequence. Match ignitions outnumbered lighter ignitions by 6 to 1. Among the 430 match and lighter incidents, fires involving children were overwhelmingly the result of playing with matches and lighters, whereas for persons over age 16, smoking was the single most prevalent activity at the time of ignition.

*The following are outside publications by the NBS staff, as soon after issuance as practical. For completeness, earlier references not previously reported may be included from time to time. The five-digit number at the beginning of each entry is used for record keeping only and should not be used when requesting reprints or other information.*

13035. Barbrow, L. E., **The mass-weight dilemma,** *Sci. Teacher* **39,** No. 7, 4 (Oct. 1972).

Key words: Free fall; gravity; mass vs. weight; weight; weightlessness; weight vs. mass.

The impending changeover to the metric system has again given prominence to the confusion that exists regarding what the term "weight" signifies. This term for centuries has been used synonymously with mass but it has also been used to signify many other concepts, each related to the force of gravitational attraction in some way. The multiplicity of meanings of the term "weight" has created a dilemma the suggested resolution of which is the use of the term exclusively as being synonymous with mass and to use the term force when discussing any of the concepts related to gravity. How to handle the popularized concept of "weightlessness" is dealt with separately.

13036. Ledbetter, H. M., Wayman, C. M., **On $\beta$ AuCd martensites,** *Met. Trans.* **3,** No. 9, 2349-2356 (Sept. 1972).

Key words: Crystallography; crystal structure/alloys; gold-cadmium alloys; phase transformations/solid state; x-ray-diffraction crystallography.

The martensites which form from $\beta$ AuCd alloys have been studied by x-ray diffraction using both powder and single-crystal techniques. Alloys containing 46.8 to 51.0 at.pct Cd were examined. Besides the parent phase $\beta$ only two other phases were observed: $\beta'$ and $\beta''$. A new unit cell is proposed for $\beta''$ which has 18 atoms and trigonal-hexagonal point symmetry. All previous $\beta''$ crystal structure proposals are reviewed critically. The relationship of the $\beta''$ crystal structure to the $\beta$-to-$\beta''$ martensitic transition is discussed.

13037. Kirby, R. K., Hahn, T. A., Rothrock, B. D., **Thermal expansion,** Section 4f in *American Institute of Physics Handbook, Third Ed.*, pp. 4-119—4-142 (1972).

Key words: Alloys; compounds; elements; Grüneisen's constant; linear thermal expansion; liquids.

New and revised tables for the 3d edition of the AIP Handbook. These tables are: Table TE-1, Linear Thermal Expansion and Coeffi-

cients of Linear Thermal Expansion of Chemical Elements; Table TE-2, Coefficients of Linear Thermal Expansion of Materials at Low Temperatures; Table TE-3, Linear Thermal Expansion and Coefficients of Linear Thermal Expansion of Some Compounds and Alloys; Table TE-4, Thermal Expansion of Liquids; and Table TE-5, Constants in Grüneisen's Equation for Thermal Expansion (eight of the elements have been deleted from this table as it appeared in the 2d edition because the information is not consistent with the data given in TE-1).

13038. Reed, R. P., **Aluminium. 2. A review of deformation properties of high purity aluminium and dilute aluminium alloys,** *Cryogenics* **12,** No. 4, 259-291 (Aug. 1972).

Key words: Elastic properties; high-purity aluminium; lattice defects; mechanical properties; recovery; strengthening.

The elastic and plastic deformation behaviour of high-purity aluminium and of dilute aluminium alloys is reviewed. Reliable property data, including elastic moduli, elastic coefficients, tensile, creep, fatigue, hardness, and impact are presented. Single crystal tensile results are discussed. Rather comprehensive reference lists, containing publications of the past 20 years, are included for each of the above categories. Defect structures and mechanisms responsible for mechanical behaviour are presented. Strengthening techniques (alloys, cold work, irradiation, quenching, composites) and recovery are briefly reviewed.

13039. Clark, A. F., **Combination of a power transmission line and an active track for a magnetically suspended high-speed train,** *J. Appl. Phys.* **43,** No. 8, 3598-3599 (Aug. 1972).

Key words: Cryogenic; high-speed ground transportation; magnetic levitation; power transmission.

The idea of utilizing proposed cryogenic power transmission lines as an active track for magnetically suspended high-speed ground transporation is briefly explored. The advantages of transporting both people and power on the same right of way are many, and proposed transmission current levels are more than adequate for suspension.

13040. Hanley, H. J. M., McCarty, R. D., **Argon third virial coefficients,** *J. Chem. Phys.* **57,** No. 7, 3023-3025 (Oct. 1, 1972).

Key words: Argon; m-6-8 potential; nonadditivity; third virial coefficients.

Experimental third virial coefficients for argon, taken from several sources, are presented. An approximate calculation for the third virial coefficient from the 11-6-8 potential, including nonadditivity effects, is also discussed and the result compared to experiment. Agreement between theory and experiment is good.

13041. Straty, G. C., Younglove, B. A., **Dielectric constant and molar polarizability of compressed gaseous and liquid fluorine,** *J. Chem. Phys.* **57,** No. 6, 2255-2259 (Sept. 15, 1972).

Key words: Clausius-Mossotti function; compressed liquid; dielectric constant; fluorine; polarizability; saturated liquid.

In this paper we present accurate wide-range measurements of the dielectric constant of saturated liquid fluorine from 70 to 140 K and of compressed fluid fluorine at temperatures between 100 and 300 K at pressures to 21 MN/m²(1 MN/m² = 9.8692 atm = 145.038 psi). The data are combined with previously measured densities to determine the molar polarizability and its dependence on density and temperature. The density range examined extends to nearly 3 times the critical density. The molar polarizability is found to increase initially with density and then decrease. Current theories of the dielectric constant are found to give satisfactory qualitative interpretation of the density dependence of the molar polarizability but do not give satisfactory quantitative predictions.

13042. Hust, J. G., **Electrical resistance ratios of Evanohm heater wire at low temperatures,** *Rev. Sci. Instrum.* **43,** No. 9, 1387-1388 (Sept. 1972).

Key words: Electrical resistance; electrical resistance temperature coefficient; heater wire; material variability.

As a consequence of using Evanohm wire as heater elements in our thermal conductivity apparatus we have obtained extensive resistance-temperature data for wires from several spools at temperatures from 5 to 300 K. These data, reduced to resistance ratios, $R(T)/R(273\ \mathrm{K})$, show the variation of resistance with temperature as well as the degree of material variability.

13043. Berger, M. J., Seltzer, S. M., **Response functions for sodium iodide scintillation detectors,** *Nucl. Instrum. Methods* **104,** 317-332 (1972).

Key words: Detection efficiency; energy deposition spectrum; gamma ray spectrum; Monte Carlo calculations; resolution; response function; sodium iodide detector.

The response of sodium iodide detectors to gamma rays has been calculated by a method that takes into account the multiple scattering and escape from the detector of the incident gamma rays as well as of the secondary charged particles and bremsstrahlung. The method is applicable to gamma rays with arbitrarily high energies, and its accuracy has been verified by comparisons with experimental response functions at energies up to 20 MeV. A systematic tabulation has been made of the response functions for 3″ × 3″ detectors irradiated with broad parallel beams of gamma rays, at energies between 100 keV and 20 MeV. These results are given in a parametrized form which makes it easy to interpolate with respect to incident gamma-ray energy. A few response functions have also been calculated for detectors irradiated with 50 MeV gamma rays. Exploratory calculations have shown that 3″ × 3″ detectors are "omnidirectional" in the sense that the shape of the response function depends very little on the direction of the incident gamma-ray beam. Therefore, the tabulated data for broad parallel beams incident perpendicularly can, in good approximation, also be applied to other source geometries, e.g., the case of a detector exposed to an isotropic gamma-ray flux.

13044. Mielenz, K. D., Eckerle, K. L., **Spectrophotometer linearity testing using the double-aperture method,** *Appl. Opt.* **11,** No. 10, 2294-2303 (Oct. 1972).

Key words: Double-aperture method; light addition; nonlinearity correction; photomultiplier nonlinearity; spectrophotometry.

The double-aperture method has been used to determine the nonlinearity correction for a new spectrophotometer having a precision of $\pm 4 / 10^{-5}$ transmittance units. The random and systematic errors of the method are discussed, and techniques are described that yield the additive nonlinearity correction to the high level of precision required for this spectrophotometer. The correction was found to be independent of source polarization, free from interference errors, but slightly dependent on wavelength.

13045. Sugar, J., **Interpretation of photoabsorption in the vicinity of the 3*d* edges in La, Er, and Tm,** *Phys. Rev. A* **6,** No. 5, 1746-1767 (Nov. 1972).

Key words: Erbium; photoabsorption; theory; thulium; 3*d* edges.

Line spectra at the 3*d* photoabsorption edges of La, Er, and Tm are interpreted as transitions of the type $3d^{10}4f^N \rightarrow 3d^9 4f^{N+1}$. Calculated relative *gf* values for these transitions are compared with published absorption curves.

13046. Buchalter, D. N., Hargreaves, J. H., Jr., **Angular displacement detector,** *Rev. Sci. Instrum. Notes* **43,** No. 11, 1711-1712 (Nov. 1972).

Key words: Angular displacement detector; light emitting diode; phototransistors.

This Note describes a detector for small angular deflections (0.1 μrad resolution). It uses a modulated infrared beam focused on a mirror whose angular deflection is to be measured. The beam is then reflected onto two phototransistors. The difference of the output voltages from these transistors is a measure of the angular displacement.

13047. Marzetta, L. A., **An evaluation of the three-voltmeter method for AC power measurement,** *IEEE Trans. Instrum. Meas.* **IM-21,** No. 4, 353-357 (Nov. 1972).

Key words: Phase-sensitive detector; power-factor; quadrature; three-voltmeter method; wattmeter.

The accuracy and frequency response limitations in the present square-law responding laboratory wattmeters have promoted the search for alternate methods of ac power measurement using electronic instrumentation. The three-voltmeter method is based on an old principle of operation implemented by new analog circuitry. Results of the tests reported here show a precision of power calculation with 0.01 percent error at frequencies below 5 kHz. A unique test procedure is described for the comparison of the three-voltmeter device and a time-division multiplier wattmeter operating at zero power factor.

13048. Goodwin, R. D., **Thermophysical properties of methane,** *Proc. 2nd Conf. on Natural Gas Research and Technology, Atlanta, Ga., June 5-7, 1972, Session V, Paper 2,* pp. 1-12 (Institute of Gas Technology, Chicago, Ill., 1972).

Key words: Methane; pressure-density-temperature relations; thermodynamic properties.

This report describes briefly the rather direct methods recently used at this laboratory to prepare tables of provisional values of thermodynamic functions for methane. The basic data are spectroscopic specific heats for ideal gas states; the vapor pressure and melting curves; available virial coefficients for low density gas; and density (PVT) measurements over the domain from the triple point (90.68 K) to 400 K at pressures to 350 bar (1 atm = 1.01325 bar). References are given for the principal sources of PVT data.

The analytical descriptions of the PVT physical properties are emphasized in this report because they are needed for smoothing, for interpolation, and for the computation of derivatives. These have been developed here in recent years to be at least qualitatively consistent with known behavior about the critical point. The nonanalytic equation of state used here is qualitatively consistent with the experimental observation that specific heats $C_v$ increase beyond measure upon close approach to the critical point.

13049. Goodwin, R. D., **Thermophysical properties of methane,** *Proc. 3rd Int. Conf. and Exhibition on Liquefied Natural Gas, Washington, D.C., Sept. 24-28, 1972, Session II, Paper 10,* pp. 1-12 (Institute of Gas Technology, Chicago, Ill., 1972).

Key words: Dielectric constants; methane, specific heats; thermal conductivities; thermodynamic functions; viscosities.

This report describes briefly the methods recently used at this laboratory to prepare tables of provisional values of thermodynamic functions for methane. References are given for the principal sources of PVT data. Emphasis is placed on analytical descriptions of physical properties because these are needed for smoothing, for interpolation, and for the computation of derivatives.

13050. Branscomb, L. M., **To help advance our Nation's scientific and technical capability for the greatest public benefit,** *Mater. Res. Stand.* **12,** No. 5, 8-12 (May 1972).

Key words: Experimental incentive program; metrication; technology; standardization.

This interview presents an overview of the National Bureau of Standards in the context of its goal "to strengthen and advance the Nation's science and technology and to facilitate their effective application for public benefit."

13051. Kushner, L. M., **We have decided to become more active at the policy level in voluntary standardization activities,** *Mater. Res. Stand.* **12,** No. 5, 13-14 (May 1972).

Key words: Engineering standards; standardization process; voluntary standardization.

The role of NBS in the voluntary standarization process used in this country is briefly outlined.

13052. Andrus, W. E., **A focus for the Bureau and all voluntary standardization organizations,** *Mater. Res. Stand.* **12,** No. 5, 15-17 (May 1972).

Key words: Engineering standards; standardization; voluntary standards system.

In interview form, the role of the NBS program office for engineering and information processing standards is outlined. The voluntary product standards program is described, as are guidelines for NBS participation in standardizing bodies.

13053. Ambler, E., **A major innovation is our measurement assurance program,** *Mater. Res. Stand.* **12,** No. 5, 18-23 (1972).

Key words: Basic standards; Josephson effect; lasers; metrology.

The mission and program of the NBS Institute for Basic Standards is presented in brief form. Calibration services, measurement assurance programs, and such new programs as laser stabilization and use of the Josephson junction in voltage monitoring are discussed.

13054. Hoffman, J. D., **IMR emphasizes accurate measurements and standards for materials,** *Mater. Res. Stand.* **12,** No. 5, 24-33 (May 1972).

Key words: Air pollution measurements; failure analysis; materials research.

Such aspects of the NBS Institute for Materials Research as air pollution measurements, failure analysis, standard reference materials, failure analysis, high pressure research, surface research, collaborative research, and others are presented. The competences of the various IMR groups are tabulated, and problems, perspectives, and future opportunities are covered.

13055. Willenbrock, F. K., **We can never afford to be technically wrong,** *Mater. Res. Stand.* **12,** No. 5, 34-36, 71-72 (May 1972).

Key words: Communications; consumer information; standardization.

A brief description of the NBS Institute for Materials Research is presented, especially as it impacts the public through information services and standardization activities.

13056. Young, T. R., **Laboratory evaluation: Facing up to a national problem,** *Mat. Res. Stand.* **12,** No. 11, 22-26 (Nov. 1972).

Key words: Accreditation; certification; evaluation; national system; reference samples; testing laboratories.

A concept of a national system for evaluation and accreditation of testing laboratory functions is reviewed. Requesting laboratories having need would be provided examinations involving on-site inspections and reference sample audits supplied by national reference laboratories or task groups of individuals. The criteria used and the examiners would be recognized by a National Board who would also issue accreditations of testing functions having a public interest, based upon evaluation of laboratory examinations. Examples of existing reference laboratories are discussed.

13057. Rowland, G. A., **A program to assist the States in accepting industrialized housing,** *Mat. Res. Stand.* **12,** No. 11, 17-21 (Nov. 1972).

Key words: Building codes; building manufacturer; Coordinated Evaluation System; engineering analysis; laboratory accreditation; Laboratory Evaluation and Accreditation Program (LEAP); Model Code Standardization Council; National Conference of States on Building Codes and Standards; quality assurance testing; testing laboratory.

The Laboratory Evaluation and Accreditation Program (LEAP) was established at the National Bureau of Standards to assist the States in the development of technical criteria and a methodology for the accreditation of institutions engaged in the evaluation of manufactured housing units for compliance with specified building codes. The needs of such a program were divided into: (1) a uniform national standard of reference; (2) a standard of laboratory competence; and (3) standards for uniform documentation of information. The program is concerned with: (1) engineering analysis; (2) physical testing; and (3) quality assurance.

13058. Powell, C. J., Mandl, A., **High-resolution measurements of the $L_3M_{2,3}M_{4,5}$ Auger transitions in nickel and copper,** *Phys. Rev. Lett.* **29,** No. 17, 1153-1156 (Oct. 23, 1972).

Key words: Aluminum; Auger transitions; copper; electronic density of states; nickel; secondary-electron energy distribution; x-ray photoemission.

Measurements are reported (with $\approx 0.1$-eV resolution) of the $L_3M_{2,3}M_{4,5}$ Auger-electron energy distributions from evaporated Ni and Cu using electron-beam excitation. The data reveal new structure (over an $\simeq$ 20-eV range) that could be correlated in part with the final states (for atomic Cu) and in part with overall features of the 3*d*-band density of states determined by soft-x-ray emission spectroscopy and x-ray photoelectron spectroscopy.

13059. Sengers, J. M. H. L., Greer, S. C., **Thermodynamic anomalies near the critical point of steam,** *Int. J. Heat Mass Transfer* **15,** 1865-1886 (1972).

Key words: Coexistence curve; compressibility; critical anomalies; critical exponents; critical region; equation of state; scaling law; specific heat; steam; water.

Ideas about the character of critical anomalies obtained from the lattice gas model are tested on the thermodynamic properties of steam, using methods developed for nonpolar gases. The critical anomalies in steam are shown to be nonclassical and very similar to those of simple gases. Specifically, the exponents obtained by power-law analysis of the coexistence curve, specific heat $C_v$ and compressibility $K_T$ are $\beta = 0.347 \pm 0.005$, $\alpha = 0.1 \pm 0.05$, $\gamma = 1.20 \pm 0.05$, implying $\delta = 4.45$. Since the critical point is thus a point of nonanalyticity in the thermodynamic behavior, the scaled equation of state may be an appropriate means to describe the critical region. Some results of such a scaled analysis of the *PVT* data are presented and shown to be consistent with independently measured vapor pressure and specific heat data and with the exponents quoted. The best value obtained for the critical temperature by scaling is 373.9 °C $\pm$ 0.05°, values between 0.322 and 0.327 g/cm$^3$ are obtained for the critical density depending on the property analyzed.

13060. Acquista, N., Abramowitz, S., **Infrared spectrum of matrix isolated $NbF_5$,** *J. Chem. Phys.* **56,** No. 11, 5221-5224 (June 1, 1972).

Key words: Infrared spectrum; Knudsen effusion; matrix isolation; molecular structure, $NbF_5$; vibrational assignment.

The infrared spectra of matrix isolated $NbF_5$ as well as some gas phase spectra have been observed. These spectra have been obtained using double boiler Knudsen cells. An interpretation of the spectra to yield the six infrared active frequencies of a $C_{4v}$ monomeric structure for $NbF_5$ is advanced.

13061. Wall, L. A., Brown, D. W., **High pressure polymerization of perfluorostyrene,** *J. Fluorine Chem.* **2,** No. 1, 73-85 (1972/73).

Key words: High pressure; perfluorostyrene; polymerization; polyperfluorostyrene.

Perfluorostyrene was prepared by reaction between pentafluorophenyllithium and tetrafluoroethylene and its physical behavior and thermal polymerization were studied in the temperature and pressure ranges 17-155° and 6,800-20,000 atm respectively. When highly superpressed the monomer becomes viscous and often glassy. The polymerization rates range from $10^{-3}$ to more than $10^2$ percent $h^{-1}$. They generally increase with temperature and pressure. Polymer intrinsic viscosities range from 0.07 to 0.41 $dlg^{-1}$. In liquid phase polymerizations they increase with pressure and decrease with temperature. In the glassy phase, polymer of lower intrinsic viscosity is formed; in the crystalline phase, higher polymer is formed.

13062. Barnes, J. A., Winkler, G. M. R., **The standards of time and frequency in the U.S.A.,** *Proc. 26th Annual Symp. on Frequency Control, Atlantic City, N.J., June 6-8, 1972,* pp. 269-284 (Electronic Industries Association, Washington, D.C., 1972).

Key words: Astronomical time; atomic time; frequency; international atomic time; management; NBS; standard time; time; USNO.

The National Bureau of Standards (NBS) and the U.S. Naval Observatory (USNO) are the two organizations chiefly involved in distributing accurate and precise time and frequency information within the U.S.A. The NBS is responsible for the "custody, maintenance, and development of the national standards" of frequency and time (interval) as well as their dissemination to the general public. The mission of the USNO includes the "provision of accurate time" as an integral part of its work concerned with the publication of ephemerides in support of navigation and in the establishment of a fundamental reference system in space.

Both agencies provide the U.S. contribution to the Bureau International de l'Heure (BIH) [International Time Bureau], which has the responsibility of publishing definitive values of Universal Time (UT), International Atomic Time (IAT), and Coordinated Universal Time (UTC).

13063. Zapf, T. L., **Accuracy and precision,** Chapter 4 in *Basic Electronic Instrument Handbook,* C. F. Coombs, Jr., ed., pp. 4-1—4-20 (McGraw-Hill Book Co., New York, N.Y., 1972).

Key words: Accuracy; error analysis; instrument errors; measurement errors; precision.

Topics in this chapter have been chosen to give the reader a basic understanding of many of the concepts, procedures, and mathematical tools used by metrologists to ascertain the accuracy and the precision of measurements. The chapter includes discussions of errors, corrections, precision, accuracy, systematic and random errors, statistical methods, measures of imprecision, computations based on samples, errors in the use of instruments, and scale-reading errors. Basic information for the treatment of errors in measurements, and in instruments, is given.

13064. Howe, D. A., **Nationwide precise time and frequency distribution utilizing an active code within network television broadcasts,** (Proc. 26th Annual Frequency Control Symp., Atlantic City, N.J., June 6-8, 1972, Electronic Industries Association, Washington, D.C., 1972), *IEEE Trans. Instr. Meas.* **IM-21,** No. 3, 263-276 (Aug. 1972).

Key words: Frequency standard; network path delay; stability; time and frequency dissemination; time code generator; time code receiver.

Because of the increasing interest in time and frequency dissemination via television signals, the National Bureau of Standards (NBS) has sponsored an experiment using an active time and frequency code transmitted on a U.S. television network encompassing nationwide coverage. Some history of the project is given. The format of the television code and the equipment necessary to generate and decode the transmitted information are discussed. Statistical results of system stability from New York City, N.Y., to Boulder, Colo., and to Los Angeles, Calif., are presented, and comparisons are made with earlier observations using the passive line-10 television time synchronization technique and the 3.58-MHz colorburst frequency reference used for colorcasts. Analysis of the frequency-transfer capability is presented, and the ability of a phase-locked oscillator to lock to the code's frequency reference is discussed. With the decoder's oscillator in a locked condition, plots of phase with respect to time, time domain stability using the Allan variance, and spectral noise reveal that the system permits calibration of a remote standard to one part in $10^{11}$ within one-half hour. Long-term stability (several days) is typically a few parts in $10^{12}$. Using an active time code, short-term stability is governed to a noticeable degree by the television industry's standard video format. Finally, a schematic diagram, with discussion, outlines how time-of-day information can be extracted from the television code used in this experiment.

13065. Faller, J. E., Bender, P. L., Alley, C. O., Currie, D. G., Dicke, R. H., Kaula, W. M., MacDonald, G. J. F., Mulholland, J. D., Plotkin, H. H., Silverberg, E. C., Wilkinson, D. T., **Geodesy results obtained with lunar retroreflectors,** S. W. Henriksen, A. Mancini, and B. H. Chovitz, eds., (Proc. Symp. on the Use of Artificial Satellites for Geodesy, Washington, D.C., April 1971), Paper 6, Extraterrestrial Geodesy in *Geophys. Mongr. Series* **15,** 261-264 (American Geophysical Union, Washington, D.C., 1972).

Key words: Earth rotation; geodesy; laser distance measurements; lunar range; polar motion.

Retroreflector packages have been carried to the moon by the Apollo 11, Apollo 14, and Apollo 15 missions, as well as by Luna 17. Laser ranging from the earth onto these packages should eventually yield information on polar motions and crustal movements accurate to a few centimeters, and on UT1 to 100 $\mu$sec. Present (1971) error of the range measurements is 30 cm, but accuracy to 3 cm should be obtainable with improvements in methods and equipment.

13066. Johnson, D. R., Lovas, F. J., **Microwave detection of the molecular transient methyleneimine ($CH_2=NH$),** *Chem. Phys. Lett.* **15,** No. 1, 65-68 (July 15, 1972).

Key words: Methyleneimine; microwave spectrum; pyrolysis; quadrupole structure; rotational transitions; transient species.

The molecular transient methyleneimine ($CH_2=NH$) has been identified in the gas phase from its microwave spectrum. Preliminary analysis of the rotational spectrum of $^{12}CH_2=^{14}NH$ shows the molecule to be planar with rotational constants (in MHz) of $A=196\,211$, $B=34\,642$, and $C=29\,352$. Estimates of the nuclear quadrupole coupling constants and electric dipole moment for the molecule are given. The half-life of this transient molecule is estimated to be less than 0.1 sec under the conditions used in the experiment under discussion.

13067. Geist, J., **Waveform-independent lock-in detection,** *Rev. Sci. Instrum.* **43,** No. 11, 1704-1705 (Nov. 1972).

13068. Mizushima, M., Wells, J. S., Evenson, K. M., Welch, W. M., **Laser magnetic resonance of the $O_2$ molecule using the 337-$\mu$m HCN laser,** *Phys. Rev. Lett.* **29,** No. 13, 831-833 (Sept. 25, 1972).

Key words: HCN laser; laser magnetic resonance; molecular constants of $O_2$; $O_2$ spectrum.

We observed thirteen laser magnetic resonance lines (transitions between $[n=3,\ J=4]\rightarrow[n=5,\ J=5]$ for the oxygen molecule, using the 337-$\mu$m line of the HCN laser. The magnetic $g$ factors ($g_\perp=2.0044$, $g_z=2.0020$, and $g_n=0.000\,125$) give the best fit to the data. The zero-field frequency for the transition $(N=J=3)\rightarrow(N=J=5)$ obtained by using these sets of the magnetic $g$ factors all agree with theoretical value of $775.700\,43\pm0.000\,01$ GHz if an experimental uncertainty of $\pm 1$ G ($\pm 10^{-4}$ T) is allowed.

13069. Wells, J. S., Evenson, K. M., Day, G. W., Halford, D., **Role of infrared frequency synthesis in metrology,** *Proc. IEEE Letters* **60,** No. 5, 621-623 (May 1972).

Key words: Frequency metrology; frequency of lasers; infrared frequency synthesis; laser frequency stabilization; methane-stabilized He-Ne laser; speed of light.

Infrared frequency synthesis (IFS) techniques are briefly surveyed, and some important results are summarized. The recent measurement of the frequency of the methane-stabilized He-Ne laser is significant due to the accurate measurement of the methane wavelength and its fundamental role in metrology. The possibilities of an improved value for the speed of light and of additional applications for frequency measurements at various levels of accuracy are discussed.

13070. Howe, D. A., **Results of active line-1 TV timing,** *Proc. IEEE Letters* **60,** No. 5, 634-637 (May 1972).

13071. Phillips, W. E., **Interpretation of steady-state surface photovoltage measurements in epitaxial semiconductor layers,** *Solid-State Electron.* **15,** No. 10-E, 1097-1102 (Oct. 1972).

13072. Arp, V., **Forced flow, single-phase helium cooling systems,** Chapter on Helium Heat Transfer in *Advances in Cryogenic Engineering.* A Collection of Invited Papers presented at National Technical Meetings during 1970 and 1971, **17,** Paper J-4, 342-351 (Plenum Press, Inc., New York, N.Y., 1972).

Key words: Forced flow; heat transfer; helium; refrigeration.

A flow loop using pumped supercritical helium for transferring heat from a source to a sink is considered. General factors concerning design of the loop are outlined, and pumping losses are considered in some detail. It is concluded that pumping losses depend very sensitively on the heat transfer requirements, and optimization of design must be done carefully for any particular system. Further studies of combined heat transfer and refrigeration cycles are encouraged.

13073. Brennan, J. A., Mann, D. B., Dean, J. W., Kneebone, C. H., **Performance of NBS cryogenic flow research facility,** Chapter on Measurement and Instrumentation in *Advances in Cryogenic Engineering.* A Collection of Invited Papers presented at National Technical Meetings during 1970 and 1971, **17,** Paper G-2, 199-205 (Plenum Press, Inc., New York, N.Y., 1972).

Key words: Accuracy statement; cryogenic; flow facility; liquid nitrogen; measurement.

The National Bureau of Standards and the Compressed Gas Association has jointly sponsored a research program on cryogenic flow measurement. A cryogenic flow research facility was constructed and was first used to evaluate commercially available positive displacement cryogenic flowmeters operating with liquid nitrogen.

The performance of the flow facility was simultaneously being evaluated during the meter tests. This is a summary report of the performance evaluation of the flow facility. An accuracy statement is given for both totalized mass and volumetric flow.

13074. Broadhurst, M. G., **Use and replaceability of polychlorinated biphenyls,** *Environ. Health Perspect.*, pp. 81-102 (Oct. 1972).

Key words: Dielectric fluids; heat transfer; plasticizers;

polychlorinated biphenyl; transformers.

On September 1, 1971, an interdepartmental task force was formed to coordinate the U.S. Government's scientific studies of polychlorinated biphenyl (PCB's). The task force was coordinated by the Office of Science and Technology and the Council on Environmental Quality. Represented on the task force were the following agencies: the Environmental Protection Agency, the Food and Drug Administration, the National Institute of Environmental Health Services, and the Departments of Agriculture, Commerce, Interior, and Justice.

On September 13, individual tasks were assigned to participating agencies, and the Department of Commerce was asked to critically explore the question of the utility and replaceability of PCB's. Dr. Robert W. Cairns, Deputy Assistant Secretary of Commerce for Science and Technology, requested NBS to assist him in this task.

This study has included consideration of the uses and replaceability in PCB's in the following areas: (1) Dielectric fluids for capacitors and transformers; (2) Industrial fluids for hydraulic, gas turbine, and vacuum pump uses; (3) Heat transfer fluids; and (4) Plasticizers and miscellaneous uses.

13075. Suzuki, G., **Measurements and nuclear accountability methods,** *Proc. AEC Symp. on Safeguards Research and Development, Los Alamos, Mex., Oct. 27-29, 1969,* pp. 67-68 (Mar. 1970).

Key words: Nuclear material balance accountability; nuclear material control; nuclear safeguards.

The problem discussed is the need for better material accountability through the application of better measurements in nuclear safeguards. This paper points out that accountability has many aspects and compares two of them. One aspect is that accountability is considered in the sense of a tighter material balance, accomplished by more accurate measurements in material accounts of inputs, outputs, and in inventory. Although the material balance for a process or, if you will, the entire plant is a necessary tool in nuclear materials accountability, its usefulness is limited to an indication that there is an unaccounted for loss but such loss is not necessarily due to diversion of material or to an unusual situation. Since the material balance is an aggregative tool dealing with totals, it generally does not provide a clue as to whether the material unaccounted for is in one lump or in small pieces or some intermediate form. Another aspect is that accountability be considered in the same sense except that it be accomplished by maintaining material balances around subprocesses, thus serving the additional function of material control. It points out that material control data are important especially in areas where process losses are suspected. In this manner, the safeguards capability of a plant would be enhanced both from the safeguards and plant material control points of view.

13076. Huie, R. E., Herron, J. T., Davis, D. D., **Rates of reaction of atomic oxygen with $C_2H_3F$, $C_2H_3Cl$, $C_2H_3Br$, 1,1-$C_2H_2F_2$, and 1,2-$C_2H_2F_2$,** *Int. J. Chem. Kinet.* **IV,** 521-527 (1972).

Key words: Atomic oxygen; haloethylenes; kinetics.

Rate constants for the reactions of atomic oxygen ($O^3P$) with $C_2H_3F$, $C_2H_3Cl$, $C_2H_3Br$, 1,1-$C_2H_2F_2$, and 1,2-$C_2H_2F_2$ have been measured at 307 K using a discharge-flow system coupled to a mass spectrometer. The rate constants for these reactions are (in units of $10^{11}$ $cm^3$ $mole^{-1}s^{-1}$) $2.63 \pm 0.38$, $5.22 \pm 0.24$, $4.90 \pm 0.34$, $2.19 \pm 0.18$, and $2.70 \pm 0.34$, respectively. For some of these reactions, the product carbonyl halides were identified.

13077. Huie, R. E., Herron, J. T., Davis, D. D., **Absolute rate constants for the reaction $O+O_2+M \rightarrow O_3+M$ over the temperature range 200-346 K,** *J. Phys. Chem.* **76,** No. 19, 2653-2658 (1972).

Key words: Atomic oxygen; kinetics; oxygen.

Using the technique of flash photolysis-resonance fluorescence, absolute rate constants have been measured for the reaction $O + O_2 + M \rightarrow O_3 + M$. For the case of M=Ar the temperature range covered was 200-346 K, and the total pressure was varied from 50 to 500 torr. Over the indicated temperature range, an Arrhenius plot of the data yielded the expression $k_{Ar} = (6.57 \pm 0.59) \times 10^{-35} \exp[(1014 \pm 46 \text{ cal mol}^{-1})/RT]$ $cm^6$ $molecule^{-2}$ $sec^{-1}$. A comparison of the third-order rate constants for M= He, Ar, and $N_2$ gave the relative efficiencies for these three gases as 0.92:1.0:1.6 at 298 K. At 218 K, the efficiencies of Ar to $N_2$ were in the ratio of 1.0:1.7. The reported rate measurements indicate that the rate of production of stratospheric ozone could be nearly a factor of 2 lower than that estimated from previously reported values of the third-order rate constant.

13078. Koidan, W., Hruska, G. R., Pickett, M. A., **Wedge design for National Bureau of Standards anechoic chamber,** *J. Acoust. Soc. Amer.* **52,** No. 4, Part 1, 1071-1076 (1972).

Key words: Anechoic chamber design; plane-wave tubes; wedges.

Design techniques for anechoic room wedges must always be used with caution because of the possibility that a manufacturer may change the properties of the material. This paper describes efforts at the National Bureau of Standards to adapt to relatively new glass wool manufactured in the United States. A "hybrid" wedge designed for a large anechoic chamber at NBS consists of glass wool of two densities: 3 lb/ft³ for the 55-in-long tapered portion and 1.1 lb/ft³ for the 11-in-long base. Experimental evidence indicates that the lightweight material and the 4-in air space behind the wedge, in conjunction with the heavier material, serve to produce a useful resonance absorption. The "cutoff frequency" attained for the 70-in-long structure was about 45 Hz as measured in a 31-ft plane-wave tube. Normal acoustic impedance measurements looking into the wedge from the tip were made for the hybrid wedge and a half-scale model.

13079. Kaldor, A., Olson, W. B., Maki, A. G., **Pollution monitor for nitric oxide: A laser device based on the Zeeman modulation of absorption,** *Science* **176,** 508-509 (May 5, 1972).

Key words: Air pollution; infrared spectroscopy; lasers; nitric oxide; Zeeman effect.

The concentration of nitric oxide can be monitored by a new device in which the Zeeman effect is used to shift an absorption line of nitric oxide into coincidence with a laser line of carbon monoxide. The absorption is modulated by a small, oscillating magnetic field. This device is specific for nitric oxide and is not subject to interference from other gases.



U. S. GOVERNMENT PRINTING OFFICE : 1973 OL - 496-895

UNITED STATES
GOVERNMENT PRINTING OFFICE
PUBLIC DOCUMENTS DEPARTMENT
WASHINGTON, D.C. 20402

OFFICIAL BUSINESS
PENALTY FOR PRIVATE USE, $300

U.S. DEPARTMENT OF COMMERCE
POSTAGE AND FEES PAID
375

JOURNAL OF RESEARCH of the National Bureau of Standards
A. Physics and Chemistry

Vol. 77A, No. 3 May–June 1973

SJRA UNIVE300UB 46129D 1
UNIVERSITY MICROFILMS INC
ATTN SERIALS SECTION
300 NORTH ZEEB RD
ANN ARBOR MI 48106

ts

Page

**The International Practical Temperature Scale of 1968 in the region 13.81 K to 90.188 K as maintained at the National Bureau of Standards. George T. Furukawa, John L. Riddle, and William R. Bigge.** 309

**Radiance temperature of niobium at its melting point. Ared Cezairliyan.** 333

**An experimental search for gaseous reactivity between $AlF_3$ and HF near 1200 K. Thomas B. Douglas and Ralph F. Krause, Jr.** 341

**A numerical solution of the integral equation describing a photometric integrating sphere. Robert L. Brown.** 343

**Crystallization of random copolymers. Isaac C. Sanchez and Ronald K. Eby.** 353

**Theory of disclinations. III. Continuous and discrete disclinations in isotropic elasticity. Roland deWit.** 359

**Compressive fatigue coaxing in composites. C. A. Berg and M. Salama.** 369

**Publications of the National Bureau of Standards.** 375

Library of Congress Catalog Card Number: 62–37059

For sale by the Superintendent of Documents, U.S. Government Printing Office, Washington, D.C. 20402. (Order by SD Catalog No. C 13.22/sec.A:77/3). Single copy price varies. Subscription price $17.00 a year; $4.25 additional for foreign mailing.

UNITED STATES GOVERNMENT PRINTING OFFICE, WASHINGTON : 1973